# In Situ Study of Atmospheric Stress Corrosion Crack Initiation in Aluminum 6061-T6 and Particulate SiC Reinforced Nanocomposite

Like Mo

*Corpus Christi College*

A Thesis Submitted for the Degree of

MSc by Research

Department of Materials, University of Oxford

2019



## Table of Contents

*Acknowledgments* ..... *v*

*Abstract* ..... *vi*

*1 Introduction and motivation* ..... *1*

*2 Literature review* ..... *3*

**2.1 Introduction** ..... **3**

**2.2 Stress corrosion cracking** ..... **4**

2.2.1 Mechanism of stress corrosion cracking ..... 4

2.2.2 Stress corrosion cracking of aluminum alloys ..... 5

2.2.3 Stress corrosion cracking and pitting ..... 12

**2.3 Long cracks and small cracks** ..... **15**

**2.4 6061-T6 aluminum alloy and 6061-T6 aluminum based composites with SiC nanoparticles** ..... **16**

2.4.1 6061-T6 aluminum alloy ..... 16

2.4.2 6061-T6 aluminum based composites with SiC nanoparticles ..... 17

**2.5 Methodology for SCC experiment** ..... **19**

2.5.1 Specimen ..... 19

2.5.2 Corrosive environment and stress ..... 23

2.5.3 Observation and analysis method ..... 26

**2.6 Conclusion** ..... **31**

*3 Experimental Methods* ..... *33*

**3.1 Materials** ..... **33**

**3.2 Characterization ..... 34**

3.2.1 Hardness ..... 34

3.2.2 Yield stress ..... 34

3.2.3 X-ray Diffraction (XRD) ..... 37

**3.3 Preparation for stress corrosion cracking test ..... 38**

3.3.1 DIC error test ..... 38

3.3.2 Calibration of the proving ring ..... 39

3.3.3 Specimen preparation ..... 40

3.3.4 Strain check ..... 42

3.3.5 Pre-pitting ..... 42

**3.4 Stress corrosion cracking test ..... 43**

3.4.1 Loading of the test specimens ..... 43

3.4.2 Proving ring holder for optical observations ..... 44

3.4.3 Strain distribution check ..... 45

3.4.4 Salt deposit application ..... 46

3.4.5 Temperature and humidity ..... 46

3.4.6 Optical images recording ..... 48

**3.5 Data analysis ..... 48**

3.5.1 Digital image correlation ..... 48

3.5.2 Translation and rotation removal ..... 49

3.5.3 Displacement map stitching ..... 50

3.5.4 Strain calculation ..... 53

3.5.5 Scanning Electron Microscope (SEM) and X-ray Tomography ..... 54

*4 6061 T6 aluminum alloy* ..... *56*

**4.1 Characterization of 6061 T6 aluminum alloy** ..... **56**

4.1.1 Hardness ..... 56

4.1.2 Tensile test ..... 56

4.1.3 X-ray Diffraction (XRD) ..... 60

**4.2 Preparation for stress corrosion cracking test** ..... **62**

4.2.1 DIC error test ..... 62

4.2.2 Pre-pitting test ..... 68

4.2.3 Calibration of the proving ring ..... 72

**4.3 Stress corrosion cracking behavior** ..... **77**

4.3.1 SEM ..... 79

4.3.2 DIC ..... 84

4.3.3 X-ray Tomography ..... 100

**4.4 Summary** ..... **113**

*5 6061 T6 aluminum based composite* ..... *116*

**5.1 Characterization of 6061 T6 aluminum based composite** ..... **116**

5.1.1 Hardness and yield stress ..... 116

5.1.2 Tensile test ..... 116

5.1.3 X-ray Diffraction (XRD) ..... 118

**5.2 Stress corrosion cracking behavior** ..... **120**

5.2.1 SEM ..... 120

5.2.2 DIC ..... 124

5.2.3 X-ray Tomography ..... 127

**5.3 Summary** ..... **134**

***6 Discussion*** ..... ***135***

**6.1 6061 T6 aluminum alloy** ..... **135**

6.1.1 Characterization ..... 135

6.1.2 DIC precision ..... 136

6.1.3 Pitting ..... 137

6.1.4 Stress corrosion cracking ..... 138

**6.2 6061 T6 aluminum based composite** ..... **142**

6.2.1 Characterization ..... 142

6.2.2 Stress corrosion cracking ..... 142

***7 Conclusion and future work*** ..... ***146***

***Reference*** ..... ***149***

# Acknowledgments

I would like to thank my supervisors Prof. James Marrow and Prof. Marina Galano. They helped me to decide the research direction, to design the experiment plan, and to address the problems in the experiment. At the same time, they encouraged me to think and work innovatively. I also want to thank technicians Peter Flaxman, Tony Wheeler and Robin Vincent for machining specimens for me, and Dr. Philip Holdway for helping me to conduct the XRD test. I am grateful to technician Ashley Brown for helping me to fix the environmental chamber, and to Jennifer Holter for training me on SEM.

I want to thank my group members. Philip Earp trained me on DIC, and also gave me many useful suggestions on experiments. Matthew Jordan developed a Matlab code to remove the rotation of displacement map, and I used that code to process my data. Fang Wan and Yixuan Zhao trained me on X-ray tomography, and Talha Pirzada gave me suggestions on SEM. Weiyue Xu gave me suggestions on the thesis writing.

Finally, I would like to thank my parents for supporting me to pursue the MPhil degree. They not only gave me finance support, but also encouraged me when I encountered difficulties.

# Abstract

This project aimed to study the atmospheric stress corrosion cracking (SCC) behavior of 6061 T6 aluminum alloy and a composite based on the same alloy, reinforced with SiC nano particles.

The materials were machined into taper-shape specimens, and on each specimen, three salt deposits were applied at the center and two ends. The SCC experiment was conducted at a temperature of 40 ºC and a relative humidity of 30%. The 6061 T6 aluminum alloy specimens and the composite specimens were tested at an applied constant load of 948±20 N and 1050±20 N respectively.

Cracks were only observed at the center salt deposit location of 6061 T6 aluminum alloy specimens. It is observed that pre-pitting accelerates the development of strain, but does not affect the final strain that is developed in the SCC test. There was no measurable strain change at the end location of all the 6061 T6 aluminum specimens, indicating that there is a threshold of applied stress or strain for stress corrosion cracks to develop.

For the aluminum based composite, no crack was found on the specimens. The applied strain of the center location of the composite specimen is equal to that of the end location of the aluminum specimen, within the error range, and it is concluded that the addition of SiC nano particles may make the composite material more susceptible to stress corrosion.

DIC technique was adopted to measure the displacement and strain change of specimens, and an effective method to monitor the initiation and propagation of small cracks has been developed. SEM and X-ray tomography were used to observe specimens after SCC testing, verifying the DIC result.

# 1 Introduction and motivation

6061 T6 aluminum alloy is widely used in architecture and the automotive industry because of its excellent mechanical and thermal properties. It is reported to have a good resistance to stress corrosion cracking (SCC), and this thesis is intended to investigate the SCC behavior of 6061 T6 aluminum alloy when strained and in a corrosive environment with high chloride ion concentration.

The long crack propagation mechanism has been fully investigated which is mainly controlled by the stress intensity factor. However, short crack propagation cannot be explained by that theory, since the crack tip is so close to the surface that stress and strain field are disturbed. Therefore, in this work, smooth specimens were adopted to conduct the SCC test, and the initiation and propagation of small cracks were studied.

In order to precisely measure the effects of the small cracks, digital image correlation (DIC) technique was used to monitor the displacement and strain change of specimens during the SCC test. The principle of DIC is analysis of optical images by tracking the features on the sample surface and correlating corresponding subsets to calculate a relative displacement map. SEM and X-ray tomography were used to observe pitting and cracking.

In the SCC test, a constant load was applied through the proving ring, and therefore, the specimens can be put under the optical microscope without load change. On each specimen, three salt deposits were applied by the evaporation of $MgCl_2$ solution. In the test conditions, the salt deposit creates a surface layer of aqueous $MgCl_2$ solution.

A 6061 T6 aluminum composite reinforced with SiC nanoparticles has a higher strength than the unreinforced 6061 T6 aluminum alloy. This project used the same

methodology to study the SCC behavior of the composite, and by comparing the result of two materials, the effect of the addition of SiC nanoparticles on corrosion was researched.

# 2 Literature review

## 2.1 Introduction

6061-T6 aluminum alloy has excellent mechanical and thermal properties, and the addition of SiC particles could increase the strength of alloy. However, SiC nanoparticles reinforced 6061 aluminum composite may face the problem of stress corrosion cracking (SCC). The propagation rate of SCC is slow, and it occurs with no obvious plastic deformation. When the size of crack reaches a threshold value, it could result in unexpected sudden failure[1]. Therefore, the SCC behavior of a 6061 aluminum based composite with SiC nanoparticles is worth studying. However, the SCC process of SiC nanoparticles reinforced 6061 aluminum composite is not well studied, especially the propagation of short stress corrosion crack. This remains to be investigated with the help of new techniques.

This literature review firstly introduces the general mechanisms of stress corrosion cracking, and then focuses on the SCC mechanism of aluminum alloys, the transfer from pitting to stress corrosion crack, and the different growth rates of long and small cracks. Secondly, a general introduction about 6061-T6 aluminum alloy and SiC nanoparticles reinforced 6061 aluminum composite is given, and the reported effects of reinforced particles on corrosion resistance are reviewed. Finally, this literature review considers the common methods of SCC testing, including specimen type, the method of creating corrosive environment, applying stress, observation and analysis.

## 2.2 Stress corrosion cracking

Stress corrosion cracking (SCC) refers to the cracking process caused by the combined simultaneous interaction of corrosive environment and stress. It usually happens in alloys such as aluminum alloy and stainless steel, rather than pure metals, and also happens in polymers and ceramics. There are three essential requirements for SCC, that is, materials susceptible to SCC, tensile stress higher than a threshold value and suitable corrosive environment[2].

### 2.2.1 Mechanism of stress corrosion cracking

For stress corrosion cracking of metals, three mechanisms are widely accepted[3]. The first one is active path dissolution, which promotes intergranular failure. This proposes that a grain boundary has higher susceptibility than the bulk of material, as the segregation of impurity elements there will make it harder to be passive. Therefore, the grain boundary serves as an active path to accelerate the corrosion, and the role of stress is to open up the crack. The second mechanism is about hydrogen embrittlement, which can promote intergranular or transgranular failure[4]. Hydrogen atoms diffuse to the crack or notch tip due to hydrostatic tensile stress, assisting in the fracture. The last one is film-induced cleavage, which promotes transgranular failure. For a ductile material with brittle film (for example, brass ductile substrate with brittle TiN film[5]), the brittle film could allow the crack to propagate rapidly into the material for about 1μm before ductile blunting by strain rate sensitive dislocation activity, and this process is repeatable. Some researchers also used passive film mechanism to explain SCC in aluminum[6,7,8].

### 2.2.2 Stress corrosion cracking of aluminum alloys

#### 2.2.2.1 SCC mechanisms of different series of aluminum alloys

In general, aluminum alloys have high corrosion resistance. It is mainly attributed to the oxide skin formed on the surface, which protects the metal from further oxidation[9]. However, different series of aluminum alloys has different stress corrosion resistance, as they have different alloying elements. These elements will play an important role in the formation process and stability of the protecting film. In addition, they would cause the difference in grain size, orientation and residual stresses[2].

Aluminum alloys can be divided into casting alloys and wrought alloys. Most of the aluminum alloys are the wrought, and are described in different series using a 4-digit identification system[10]. The designation number is usually followed by a temper designation that represents different processing method. For example, letter 'T' indicates heat treatment[11].

1xxx series

1xxx series refers to pure aluminum containing more than 99% of aluminum. In ASM, it is reported to be the most corrosion resistant amongst all aluminum alloy series. In an aqueous environment of pH 4 to 9, only water staining and pitting occur[12]. However, G. M. Bond et al. used an in-situ environmental-cell TEM deformation technique to compare the fracture behavior of hydrogen charged and uncharged pure aluminum specimens. They found out that the hydrogen environments could increase dislocation mobility, and therefore, the stress for fracture propagation would decrease and the failure would be more microscopically ductile. Although they indicated that the presence of hydrogen could promote

facture, they did not directly prove that SCC could occur on 1xxx series aluminum alloy and be caused by hydrogen embrittlement. But their research still casts doubt on the stress corrosion resistance of this series aluminum alloy[13].

2xxx series

The main alloying element of 2xxx series is copper, and some 2xxx aluminum alloys also have the addition of magnesium and lithium. H. Vogt and M. O. Speidel investigated the 2014 aluminum alloy, loading it to different K (stress intensity) values and immersing it in high purity water. Then they used an anodic dissolution mechanism to correctly predict the effect of stress intensity (K) on growth rate [14]. However, W. Gruhl stated that the mechanism in Al-Cu-Mg alloys was not stress corrosion but intergranular corrosion that could happen without the existence of stress[15].

3xxx series and 4xxx series

The principle alloying element of 3xxx series aluminum alloy is manganese (no more than 1.5%), while the major addition of 4xxx series aluminum alloy is silicon but that can be added up to 12%[12]. They are reported to be immune to the corrosion although Ali Davoodi studied a newly developed Al-Mn-Si-Zr fin alloy and found a few 'tunnel like' pits after 2 days of exposure in artificial ocean water acidified with acetic acid to pH 4[16].

5xxx series

The major alloying element of 5xxx series is magnesium, and sometimes with the second addition of manganese. Unlike other series aluminum alloys mentioned above, more than one SCC mechanism has used to explain the stress corrosion behavior of 5xxx series aluminum alloy.

For example, J. R. Pickens et al. put 5083 aluminum alloy tension specimens in NaCl solution and studied the time-to-failure change, with and without the addition of a hydrogen recombination inhibitor. The principle of hydrogen recombination inhibitor (As) is that it could retard the chemical reaction[6]:

$H + H \rightarrow H_2$

Therefore, the inhibitor could increase the concentration of hydrogen atoms. They found that the time-to-failure was doubled without the help of inhibitor, and therefore, they obtained the conclusion that in tension mode, hydrogen embrittlement was the main reason for SCC in 5083 aluminum alloy[17].

T. Skoulikidis and J. Colios studied notched 5052 specimens, and they found the time-to-failure of specimen that was electrolytically machined was half of that was mechanically machined, which indicated an active path was introduced when machining the notch and this played an dominant role in SCC process[18]. T. Skoulikidis then used passive film theory to explain the SCC process in a 5052 aluminum alloy that had undergone H38 treatment. They put stressed specimen vertically and horizontally respectively, finding that the time-to-failure of sample depended on the orientation of the $\gamma_1$- $Al_2O_3$ cells in the anodized film relative to the stress axis[7,6].

The common doubt in these papers is that they investigated the roles of hydrogen embrittlement, active path and passive film mechanisms played in 5xxx series aluminum alloy SCC process by comparing the time-to-failure instead of the growth rate which is more directly related to SCC behavior. It may be because of the limitation of technique at that time. Connolly et al. did the SCC test on aluminum alloy AA2024, proving that the X-ray tomography can be used to measure the growth rate[19].

6xxx series

The principle alloying elements of 6xxx series aluminum alloy are magnesium and silicon. It is widely believed that SCC normally happens in 2xxx,5xxx and 7xxx series aluminum alloy, while rarely occurs in 6xxx[20]. In addition, among 6xxx series aluminum alloys, 6061-T6 is believed to be most resistant to stress corrosion cracking[9,21]. T6 means the solution heat treatment followed by artificial aging, and this peak-aged state will further decrease the sensitivity of SCC. There is no literature clearly explaining why T6 peak aging would increase the SCC resistance of 6061 aluminum alloy, however.

Although there are a few service records of stress corrosion cracking failure for 6xxx aluminum alloys, stress corrosion cracks could be demonstrated in 6xxx alloys in lab tests under extreme conditions[22]. R. Braun[23] observed SCC phenomenon in 6061-T4 aluminum alloy using aqueous solution of 3% NaCl + 0.3% $H_2O_2$ in slow strain rate tests. Also, T. E. Graedeli et al.[24] and S. I. Pyun et al.[25] found that the combined simultaneous interaction of $Cl^-$ and $SO_4^{2-}$ resulted in more severe SCC on 6xxx aluminum alloy than that caused by their single action.

7xxx series

The major alloying element of 7xxx series aluminum alloy is zinc, whereas there are various addition elements such as copper, magnesium, chromium and zirconium. Similar to 5xxx series aluminum alloy, various mechanisms are proposed to explain its SCC behavior.

The first one is hydrogen-induced SCC. L. Oger et al. used SEM to observe the effect of hydrogen on the fracture mode of 7046-T4 aluminum alloy. They compared the pre-corroded sample and healthy sample, and found that in healthy sample, the

initial fracture mode was ductile-intergranular, while in pre-corroded sample that was the combination of brittle intergranular and cleavage[26].

The second one is anodic dissolution or active path dissolution. A. Joshi et al. compared the solute segregation under T6 and T73 heat treatments of 7075 aluminum alloys with Auger electron spectroscopy. Large amounts of alloying elements were observed to concentrate around grain boundaries under T6 than under T73 heat treatment, and the authors believed that this was the reason of higher SCC susceptibility of 7075-T6[27].

Other mechanisms used to explain SCC behavior of 7xxx series aluminum alloys include passive film rupture[8] and surface mobility[28]. In 7xxx series aluminum alloys, the T6 tempered condition increases the susceptibility to SCC. T73 temper could give 7xxx series aluminum alloys more stress corrosion cracking immunity than T6 at the cost of losing some degrees of strength[29].

#### 2.2.2.2 Factors that affect the aluminum alloys SCC behavior

Various factors influence the SCC process in aluminum alloys[30]. In terms of metallurgy, Sun Zhihua et al.[31] found that the threshold stress intensity factor for stress corrosion cracking ($K_{ISCC}$) of 7B04-T6 aluminum alloy is 120 MPa$\sqrt{m}$, while that of 7B04-T74 is 300 MPa$\sqrt{m}$, which means that the susceptibility of SCC decreased with over aging.

The environmental factors could be divided into humidity, temperature and corrosive substance. Joseph R. Davis[9] studied the relation between relative humidity and stress corrosion crack velocity of 7075-T651 aluminum alloy, showing that the velocity increased along with the increase of humidity, and the increase of temperature could also result in a higher corrosion rate. However, Jacob Siegel et al. obtained a

contradictory result from SCC tests on AA 5xxx alloys under cyclic relative humidity, observing an increased crack velocity with decreasing relative humidity[32]. Therefore, the relation between cyclic relative humidity and stress corrosion rate may be different from that between constant relative humidity and stress corrosion rate. The applied stress will also affect SCC[33]. Osama M. Alyousif et al. conducted experiments with 5052-H3 aluminum alloy, finding that with decreasing of applied stress, the time-to-failure increases (Figure 1):

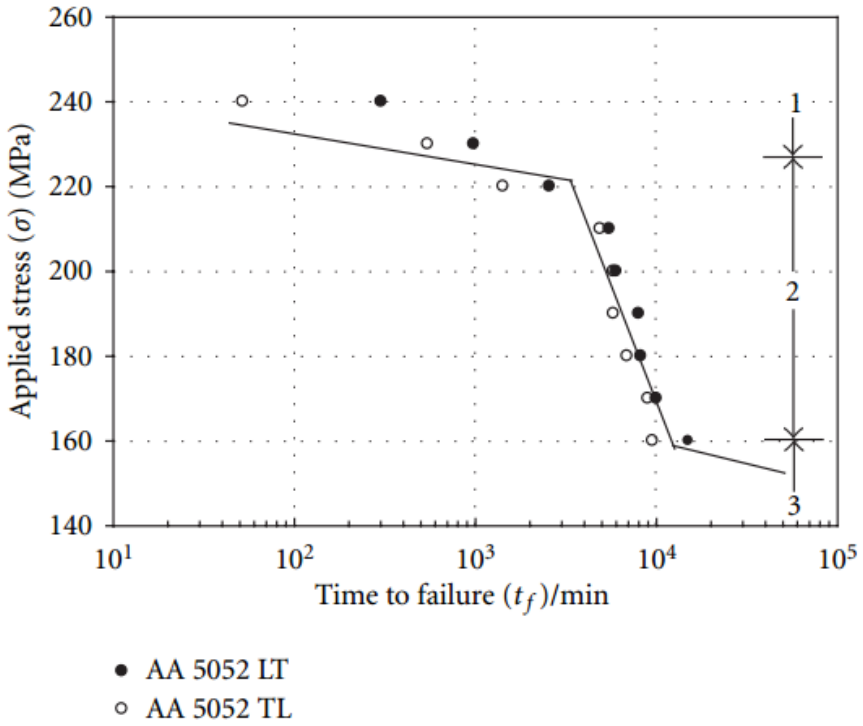



*Figure 1 The relation between the logarithm of time-to-failure and applied stress for the aluminum alloy A5052-H3 specimen with a yield stress of 180 MPa when exposed to 0.5 M sodium chloride solution. LT refers to the sample orientation along the rolling direction, while TL refers to the orientation transverse to the rolling direction*[33]

The deformation of materials also plays an important role in corrosion behavior. When aluminum alloys undergo hot and cold rolling, the shear deformation will result in the generation of a thin deformation layer at the surface. This layer will be affected by fine intermetallic particles formed in the later annealing process[34]. Ambat et al. compared the anodic and catholic reactivity of the thin deformed layer and the bulk in Al-1Mn-0.4Fe-0.3Si model alloy and AA3005 rolled sheet, finding out that the layer has a higher reaction rate than the bulk[35]. Not only rolling but also surface preparation procedures like grinding, machining and blasting could cause a deformed layer. Scamans et al. investigated the corrosion resistance of hot rolled AA3005 aluminum alloy after grinding and subsequent annealing. They claimed that the grinding was able to help generate ultra-fine activating surface layers enhanced by fine intermetallic particles, and these layers are susceptible to filiform corrosion[36]. S.H. Kim et al. found that when exposing recrystallized high purity (99.9999%) aluminum to hydrochloric acid, bands with different corrosion resistance would be formed parallel to the rolling direction. The corrosion resistance is mainly attributed to the grain orientation and boundary angle. Predominantly cube texture oriented grains and low-angle boundaries could help to considerably increase the corrosion resistance of band[37].

#### 2.2.2.3 Methods to protect aluminum alloys from SCC

There are several methods used to protect aluminum alloys from SCC. The first one is restricting the strength level of the aluminum alloy, and increasing strength generally leads to a decrease of fracture toughness, which decreases the critical crack size. Nevertheless, sometimes, for some specific alloys, the resistance to stress corrosion cracking could be increased without the cost of losing strength. For

example, for the 7xxx series aluminum alloys, T6 temper will give them a near-peak strength, while over-aging to T73 temper could decrease their SCC susceptibility but the strength will also decrease. A heat treatment called retrogression and re-aging (RRA), however, could combine the SCC resistance of T73 temper and the strength level of T6 temper. Retrogression refers to the treatment of reheating the material in a specific temperature range (higher than the temperature of T6 and T73, normally range from 200 °C to 280 °C) for several minutes, while re-aging is using the same conditions as in T6 aging after retrogression. Because of high temperature, RRA could increase the sizes of precipitates in the matrix and at the grain-boundary. With larger precipitate size, the slip mode is more homogeneous, and the slip planarity is reduced. This effectively helps to increase the SCC resistance [29]. Other methods include applying corrosion resistance coatings and stress relief treatment[20].

### 2.2.3 Stress corrosion cracking and pitting

Pitting corrosion is a kind of localized corrosion and also an electrochemical oxidation-reduction (redox) process. It mostly happens in metals with a passive oxide layer (for example, aluminum alloys, stainless steels), and the existence of chloride, sulphate or bromide ions could accelerate the pitting process. There are three possible ways for the chloride ion to participate in the pitting initiation: penetration, film breaking and adsorption at the oxide surface[38].

The corrosion rate of pitting is about 10 to 100 times of that of uniform corrosion, which makes it much more dangerous than normal corrosion[39].

Many stress corrosion cracks initiate at pits. However, not all the pits will transfer to stress corrosion, depending on the electrochemistry, geometry, materials' chemistry

and stress or strain rate. Stress concentration factor is usually used to quantify the stress concentration level of material, and it is calculated as Equation 1:

*Equation 1* $SCF = \frac{\sigma_{max}}{\sigma_{ref}}$

where $\sigma_{ref}$ is the reference stress of the material without stress concentration when applied the same load.

Many researchers simulated the relation between the aspect ratio (a/2c, a refers to the depth while 2c refers to the diameter of pits) and the stress concentration factor (SCF)[40,41] as shown in Figure 2. It can be observed that the SCF increases with the increase of the aspect ratio, and as discussed before, a larger stress leads to a higher possibility of crack initiation. Fang B. et al. cyclically loaded the pre-pitted X-52 pipeline steel specimens in near-neutral pH environment, and observed that the aspect ratio of the non-cracking pits were almost all below 0.6, while many cracking pits were found to have an aspect ratio larger than 0.5 (Figure 3)[42].

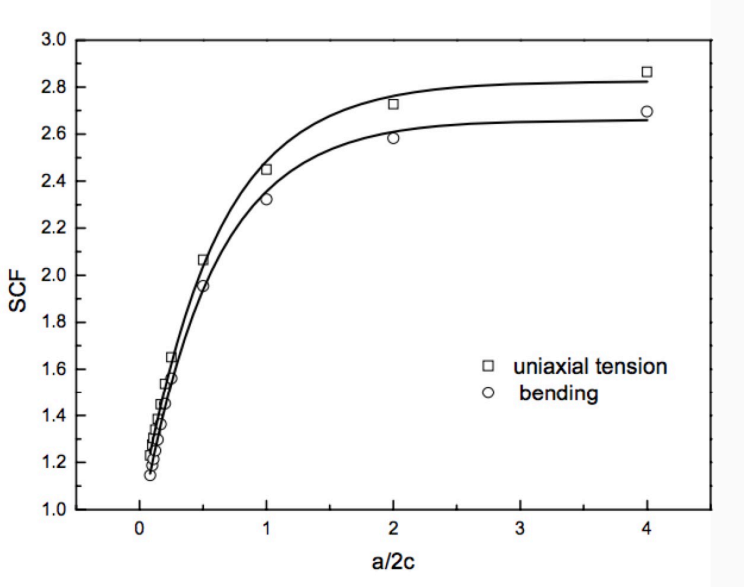



*Figure 2 The relation between stress concentration factor (SCF) and aspect ratio (a/2c) of pits*[40]

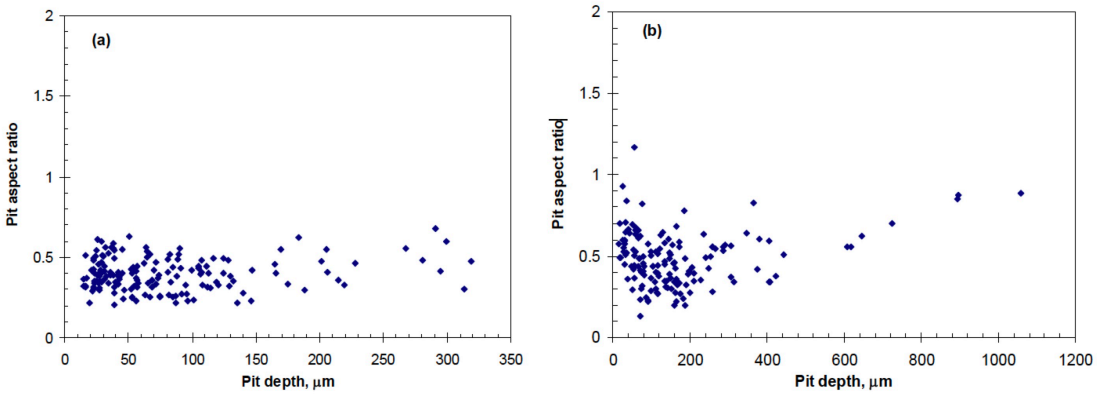



*Figure 3 The aspect ratio and depth distribution of pits that (a) did not transfer to cracks and (b) transfer to cracks on the pipeline steel specimens exposed to NNpH solution*[42]

Y. Kondo proposed another method to define whether a pit would transfer to a crack or not, and there are two conditions that a pit should satisfy[43]:

1. The threshold stress intensity factor decides a threshold value for depth, and the depth of pit should exceed that value.
2. The growth rate of crack should be larger than that of pit.

Y. Kondo' method is easier to be quantitatively analyzed. However, this method was developed for low-alloy steel tested in deionized water at 90 °C. The applicability of it on aluminum alloys in other conditions remains to be studied.

Not all the stress corrosion cracks need to initiate with the existence of pitting. The mechanism of these kind of cracks is intergranular or slip-dissolution processes. The intergranular corrosion results from the different chemistry between the grain-boundary and the bulk, while slip-dissolution-induced SCC is caused by the local corrosion of the slip planes[44].

## 2.3 Long cracks and small cracks

Environment-assisted cracks of different length can be divided into long cracks and small cracks, and they have different propagation mechanisms and different growth rate.

Long cracks usually refer to the cracks that are long comparable to the scale of grain, local plasticity or of a size more than 1 mm. There are many papers in the literature describing the growth rate of long cracks, generally using fracture mechanics parameters. Although important for some applications, experimental data obtained for long cracks does not describe the processes that are important for cracks that nucleate at pits or from smooth surfaces. This requires an understanding of small cracks.

Small cracks usually refers to the cracks that are of the length comparable to the scale of grain, local plasticity or less than 0.5-1 mm[45]. At the initiation stage of crack, it forms at the areas with high stress concentration[46]. Since the scale of it is small, it is complicated to describe the growth rate of small crack and only a few literatures mention their propagation. One researcher claimed that short crack behavior could be calculated by stress intensity factor K when there is a small scale yielding and by J integral when there is a significant yielding[47]. However, the paper did not clearly propose a relation between the growth rate and these factors.

In general, the growth rate of small cracks may be different from those of long cracks, since the crack tip is near the surface and it is more sensitive to the near-surface microstructure, electrochemical and mechanical properties.

## 2.4 6061-T6 aluminum alloy and 6061-T6 aluminum based composites with SiC nanoparticles

### 2.4.1 6061-T6 aluminum alloy

6xxx aluminum alloy is alloyed with magnesium and silicon[12], which enables them to undergo solution heat treatment. In addition, because of these two main alloying elements, 6xxx aluminum alloys have good corrosion resistance. The alloy composition of 6xxx is shown in Table 1. The 6061 aluminum alloy is the most commonly used of the 6xxx series aluminum alloys, having excellent weldability, mechanical and thermal properties (shown in Table 2). It is usually used in architectural extrusions.

Heat treatment is a technique used to alter the properties of materials. Common heat treatments include annealing, solution heat treatment, quenching and age hardening. Annealing is used to soften material, and solution heat treatment helps alloying constituents to dissolve in solution, while the quenching maintains the constituents in solution when the temperature decreases. Constituents are precipitated in the aging hardening process, improving the strength and hardness of material. The amount, size and distribution of precipitation depend on the aging temperature and time[48]. T4 and T6 are the two most common heat treatments of 6xxx series aluminum alloy. T4 heat treatment refers to solution heat treatment followed by natural aging. T6 heat treatment refers to solution heat treatment followed by artificial aging, resulting in a higher hardness and yield strength than T4[49].

*Table 1 The alloy composition of 6xxx aluminum alloy (by weight)*[50]

| | | | |
|---|---|---|---|
| Silicon | Minimum 0.4%<br>Maximum 0.8% | Zinc | No minimum<br>Maximum 0.25% |
| Iron | No minimum<br>Maximum 0.7% | Titanium | No minimum<br>Maximum 0.15% |
| Copper | Minimum 0.15%<br>Maximum 0.4% | Other elements | No more than 0.05 each,0.15% total |
| Manganese | No minimum<br>Maximum 0.15% | Magnesium | Minimum 0.8%<br>Maximum 1.2% |
| Chromium | Minimum 0.04%<br>Maximum 0.35% | Aluminum | 95.85-98.56% |

*Table 2 The mechanical and thermal properties of 6061-T6 aluminum alloy*[50]

| | | | |
|---|---|---|---|
| Vickers Hardness | 107 HV | Elongation at Break | 10% |
| Tensile Strength: Yield (Proof) | 270 MPa | Poisson's Ratio | 0.33 |
| Tensile Strength: Ultimate (UTS) | 310 MPa | Elastic (Young's, Tensile) Modulus | 71 GPa |

### 2.4.2 6061-T6 aluminum based composites with SiC nanoparticles

#### 2.4.2.1 General introduction to 6061 aluminum alloy based composites with SiC nanoparticle

Metal matrix composites (MMCs) have been widely developed and investigated over the past few decades. Generally, this class of materials consists of a metallic matric

and ceramic reinforcement[51]. Compared with traditional alloys, particle reinforced metal matrix composites have many advantages. They can be produced by various routes. For instance, J. Ghazi used a stir-casting technique to fabricate a Al-Si/SiC composite and found that with increasing of SiC volume fraction, ultimate tensile strength, yield strength and hardness increased, while the impact energy of the composite decreased[52]. V. S. Aigbodion et al. obtained the same conclusion in both the as-cast and thermally age-hardened samples of SiC particulate reinforced Al-Si-Fe matrix composite that was fabricated by a double stir casting route[53]. K. L. Meena et al. also tested the relation between mechanical properties and the weight fraction of reinforced SiC particles in a 6063 matrix/SiC composite, finding out that most mechanical properties, including the fracture strength, increased with the increase of reinforced particles weight fraction[54].

There are several kinds of reinforcement, that is, fibers, flakes or particles[55]. Compared with continuous fibers, discontinuous reinforcement has relatively low cost. Such composites can be formed using metal working methods[56,57]. However, A. J. Knowles et al. pointed that particle-containing MMCs were less ductile than fiber composites, and undesirable interfacial reaction and de-cohesion that may decrease mechanical properties in MMCs with particles[55].

Aluminum alloys are commonly used as the matrix for particle-reinforced composites, with SiC commonly used as the reinforcement phase: the aluminum alloy matrix gives low density, excellent corrosion resistance and ductility, while the SiC has high strength[58].

The size of the reinforcement also affects the properties of the composite. Compared with the micro-size SiC particles, the nano-size SiC particles are dispersed and distributed more uniformly after same mechanical alloying process[59]. Therefore, a

decrease in the reinforcement size increases the strength of the composite and decreases the matrix ligament size[60]. Salem et al. compared the properties of Al-SiC composites reinforced by SiC particles with the average size of 162 μm and 160 nm respectively, concluding that the nano particle reinforced composite has a higher thermal conductivity, electrical resistivity, and hardness[61].

#### 2.4.2.2 The effect of reinforced particles on corrosion resistance

Localized corrosion such as pitting can occur due to different electrochemical properties between the particles and the metal[62], and stress corrosion cracks may more easily initiate at these locally corrosive areas. K. Muna et al. used potentiostatic polarization to study the corrosion resistance of Al 6061 reinforced by SiC particles (with the average size less than 20 μm), finding that adding SiC particles increased the strength of material but decreased its corrosion resistance[63]. It is because the reinforcement content results in a cathodic area and a plastic strain from the thermal and mechanical expansion differences of matrix and reinforcement materials. Therefore, dissolution and hence pitting initiated easily in these areas. However, in this test, the 6061 aluminum based composite was only exposed to a corrosive environment but there was no applied load. Therefore, it only studied the effect of SiC reinforcement on corrosion instead of stress corrosion.

## 2.5 Methodology for SCC experiment

### 2.5.1 Specimen

In general, there are two types of SCC specimen, that is, smooth and precracked/notched specimen[64].

#### 2.5.1.1 Pre-cracked or notched specimen

A pre-cracked specimen has a machined notch, and it is a common specimen type in SCC testing. A notched specimen is also suitable for studying hydrogen embrittlement, because the triaxial tensile stress of the notch geometry can attract hydrogen atoms to the target area. Shallow notches are suitable for the study of surface effects whereas a deep notch can be used for hydrogen penetration[65]. Examples of various pre-cracked samples for SCC testing are shown in Figure 4[66]: The main advantage of pre-cracked specimen is that the stress is concentrated at the tip of notch, and therefore, the cracking would be localized around the notch tip. In addition, because of the larger stress that can be achieved at the notch, the failure process is accelerated[64]. Studies of crack growth rates for both small and long cracks can be conducted on notched specimens[67,68], but this approach is not suitable for thin products such as sheet, as the plasticity of crack tip needs to be confined to achieve high stress.

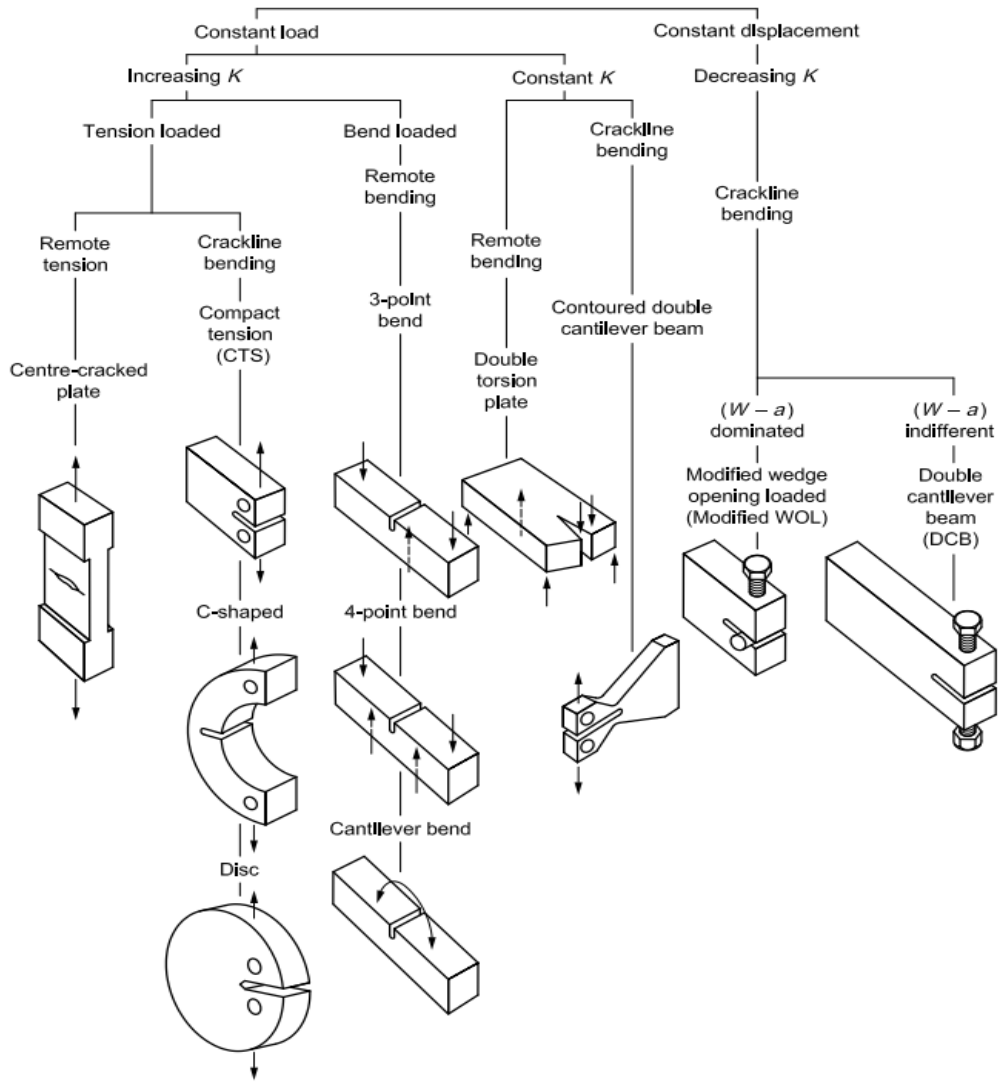



*Figure 4 Differenct types of pre-cracked samples for SCC test*[66]

The crack propagation rate could be described by stress intensity factor K. For the pre-cracked specimen, when under a constant load, K increases with increasing crack length. At different ranges of stress intensity factor, the sensitivity of the crack growth rate to the stress intensity factor varies, as shown in Figure 5[44]. It can be observed that in the second stage, the growth rate almost remains stable with increasing stress intensity factor due to rate-limiting environmental processes (for example, environmental species transport from up the crack to the crack tip).

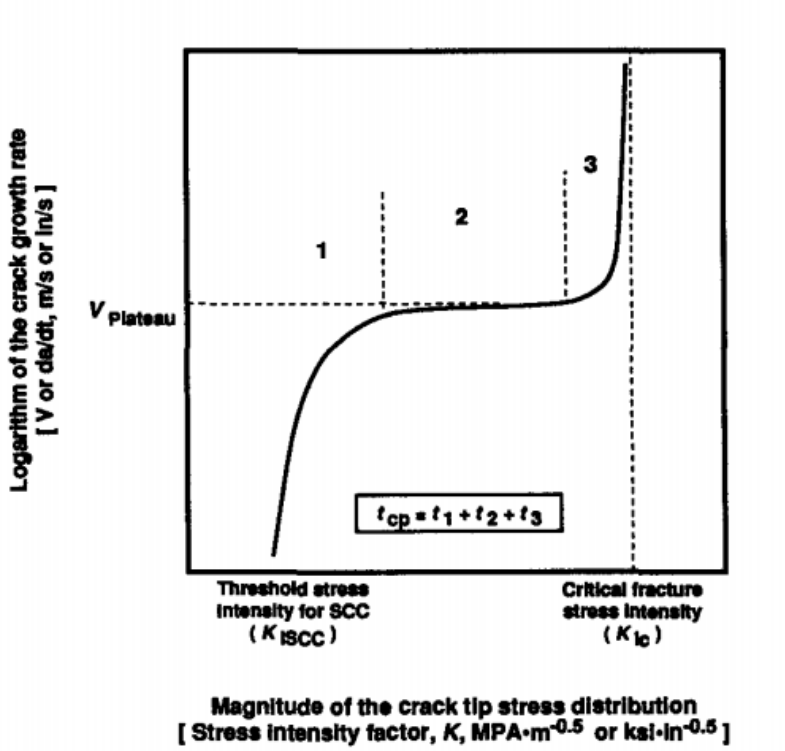



*Figure 5 The logarithm of crack growth rate versus the magnitude of the crack tip stress intensity for smooth sample under a constant load*[44]

#### 2.5.1.2 Smooth specimen

Compared with notched specimen, SCC test on the smooth specimen is used to study the total process of stress corrosion cracking including the nucleation of crack[64]. However, nucleation may take a long time even using higher corrosive concentration and loading than practical service. The smooth specimen is usually loaded under a constant strain, a constant load or a slow strain rate. In constant strain tests, it is usual to adopt a bent-beam specimen, U-bend specimen or C-ring specimen, whereas constant load test and slow strain rate test usually adopt tensile type specimens[69]. Figure 6 is the illustration of the relation between the time-to-failure and applied stress for a typical smooth sample statically loaded[44]. It could be concluded that the time-to-failure decreases with increasing stress. However, such tests give no

information on the growth rate of the cracks that nucleate and then propagate to cause failure over this time.

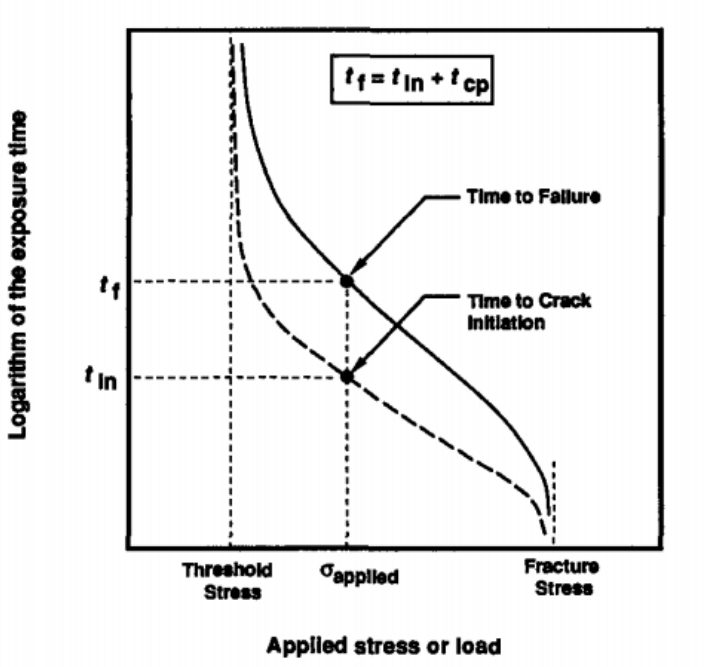



*Figure 6 The logarithm of time-to-failure and time-to-crack-initiation by SCC versus the initially applied stress/load for smooth sample*[44]

### 2.5.2 Corrosive environment and stress

Researchers use different methods to create corrosive environment and to apply load. Slow strain rate testing is a common method used in the SCC test, and the main characteristic of it is the low strain rate. It is quite critical to use this method to assess materials' immunity to cracking because the unsuitable strain rate will cover up the susceptibility of cracking. For example, R. Braun[21] immersed samples in 3% NaCl and 0.3% $H_2O_2$ aqueous solution and applied the strain at the rate from $10^{-7}$ to $10^{-3}$ $s^{-1}$ to conduct SCC tests on a range of aluminum alloys, comparing with the reference tests conducted in the dry air. Generally, there is a monotonic increase relation

between the strain rate and the log crack propagation rate for the face-centered cubic alloys[70].

When J. M. Drugli[71] et al. assessed the susceptibility to chloride stress corrosion cracking of highly alloyed duplex stainless steels and austenitic stainless steel, a C-ring specimen was adopted. The specimen was immersed in an electrolyte containing $Na^+$, $Ca^{2+}$, $K^+$, $Mg^{2+}$, $Cl^-$ and $SO_4^{2-}$. The load was applied through a compressed spring, and a constant temperature bath was used to keep a temperature range from 90 °C to 150 °C. He concluded that the saturated solution of $MgCl_2$ was more aggressive for chloride stress corrosion cracking (CSCC) than that of NaCl, since the chloride concentration is higher, and pH is lower in $MgCl_2$ solution. K. N. Lyon et al. also immersed 316Ti austenitic stainless steel in boiling magnesium chloride to conduct SCC tests[72]. Submerging the specimen in the electrolyte is convenient for long time tests. However, it is hard to observe the initiation and propagation of cracks. This may be achieved by applying salt deposits through droplet evaporation, which allow comparison of the behavior of the area under corrosive environment and that without it.

When T. Prosek et al. conducted the SCC test on the stainless steel, they applied six saturated chloride salt solution droplets on each U-bend specimen (Figure 7 (a)). After 4 weeks', 10 weeks' (Figure 7 (b)), or 22 weeks' exposure, the specimens were cleaned, and the corrosion deterioration were examined using optical and confocal microscope[73]. Although they created the corrosive environment by applying chloride droplets, which was convenient for the observation of the sample surface during the SCC test, they only investigated the corrosion deterioration of specimens after the SCC test.

H. S. Isaacs et al. captured images of the laser welded steel specimen surface to record its behavior in chloride solution. Then they used difference viewer imaging technique (DVIT) to investigate the difference between images captured at different stages of the experiment, and to present the change of the specimen surface[74].

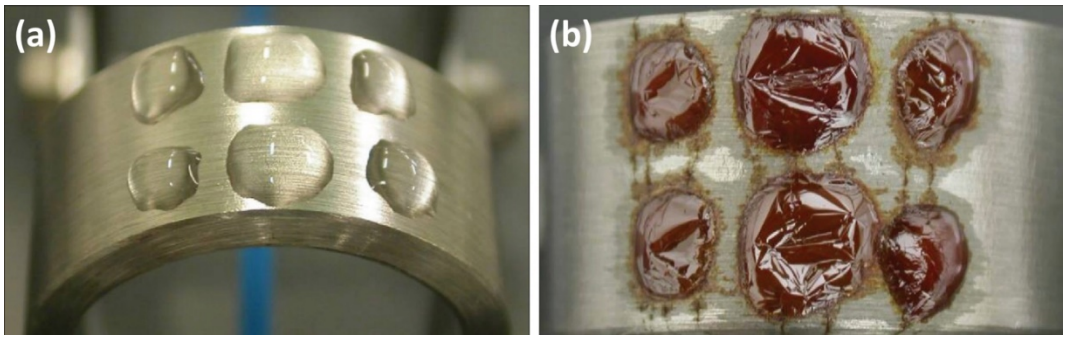



*Figure 7 The stainless-steel U-bend specimen with (a) the applied salt chloride droplets, and (b) the salt deposits after the 10 weeks' exposure at 40 ºC and 30% RH*[73]

Creating the corrosive environment by submerging specimens in the electrolyte solution is usually used to investigate aqueous corrosion, while that by applying salt deposits is used to study atmospheric corrosion. The main difference between them is that the applied salt deposits absorb moisture from the atmosphere and turn into droplets, causing a decreased oxygen concentration from the droplet edge to the center.

Evans investigated the corrosion of Fe specimen under NaCl droplets and found that the differential oxygen concentration resulted a higher pH near the edge than the center.

Near the droplet edge, because of the high concentration of oxygen, the dominant reaction is:

$O_2 + 2H_2O + 4e^- \rightarrow 4OH^-$

Near the droplet center, the diffusion of oxygen is inhibited by the solution, and therefore the dominant reaction is[75]:

$Fe \rightarrow Fe^{2+} + 2e^-$

$Fe^{2+} + H_2O \rightarrow FeOH^+ + H^+$

Therefore, a local cathode is developed around the droplet edge, while a anode is established in the center, which promotes the corrosion process[76]. Not only on stainless steel specimens, this phenomenon is also observed on aluminum alloy specimen[77].

### 2.5.3 Observation and analysis method

#### 2.5.3.1 Digital Image Correlation (DIC)

Digital image correlation is an optical method that is used to measure the differences between images. With the help of DIC, the displacement map and thus the strain map can be easily obtained. The principle of DIC is tracking of displacements by analyzing groups of pixels with a correlation algorithm. Therefore, if recording a series of digital images during the propagation process of cracks, DIC could show a continuous change of displacement and strain. However, there are some limitations and requirements for the DIC technique. The first one is that it generally can only measure the displacements and strain in plane, and out-of-plane movement may lead to an in-accurate result unless two-camera systems are used (so-called “3D-DIC”) or specialized optics. The second one is that for DIC technique, it is necessary to provide it with enough information to track and correlate, which means that it is not

suitable for many traditional SCC methods that involves submerging the specimen in the corrosive solution. A speckle pattern is necessary for DIC, and generally, there are two methods to treat the specimen's surface. The most common one is applying white matt paint first to provide a white background and then, fine and uniform black speckles for DIC to track. The second one is applying random scratches[78].

P. L. Reu et al. used DIC to measure the crack growth of the 6061 T6 aluminum alloy pre-notched specimen under tension, analyzing the strain field to track the crack tip position[79]. A. Cook et al. conducted a similar experiment on stainless steel to detect stress corrosion crack growth beneath a deposited salt film, and the optical images and strain maps calculated by DIC are shown in Figure 8[80].

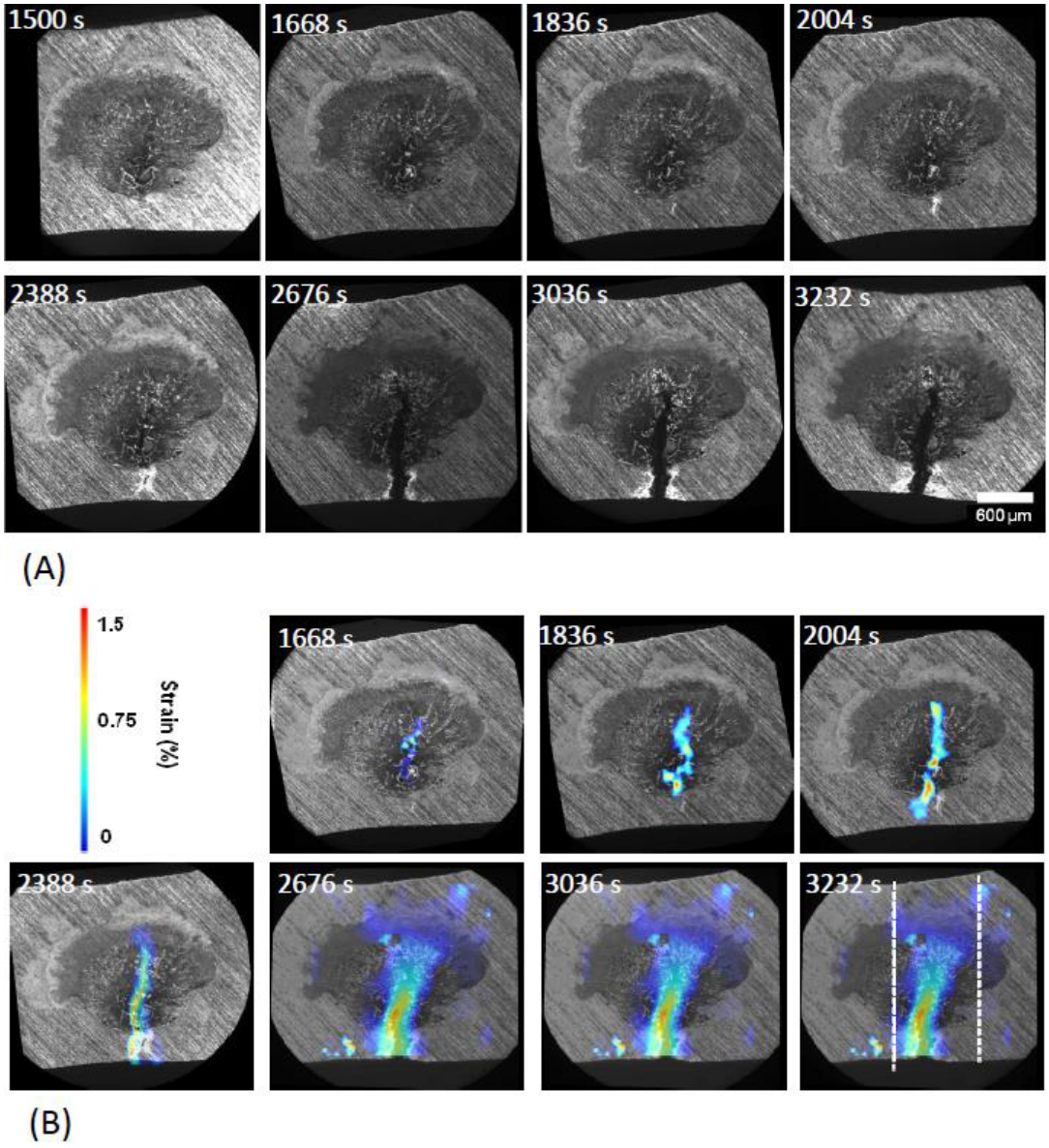



*Figure 8 (a) Time series optical images and (b) strain maps obtained by correlating corresponding optical images to the first image (captured in 1500s) of 304 stainless steel tested under a salt-deposit* [80]

### 2.5.3.2 X-ray computed tomography (XCT)

X-ray computed tomography is a non-destructive 3D technique that can visualize the interior of materials, and it has been used to study SCC in steels and aluminum. XCT can be used for both in-situ and ex-situ SCC experiment. For instance, B. J. Connolly

et al. conducted the in-situ corrosion experiment on AA2024-T351 FSW specimens to investigate its localized corrosion using X-ray tomography for 48 h, and during the test, the specimens were immersed in the corrosive environment. They also conducted the ex-situ corrosion experiment on AA2024 specimens. These specimens were corroded for 1, 3 and 5 days before being scanned, and the X-ray tomography was used to visualize the pits and stress corrosion cracks on specimens after corrosion[19].

Singh et al. performed in-situ SCC test on under-aged 7075 aluminum alloy pre-notched specimen and used X-ray synchrotron tomography to study the small stress corrosion crack development. Virtual sections of the tomography images could be used to illustrate the growth process of the stress corrosion crack over time at constant load, as shown in Figure 9[81].

T. J. Marrow and L. Babout et al. used high resolution X-ray tomography to conduct in-situ SCC test on sensitized 5083 aluminum alloy. The specimen was applied a constant tensile load in an environmental cell containing 3.5% NaCl solution during the scanning, and an Ag/AgCl electrode was used to monitor the potential. In this test, localized corrosion and intergranular cracking were successfully observed on specimen[82].

C. Ornek and D. L. Engelberg conducted the in-situ SCC test on the DSS grade 2202 and 2205 stainless steel wires. Specimens were exposed to $MgCl_2$ atmospheric environments under 50 ºC and 30% RH for 21 months, and the time-lapse XCT was used to observe and measure the corrosion rate[83].

D. A. Horner et al. studied the stress corrosion behavior of turbine disc steel, at stresses below yield and in a simulated steam-condensate. The ex-situ XCT was used to examine the pits and cracks of the pre-exposed specimens. Examples of the SEM

and XCT image of the sample are shown in Figure 10[84], in which it could be seen that most cracks start from the edge instead of the base of pit.

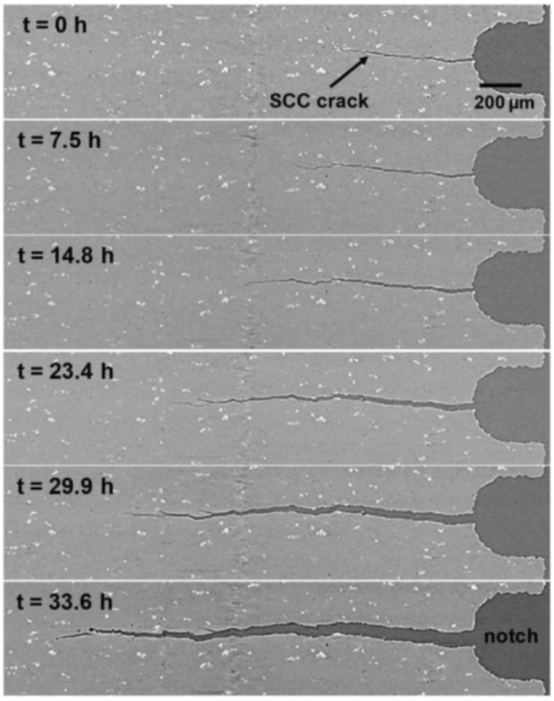



*Figure 9 The time series X-ray tomography images of the stress corrosion crack growth for a specimen under constant load*[81]

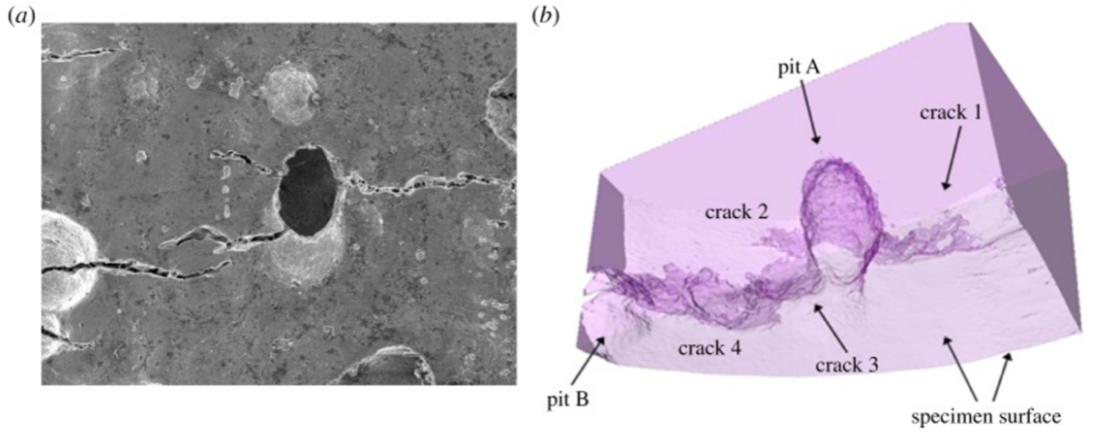



*Figure 10 (a) The SEM image and (b) the X-ray tomography image of a steel specimen when applied a load of 90% of the yield stress and exposed at 90 °C for 7173 h, showing multiple cracks developed from a pit* [84].

Compared with surface observations used for DIC, XCT provide 3D data. In addition, XCT could detect interior cracks while DIC could only analyze the crack on the surface. Furthermore, Digital Volume Correlation (DVC) technique can be used to process the XCT datasets, and to calculate the displacement in 3-dimension. T. J. Marrow et al. used X-ray microtomography in the fatigue experiment of the annealed Elektron 21 magnesium alloy. DVC was used to analyze the μXCT dataset for 1000, 3500 and 10250 cycles with the reference dataset of 500 cycles, obtaining the crack opening displacements in 3-dimension[85].

For the in-situ XCT experiment, although XCT could be used for qualitative analyses, the exposure time would also affect the detected size of crack, especially for short cracks. Besides, since the crack growth rate is relatively small at the initial stage, there is a challenge of maintaining beam source and exposure conditions.

For the ex-situ XCT experiment, as discussed before, if an XCT dataset is scanned before the corrosion experiment as the reference, the crack opening displacement of stress corrosion crack can be calculated with the help of DVC technique. However, the ex-situ XCT experiment is not suitable for the test that requires the observation of in-operando conditions.

## 2.6 Conclusion

The general mechanisms of SCC in aluminum alloys are understood, but there are only a few literatures about the initiation of short stress corrosion cracks. Such studies are needed to develop an understanding of the growth rates of short stress corrosion cracks. Various techniques including DIC and XCT have shown that they may be suitable to study short cracks. This project therefore aims to develop a method to study the development of short cracks. The chosen material is a 6061 T6

aluminum, which may suffer from atmospheric stress corrosion cracking under some conditions. These have not been quantified reliably, and this may be done using in situ observation. This alloy can be strengthened by the addition of SiC nanoparticles, but there is no data for the effect of this on stress corrosion cracking. This study will therefore examine the behavior of a SiC nanoparticle reinforced 6061 aluminum based composite.

# 3 Experimental Methods

## 3.1 Materials

6061 T6 aluminum alloy and SiC nano-particle reinforced 6061 T6 aluminum based composite were used in this test. Standard 6061 T6 aluminum alloy sheet with the thickness of 0.040" (1.016 cm) was purchased from LAS Aerospace Ltd, and the chemical composition provided by the supplier is shown in Table 3. The SiC nano-particle reinforced 6061 T6 aluminum alloy was produced by Prof. Marina Galano's group (University of Oxford) and contained 15% (by weight) of SiC nano particles with the average diameter less than 500 nm. It has been extruded into a bar with a diameter of 7.5 mm using a Fogg & Young extruder. The extrusion ratio was 14:1, and the extrusion speed was 8 mm/s. After the extrusion, solutionizing was performed at 525°C for 1 h followed by water quenching, and then artificial ageing at 125 °C for 8 h followed by air cooling.[58]

*Table 3 The chemical composite of commercial 6061 T6 aluminum alloy (% by weight)*

| | Si | Fe | Cu | Mn | Mg | Cr | Zn | Ti | Others Each | Others Total |
|---|---|---|---|---|---|---|---|---|---|---|
| Spec.min | 0.40 | - | 0.15 | - | 0.80 | 0.04 | - | - | - | - |
| Spec.max | 0.80 | 0.70 | 0.40 | 0.15 | 1.20 | 0.35 | 0.25 | 0.15 | 0.05 | 0.15 |
| Actual | 0.75 | 0.43 | 0.23 | 0.13 | 0.87 | 0.18 | 0.05 | 0.03 | 0.02 | 0.03 |

## 3.2 Characterization

### 3.2.1 Hardness

Following the guidance of ASTM E92-82[86], the Vickers hardness values of the 6061 T6 aluminum alloy and the SiC nano-particle reinforced composite were measured under room temperature with a 5 kg load applied. The specimens' surface was ground with #1200 grinding paper before the hardness test. The hardness test was conducted six times for each material and the average value is adopted as the Vickers hardness of material. The sample standard deviation was calculated as Equation 2.

$$Equation\ 2 \quad S = \sqrt{\frac{1}{N-1}\sum_{i=1}^{N}(x_i - \bar{x})^2}$$

where $x_i$ is the sample value, N is the number of the sample, and $\bar{x}$ is the average value of the sample.

### 3.2.2 Yield stress

The specimen was cut from 6061 T6 aluminum alloy sheet and was machined into standard tensile specimen shape according to ASTM E8/E8M – 09[87] by a Global Cutting Technologies Model 1212 water-jet cutter. The cutting width is 0.7 mm, and the cutting speed is 100 mm/min. The sample geometry is shown in Figure 11.
In order to allow displacement measurements by digital image correlation, the specimen was firstly coated with a layer of matt white paint (James Briggs Ltd.) to create a matt surface. Then, fine black speckles were applied through a Timbertech airbrush with the black ink (H. Schmincke & Co). It was loaded in tension by a Shimadzu machine with P/N 346-52653-01 loading rig with a capacity of 5 kN. The tensile test was conducted at the rate of 1 mm/min, and the force change during the

elongation process was monitored. A GOM-Aramis 5M two-camera DIC system was used to capture 64-bit monochrome optical images during the tensile process with the exposure time of 127 ms. Each captured image was 2448 x 2050 pixels. Two cameras observed the specimen with a field of view of 65mm x 55mm since it is suitable for the tensile specimen size. The cameras were set and calibrated with CQ/CP20 55 x 44 cube (Figure 12 (a)), after they had been set up with a distance between two cameras of 284 mm with an included angle of 25°. The front surface of the specimen was perpendicular to the center of two cameras with a distance of 730mm between them (Figure 13). Images were taken at the rate of 1 image per second, and the pixel size is 27 μm/pixel. The images were then correlated with the image of the unloaded sample using the Aramis digital image correlation software v6.3.0, with the subset size of 19 pixels and step of 15 pixels. This subset size and step size enable sufficient accuracy and resolution without much cost of computation time. Figure 14 is the schematic diagram of the subset size and the step size. When correlating two images, one square region in the reference image is selected as the yellow square shows, and the software tries to find a similar region containing the same features in another image. This square is called a 'subset'. The distance between the centers of subsets is the step size.

Since only the sample surface was applied speckles, only this area can be correlated and obtained displacement maps, and the size of the displacement maps is about 12 x 55 mm. After obtaining maps of the surface displacements, data of the load at different stages was imported into Aramis and use the in-built tensile-test analysis script, the stress-strain curve as well as the yield stress were obtained.

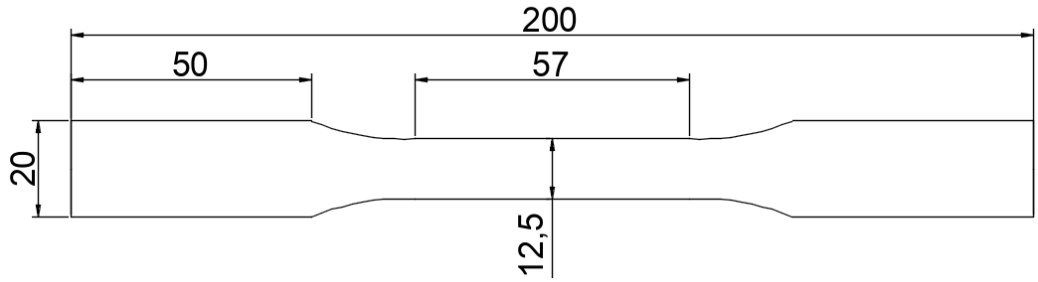



*Figure 11 The schematic diagram of tensile specimen (all dimensions in mm)*

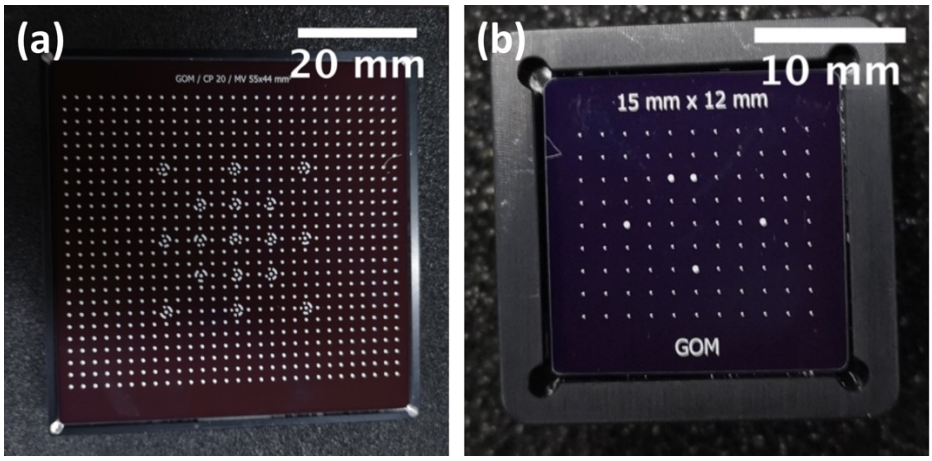



*Figure 12 The calibration cube (a) CQ/CP20 55 x 44 and (b) CQG4146*

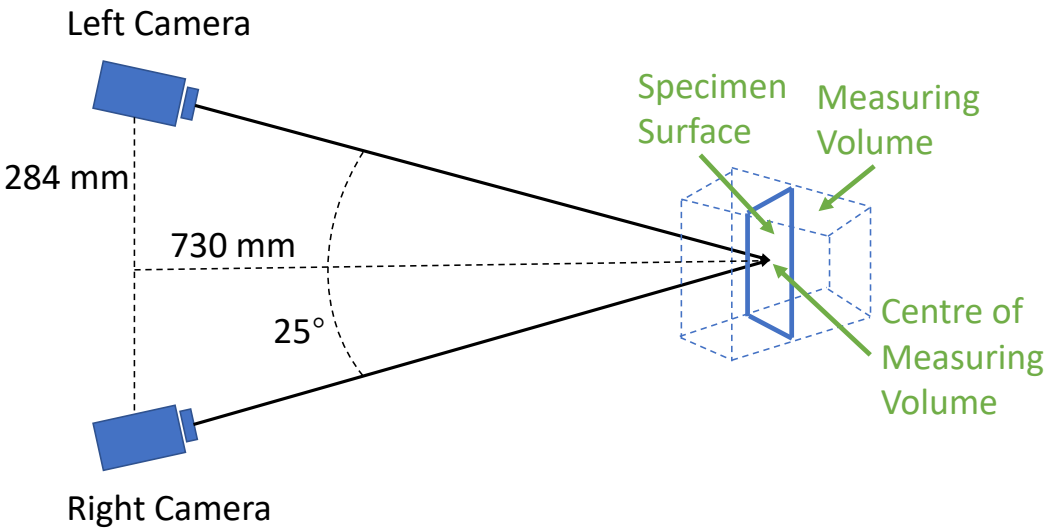



*Figure 13 The schematic diagram of the experiment set up*

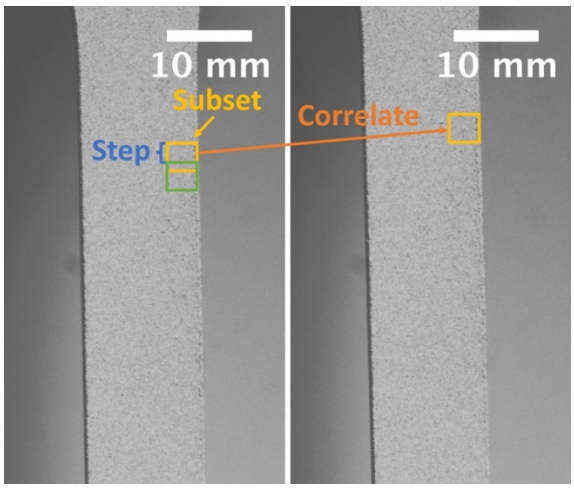



*Figure 14 The schematic diagram of the subset size and the step size*

### 3.2.3 X-ray Diffraction (XRD)

XRD was carried out with the help of Dr. Philip Holdway to analyze the texture of material and to investigate if the texture could be changed by annealing. Two 15 mm x 15 mm square coupons were cut from the aluminum alloy sheet. One was put in a Carbolite furnace at the temperature of 550°C for one hour and then cooled down within the furnace, while another one remained as-received. The XRD machine was a BRUKER D8 ECO with copper radiation, 1.5406 Å wavelength, 40 kV working voltage, 25 mA working current, 10-100° 2 theta scan range and 1 °/min scan rate. The obtained XRD curves and the ratio of characteristic peaks were compared with standard PDF cards to investigate texture.

## 3.3 Preparation for stress corrosion cracking test

### 3.3.1 DIC error test

For digital image correlation, reducing the subset size will result in higher spatial resolution of the displacement map and greater error in the measurement of the displacement vectors[80]. Therefore, testing was conducted to select a suitable subset size. One square coupon sample of the aluminum alloy with a size of 10mm x 10mm was cut from the aluminum sheet, followed by grinding with #1200 grinding paper. Then, it was immersed in acetone and ethanol successively, cleaned in Kemet ultrasonic cleaner for 10 minutes respectively. Random scratches were introduced by #1200 grinding paper as shown in Figure 15.

The coupon was then put under the Zeiss Axiophot optical microscope to capture two optical images. An aperture of 8.5 and magnitude of 2.5 x 2 were used (magnitude of ocular lens and objective lens respectively). These two images were taken under exactly the same condition with a transition of about 0.5 mm between them to introduce a rigid body movement. After being imported into the LaVision Davis software, a subset size ranging from 5 to 49 pixels with the increment 4 was used to correlate them, and the standard deviation of the total displacement maps obtained with each subset size was adopted as the system error.

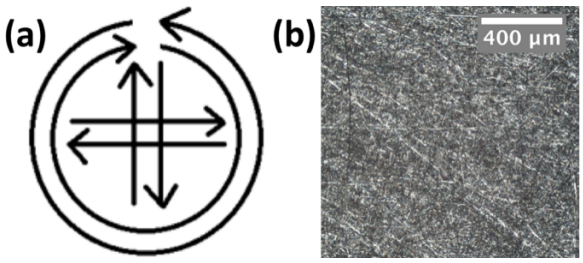



*Figure 15 (a) The schematic diagram of the random scratches applying method, and (b) the applied random scratches on the specimen surface*

### 3.3.2 Calibration of the proving ring

Proving rings were used in the stress corrosion experiments to apply a constant and symmetrical load. They were machined from 316L stainless steel by Manchester University. The external diameter, width, thickness and elastic limit were 60 mm, 15mm, 2.96 mm and 1200±40 N respectively[80]. Before using the proving ring to load specimens for stress corrosion tests, a calibration test was conducted to verify its diametral change under different loads. A layer of matt white paint (James Briggs Ltd.) was applied on the front side of the proving ring, followed by black speckles applied through airbrush, as for the tensile specimens (Figure 16). The 5 kN Shimadzu P/N 343-08095 fixed compression plate was used to apply a series of compressive loads ranging from 0 N to 1100 N with the increment of 50 N. The GOM-Aramis camera was used to capture images of the proving ring at each load. The selected field of view was 65 mm x 55 mm, and it was calibrated with CQ/CP20 55 x 44 cube, as before. Only the front side of the ring was selected for the DIC correlation, which was done using a subset of 19 pixels and step of 15 pixels (the pixel size is 27 μm/pixel). After obtaining displacement maps, the data from two small areas containing 141 displacement vectors on the left and right edge of the proving ring were selected for analysis. The difference between their average values for displacement x was calculated as the horizontally diametral change. Similarly, the difference between the average values for displacement y of two areas on the top and bottom was calculated as vertical diametral change.

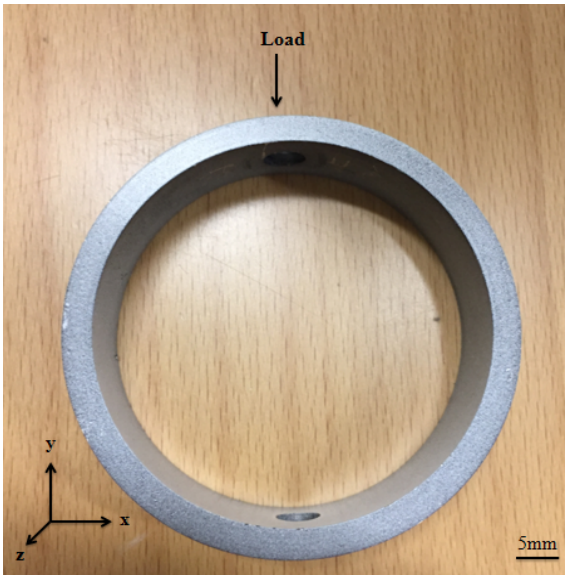



*Figure 16 The surface of the proving ring and the loading direction*

### 3.3.3 Specimen preparation

#### 3.3.3.1 Specimen manufacture

Since the 6061 T6 aluminum based nano composite was extruded into a bar with the diameter of 7.5 mm, it was firstly cut into a 1.1 mm-thick sheet through the middle of the bar by the workshop of Materials Department (Figure 17). Then, both the aluminum alloy sheet and aluminum based composite sheet were machined into taper-shaped specimens using the Global Cutting Technologies Model 1212 water-jet cutter (Figure 18) with the cutting speed of 100 mm/min. The gauge section was the same shape for both materials, with a taper angle of 6°.

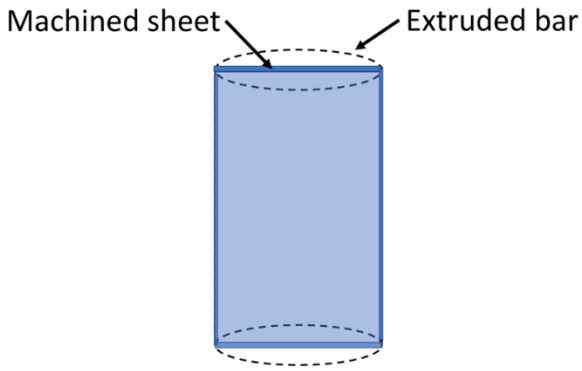



*Figure 17 The schematic diagram of the extruded bar and the sheet machined from it*

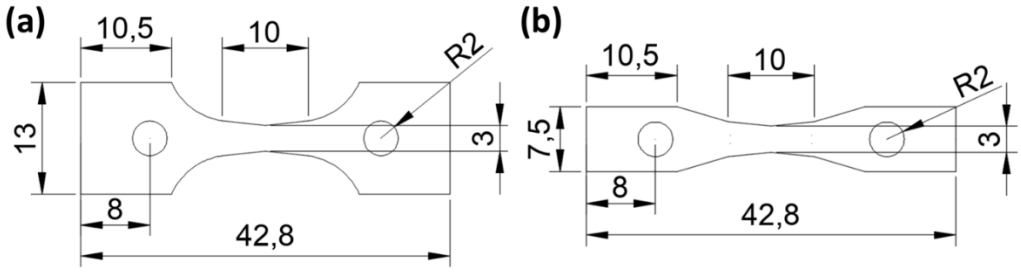



*Figure 18 The schematic diagram of the (a) aluminum alloy specimen and (b) alloy based composite specimen (all dimensions in mm)*

### 3.3.3.2 Grinding and random scratches

To introduce random scratches for DIC, each specimen was fixed to the grinding sample holder using Crystalbond 509-3 Adhesive (Agar Scientific), with sample heating on a Stuart SB160 hotplate. Then it was ground for 5 minutes using Metkon Forcipol 2V grinding machine at the rate of 100 revolutions/min with #1200 SiC grinding paper. By heating the holder, the specimen could be removed, and the adhesive was cleaned off by immersion in acetone and ethanol successively, then cleaning in a Kemet ultrasonic cleaner for 10 minutes respectively. Random scratches were then applied manually using #1200 SiC grinding paper.

### 3.3.4 Strain check

In order to examine the strain distribution of tapered specimens in the SCC test, tensile tests were conducted on the tapered specimen of 6061 T6 aluminum alloy and 6061 T6 aluminum based composite (Figure 18). They were ground with #1200 grinding paper, and then was coated with a layer of matt white paint produced by James Briggs Ltd. Fine black speckles produced by H. Schmincke & Co. were applied through a Timbertech airbrush. Shimadzu P/N 346-52653-01 loading rig was used to apply a load of 948 N to the 6061 T6 aluminum alloy specimen and a load of 1050 N to the aluminum based composite specimen. Aramis 5M was used to capture 64-bit monochrome optical images before and after loading with the exposure time of 127 ms. The captured image is at the size of 2448 x 2050 pixels. The field of view of two cameras was selected as 25mm x 20mm, and the cameras were set and calibrated with CQG4146 cube (Figure 12 (b)). The calibration deviation of the GOM Aramis was 0.033 pixels. After correlation, the average strain of an area of 3 mm x 3 mm at the center and end location of each specimens were calculated.

### 3.3.5 Pre-pitting

The stress corrosion cracking tests were conducted on both pre-pitted specimen and non pre-pitted specimen. To determine the conditions for pre-pitting, six square coupon samples at the size of about 30 mm x 30 mm were cut from aluminum alloy sheet. On each of them, 30 salt deposits were applied. Each salt deposit was applied by the evaporation of 5 µl of $MgCl_2$ (95.21 g/mol) aqueous solution. The diameter of the droplet is around 3 mm. The $MgCl_2$ concentration of the solution is 6.48 g $dm^{-3}$ which would therefore turn into the deposit with the $MgCl_2$ density of 460µg•$cm^{-2}$ after evaporation[80]. The salt deposit then would absorb moisture in equilibrium with

the environment and produce a saturated aqueous solution film on the surface. The magnesium chloride hexahydrate (Fisher Scientific) was weighed using a Mettler Toledo electronic scale and was then dissolved in deionized water (Chemiphase Ltd.). The solution was heated to 60 °C using a Stuart US152 Metal Coated Hot Plate Stirrer. After 10 minutes of heating and stirring, a SciPette micro pipette was used to transfer 5 µl of the $MgCl_2$ aqueous solution from the beaker to the sample surface. After applying the droplets, the specimens were put in the Weisstechnik environmental chamber (see next section) at a temperature of 40 °C and relative humidity of 0 % for ten minutes to be evaporated.

The pitting test was conducted in the environmental chamber at the temperature of 40 °C and relative humidity of 30 %. At the 1st, 2nd, 4th, 8th, 16th and 32th day of corrosion, one coupon sample was taken out of the environmental chamber. Then the salt deposits were removed by immersing the coupon sample in 100 °C hot water and putting it in ultrasonic cleaner for 10 minutes. The Zeiss Evo MA10 scanning electron microscope (SEM) was used to examine the surfaces, with the images then used to determine the optimal time to develop pitting (i.e. 16 days). The SCC specimens prepared for pre-pitting were similarly ground, with random scratches and salt deposits applied, and were placed into the environmental chamber for 16 days.

## 3.4 Stress corrosion cracking test

### 3.4.1 Loading of the test specimens

The load was applied by the proving ring according to the guidance of ASTM G 49[88]. Firstly, the specimen was loosely fixed in the proving ring by pins at two ends. Then the proving ring was fixed into a loading jig that had been designed to

minimize the application of torque. The jig has a groove in the middle, in which the pins that went through the proving ring and specimen were located. This restricted the horizontal movement and twisting of the proving ring during loading process. Two clamps applied a compressive load to the proving ring that could increase the friction between it and the measuring equipment and therefore prevent movement. The sides of the proving ring were contacted by two dial-indicators with the graduation of 0.0001" (2.54 μm), and the change in these was used to measure the total horizontal diameter change of the proving ring (Figure 19). The load was applied by manually turning the bolts at two ends using a spanner until the diameter change reached the value required to apply the desired load, based on the calibration test.

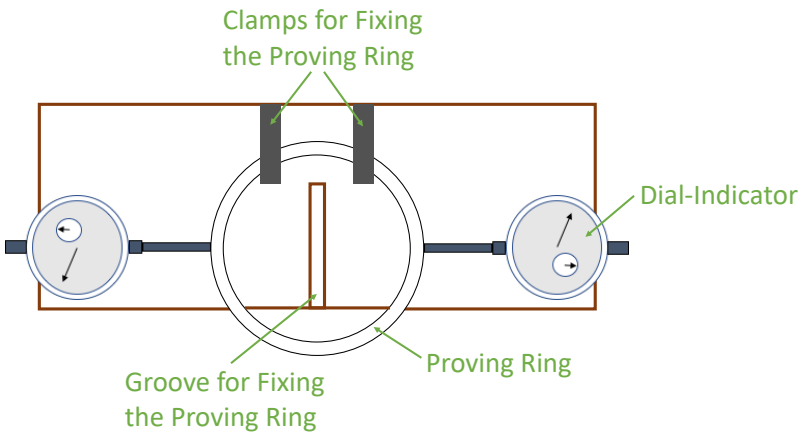



*Figure 19 The schematic diagram of the loading jig*

### 3.4.2 Proving ring holder for optical observations

A proving ring holder was machined from an aluminum plate to fix the location of proving ring during the periodic optical observations of the SCC tests, and so allow reliable repeat images. The plate are of 6 mm thickness and there are three supporting 1 mm diameter balls stuck to its by Permabond glue. There was one hole

of 4 mm diameter and one horizontal groove in the middle of the plate allowing the proving ring pins to go through. For proving rings under different loads, the distance between two pins varies, and the groove makes the holder suitable for all loads. The groove on the bottom is of the length of the metal strip on the sample holder of optical microscope, which had a Vernier gauge to measure position (Figure 20). Therefore, the proving ring holder could move with the movable metal strip and the location could be recorded by the vertical and horizontal scales on the sample holder.

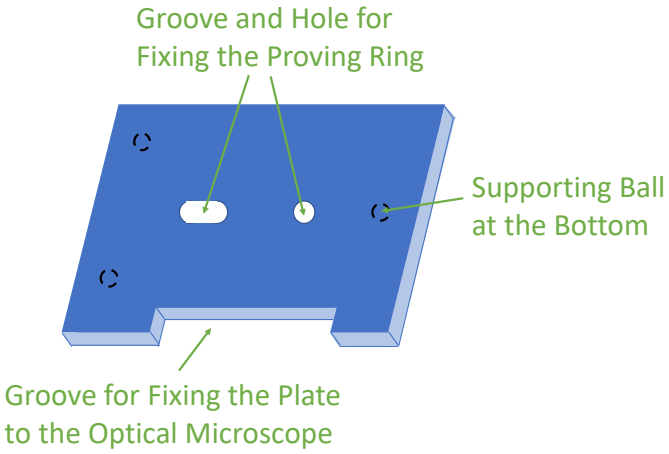



*Figure 20 The schematic diagram of the proving ring holder*

### 3.4.3 Strain distribution check

For each material, identical tapered specimens were loaded by the Shimadzu and by the proving ring respectively to compare the strain distribution obtained by the different loading methods. Both specimens were ground with #1200 grinding paper. The tapered specimen for the Shimadzu was coated with a matt white paint layer and black speckles, while the one for the proving ring had random scratches applied by #1200 grinding paper. The optical images of specimens before and after loading were taken and then analyzed by DIC. For the specimen that was loaded by the Shimadzu, the images were captured and correlated using the GOM Aramis system,

while those of the specimen loaded by the proving ring were captured by optical microscopy and correlated using the LaVision Davis software. In this latter case, the proving ring that contained the specimen was removed from the microscope for loading, while the Shimadzu loaded specimen was observed in situ.

### 3.4.4 Salt deposit application

On each SCC specimen, three salt deposits were applied using the same method as described in 3.3.4 (Figure 21). The distance between each deposit is about 3 mm. Since the tapered angle of the tapered specimen is 6°, the applied stress of the center salt deposit location is 1.2±0.1 times of that of two end locations.

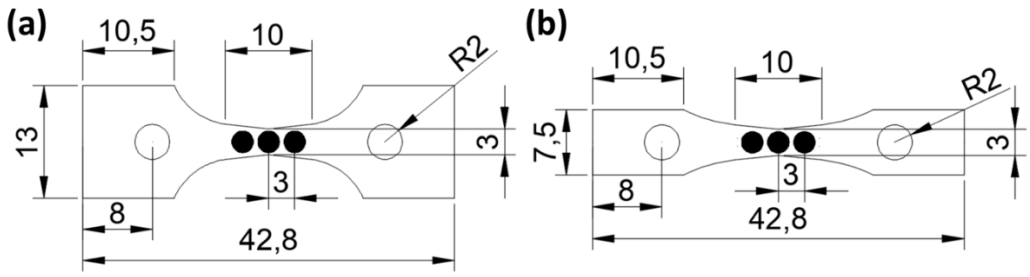



*Figure 21 The schematic diagram of salt deposits locations on (a) alloy specimen and (b) alloy based composite specimen, and the black circles indicate the applied salt deposits*

### 3.4.5 Temperature and humidity

The stress corrosion cracking tests were conducted at 40 °C and 30% relative humidity which was maintained in a Weisstechnik environmental chamber (Figure 22). The chamber is equipped with two temperature sensors and one humidity sensor (manufacturer calibration). One temperature sensor is fixed in the back of the chamber to monitor the temperature of the whole chamber, while another one is

movable, and can be placed near the sample to monitor the real temperature of that area. The calibration of temperature sensors involved two steps: 1. Put two sensors at the same place to investigate the initial difference between them under 40 °C; 2. Put a pot with water in the chamber, and then put the mercury thermometer and the movable sensor in the water under room temperature. After 15 minutes, check the difference in the temperature that they detected respectively. The temperature tested by the standard thermometer was set as the reference. According to the result, the temperature tested by the movable sensor is 1.2 °C lower than the standard value, while that tested by the fixed sensor is 1 °C higher than the standard value. Therefore, in the SCC test, the temperature of the environmental chamber which is controlled by the fixed sensor was set to 39 °C. The location of the specimen and sensors in the experiment is shown in **Error! Reference source not found.**.

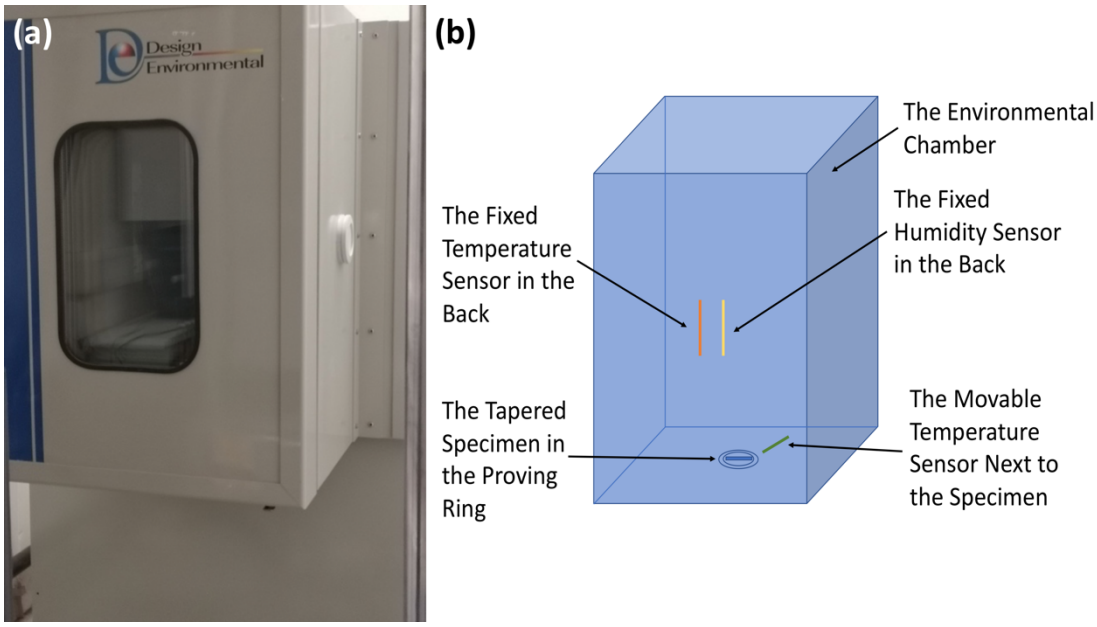



*Figure 22 (a) The environmental chamber and (b) the schematic diagram of the specimen and sensors location*

### 3.4.6 Optical images recording

During the stress corrosion tests, each specimen was removed from the chamber to capture optical images by Zeiss Axiophot optical microscope. The total time of removal was 40 minutes per observation. A 2.5 × 2 magnification was adopted, and the observed field of view (2560 x 1920 pixels) had a resolution of 0.65 μm/pixel. Each salt deposit was observed using nine overlapped images in a 3 x 3 array, where the overlap distance was about 150 μm.

## 3.5 Data analysis

### 3.5.1 Digital image correlation

Pairs of optical images recorded at the same location were imported into the LaVision DaVis 8.4.0 software to map the displacement changes. The import parameters were as follows. Firstly, in the Camera attributes section, the number of camera was selected as 1, the number of frames was 1 and pixel size was 0.65 μm. Secondly, in the AcqTime attribute section, since the images were captured every day, the time between images was 24 hours ($8.64 \times 10^{10}$ μs). Thirdly, for the attributes of processing, the correlation mode was 'relative to first', the maximum expected displacement was 500 pixels, the subset size was 33 pixels with a step of 5 pixels. For each set of images, nine points were selected as the starting points (Figure 23), distributing both on the non salt-covered area and salt-covered area.

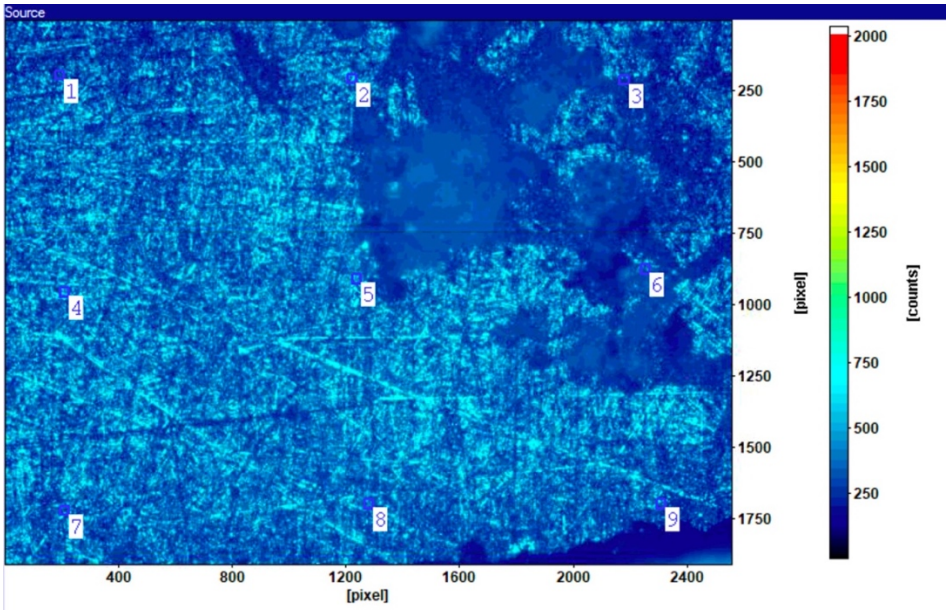



*Figure 23 Nine starting points of image correlation (exported from DaVis software)*

### 3.5.2 Translation and rotation removal

Although the scale on the optical microscope was used to determine the location and the proving ring holder was machined to restrict rotation, there were still slightly unavoidable translation and rotations between images captured at different times. These could introduce displacements that were large compared to the real relative displacements of the specimen. As the final data analysis required the displacement field, it was necessary to remove these translations and rotations. An existing Matlab code was adapted for this. Firstly, the displacement maps were exported from Davis as DAT file, which contains the x and y coordinates of each point and the relative displacement in x and y direction at that point. Since there were some areas such as the area of pitting could not be correlated, the coordinates of points in these areas were not in the DAT file. Therefore, secondly, the coordinates of all such points were created in the DAT file and the displacements of them were set to NaN (i.e. “not a number”). Thirdly, the translation was removed by subtracting the average

displacement vector from all points. The rotation was removed using existing code written by Matthew Jordan (Oxford University). K. Shoemaker stated that the rotation could be represented using Quaternions which is a four-coordinate system. Compared with Euler Angles, it requires fewer elements to describe rotation[89]. This code adopts this principle, finding the rotation center and removing the rotation by solving rotation matrix. In order to remove the effect of extreme values and background noise, 2D median filtering was firstly used to smooth data, and the average value and rotation center were then calculated. Then they were applied to treat the non-filtered original data and obtain a rotation corrected result.

### 3.5.3 Displacement map stitching

Each salt deposit was covered by nine overlapped optical images, as depicted in Figure 24. The DIC analysis considered pairs between successive observations at the same location (e.g. “lu”), and only provided the relative displacements between them.

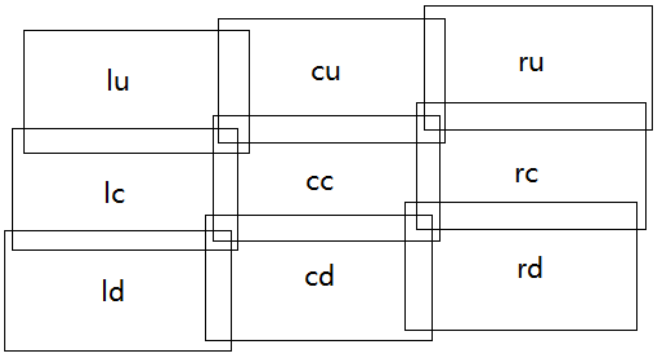



*Figure 24 Typical layout of overlapping images and the notation used to refer to them: "l", "c" and "r" for left, center and right, "u", "c" and "d" for up, center and down*

In order to measure the relative positions of the images, the origin (0,0) was defined at the middle of the central image (marked as cc), and then the relative translations of the four surrounding images (lc, rc, cd, cu) could be obtained. For the four images in the corners (lu, ld, ru, rd), the relative translation of these was taken as the average value obtained from the two adjacent images (e.g. cu and rc used for ru). In order to put all the images in the same coordinate system, the original central coordinate of each image was added its corresponding relative translation. Consequently, the points in the overlapped areas should have the same coordinate in the different images. However, the displacements of these points obtained from different images were not exactly the same which would cause pixel or sub-pixel size steps in the stitched maps and displacement field. Hence, in the overlapped area the displacement difference between images was the average value of displacement difference of each point. In order to reduce the effect of extreme values on this average value, any points where the displacement difference of separate points was larger than 50 pixels was set to NaN and so was not used to calculate average value. This method was

encoded using Matlab and a threshold for displacement difference between images was set at ±20 pixels. If the calculated value beyond threshold, it was reported by the code and the analysis of that pair of images was abandoned.

For the pre-pitted specimens, the procedure of calculating the displacement differences that was outlined above is summarized in Figure 25. However, for the non pre-pitted specimens, it was found there was a large area in the cc images that could not be correlated. Hence, only the other 8 images were stitched together, and the procedure was as described in Figure 26. Then for each image, the displacement data was added by the calculated relative displacement difference. For any points having the same coordinate in the overlapping datasets, the displacement was calculated as the average value.

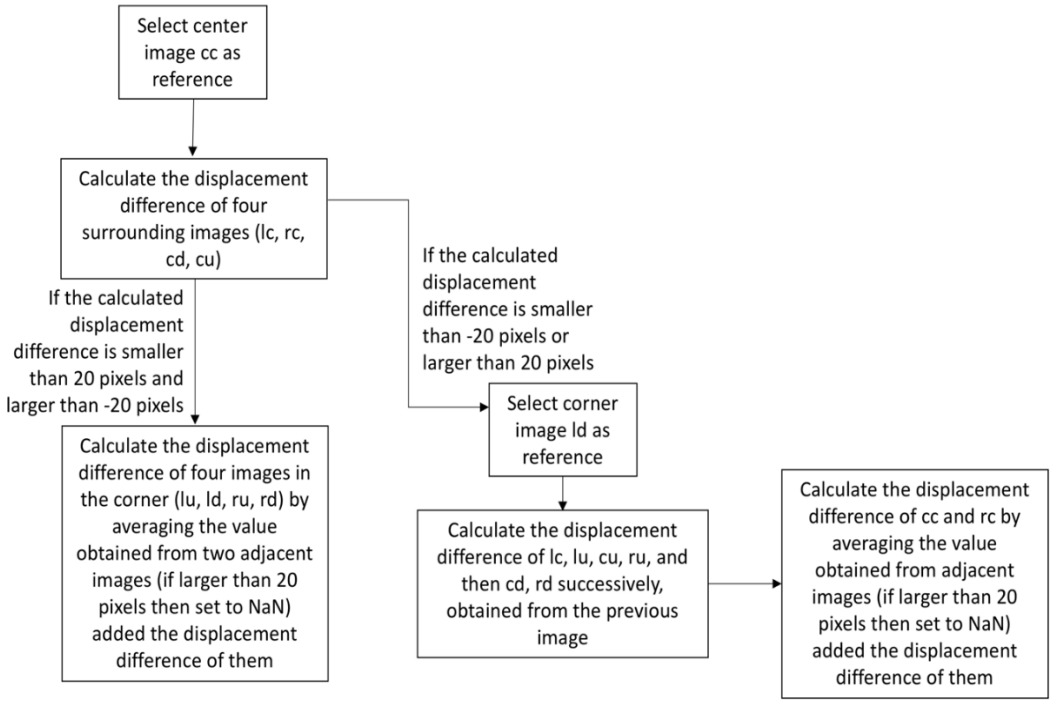



*Figure 25 The procedure of calculating the displacement difference for pre-pitted samples*

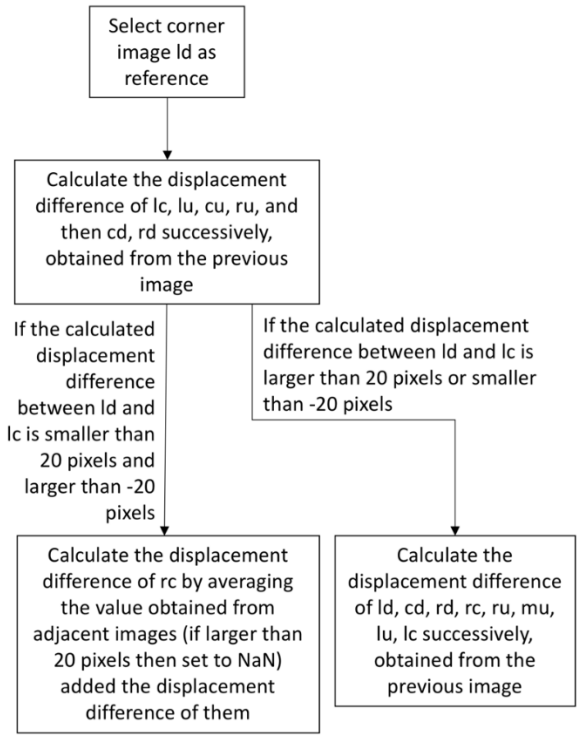



*Figure 26 The procedure of calculating the displacement difference for non pre-pitted samples*

### 3.5.4 Strain calculation

A horizontal band with the width of 40 image pixels (8 points on the displacement map) in the middle of the stitched data was selected to calculate the specimen's extension along the load direction (x direction). For each x coordinate, the corresponding displacement value was the average x-displacement of all points (if they had a value) that had the same x coordinate but different y coordinate. Thus, the trend for x-displacement change along x-axis was obtained. In order to remove noise in the obtained displacements, the application of various filters over different measurement spans were investigated: 'lowess' uses linear regression, 'loess' uses quadratic regression, 'rlowess' uses robust linear regression, rloess' uses robust

quadratic regression, 'sgolay' uses a quadratic polynomial, ‘remove average’ and ‘median’ filter calculate the average and median value of the data respectively. The ‘rlowess’ filter, with a span size of 150 was selected as optimal. Each data is smoothed by robust linear regression over 150 neighboring values. The smoothed curve was interpolated with a x coordinate interval of 1 x $10^{-3}$ using the Matlab command ‘interp1’. This command calculates the y values of interpolated points by linear interpolation of neighboring points. The gradient (strain) of the displacement curve at each point was then calculated. The gradient values were then plotted as a function of the original x coordinates. The average of the central set of 400 values (over a distance of about 1.3 mm) was used as a measure of the strain over the salt deposit location, while the standard deviation of these values was calculated as the measurement error. The same process was used to calculate the average strain in the y-direction using a vertical band with a width of 40 pixels.

### 3.5.5 Scanning Electron Microscope (SEM) and X-ray Tomography

After the stress corrosion cracking tests, the specimens were immersed in hot water and then put in an ultrasonic cleaner for 10 minutes. After drying, the Zeiss Evo MA10 SEM was used to observe the specimen surfaces at 7.0 mm working distance, 5 kV working voltage, and 50 pA working current. The number of cracks was counted, and their openings were approximately measured from the image.
X-ray tomography in the Xradia Versa 510 X-ray Microscope was then used to scan the specimen. The working voltage was 110 kV, the power was 10 W, the current was 90.8 µA, the exposure time per radiograph was 17 sec, the binning was 1, the objective was 4X, the field mode was normal, the source filter was air, the obtained resolution was 2.11 µm/pixel, and there were 1601 projections over 360° rotation.

The specimen was held vertically in the Deben CT5000 loading rig, which could be used to apply a load to the specimen.

Each tomograph was reconstructed with a secondary reference image that was captured with the same working parameters but without specimen, using the microscope software (XM3DViewer 1.2.8. Scout-and-Scan$^{TM}$ Control System Reconstructor). Both the center salt deposit location and one end salt deposit location of one non pre-pitted sample and one pre-pitted sample were scanned. They were imaged without load and then with a tensile load applied. In the loaded condition, a load of 900 N was applied to the aluminum alloy specimen, and 1000 N to the alloy based composite specimen. SEM examination was used again after X-ray tomography to search for minor cracks that might have appeared after loading.

# 4 6061 T6 aluminum alloy

The chapter represents the microscopic and macroscopic characteristics of 6061 T6 aluminum alloy. The stress corrosion cracking tests of 6061 T6 aluminum alloy were conducted under the constant load and corrosive environment, and the effect of applied strain and pre-pitting on SCC behavior is discussed.

## 4.1 Characterization of 6061 T6 aluminum alloy

### 4.1.1 Hardness

The measured Vickers Hardness are 126 HV, 130 HV, 127 HV, 128 HV, 125 HV and 124 HV. The average of these six impressions is 127±2 HV.

### 4.1.2 Tensile test

In order to measure the yield stress of 6061 T6 aluminum alloy, tensile tests were conducted on the standard tensile specimens. Example strain maps are shown in Figure 27. In this example, the Young's modulus (67.64 GPa) and 0.2% yield stress (265 MPa) were calculated by the software, shown on the right corner of the image. The stress-strain curve, plotted by Matlab from the DIC data, is also shown in Figure 28. To verify the GOM analysis, the elastic deformation range of the curve was fitted using 'polyfit' command of Matlab which is in a least-squares sense. The yield stress measured by the 0.2% offset strain method is 266.0 MPa. The calculated yield stress of other two tests is 263.2 MPa and 261.5 MPa respectively. The average yield stress of the 6061 T6 aluminum alloy is thus 263.2±1.7 MPa, while the error is the sample standard deviation of three tests results.

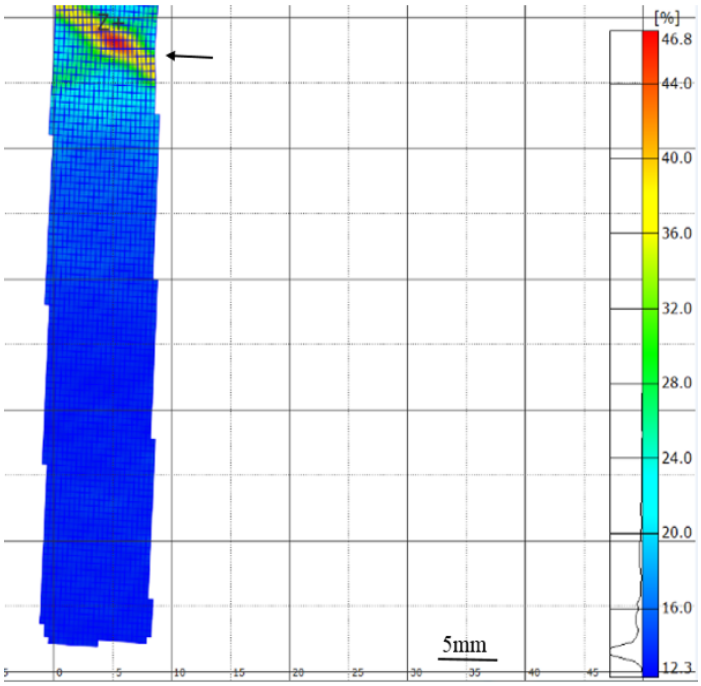



*Figure 27 The distribution of the strain along the loading direction of the standard tensile specimen at 4000 N. The black arrow indicates the location of strain concentration where the failure develops. The sample failed at 4100 N*

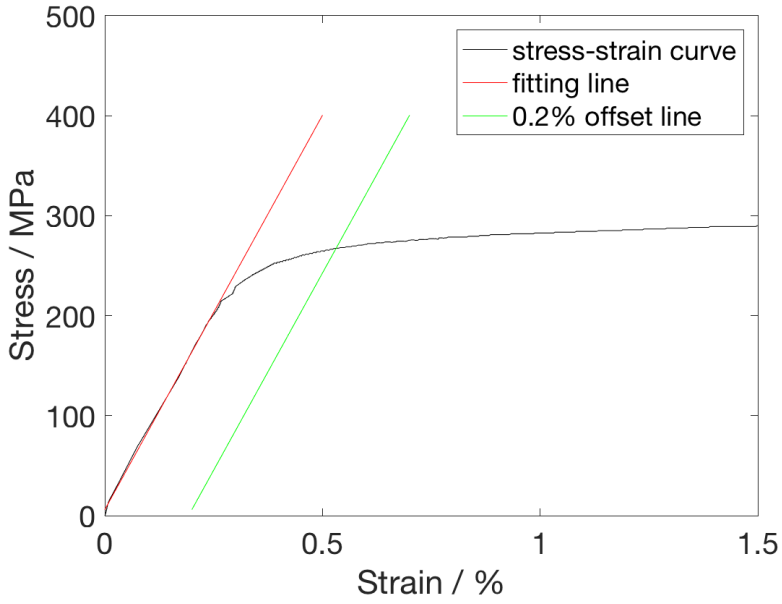



*Figure 28 The stress-strain curve extracted and drawn by Matlab. The black line represents the stress-strain curve, the red line is the fitting line and the green line is the 0.2% offset line*

In order to examine the strain distribution of tapered specimens in the SCC test, tensile test was also conducted on the tapered specimen of the 6061 T6 aluminum alloy. The sample was prepared and tested using the same method employed for the tensile tests of the standard tensile specimens.

Two areas at the size of 3 mm x 3 mm at the center and one end location (i.e. the locations to be used for droplet placement in the SCC tests) were selected for investigation, as shown in Figure 29. It can be observed that after loading, the selected area at the center location is elongated more than that at the end location. The average strain of the two areas is calculated, and the change of it with the increase of applied load is shown in Figure 30.

Under 948 N (the load applied to the 6061 T6 aluminum alloy specimen in the SCC test), the average strain of an area of 3 mm x 3 mm at the center location is 9.0±2.0%, and that at the end location is 1.5±1.0%.

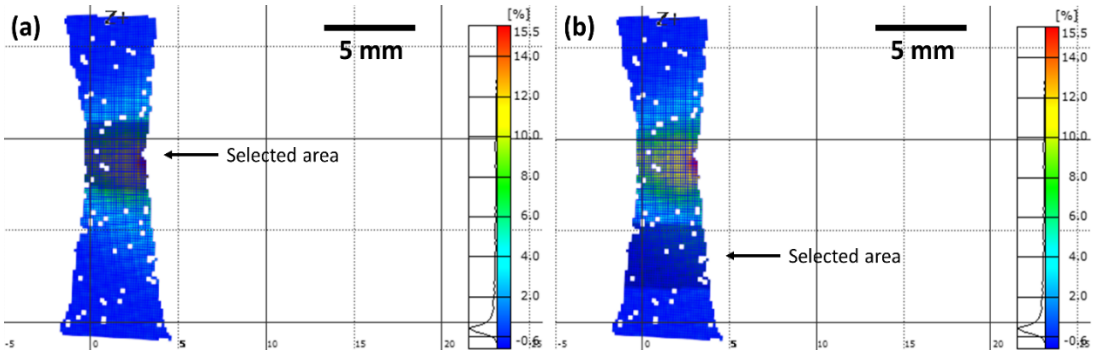



*Figure 29 The map of strain of 6061 T6 aluminum alloy specimen along the perpendicular direction (loading direction) under 948 N. (a) The area selected at the center location, and (b) the area selected at the end location. The blank areas are the areas that cannot be correlated*

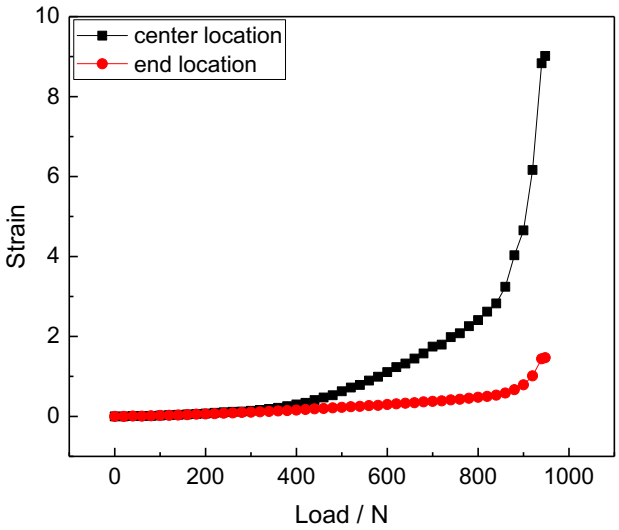



*Figure 30 The strain for two locations of 6061 T6 aluminum alloy specimen under different loads*

### 4.1.3 X-ray Diffraction (XRD)

XRD data from as-received and annealed samples are shown in Figure 31 and Figure 32. In both samples, aluminum peaks were found at 38.5°, 44.7°, 65.1°, 78.2° and 82.4°, corresponding to the (111), (200), (220), (311) and (222) planes. Besides, several small peaks corresponding to the $Al_2Fe$ phase and $Al_8Fe_2Si$ phase were found in both figures. After annealing, $Mg_2Si$ peaks were observed at 24.3° and 40.2° (corresponding to the (111) and (220) planes respectively).

Figure 33 shows the texture of two specimens, compared with a standard pattern for the aluminum. It can be observed that the annealing process did not remove the texture, and both the as-received and annealed samples were mainly textured in the (200) direction.

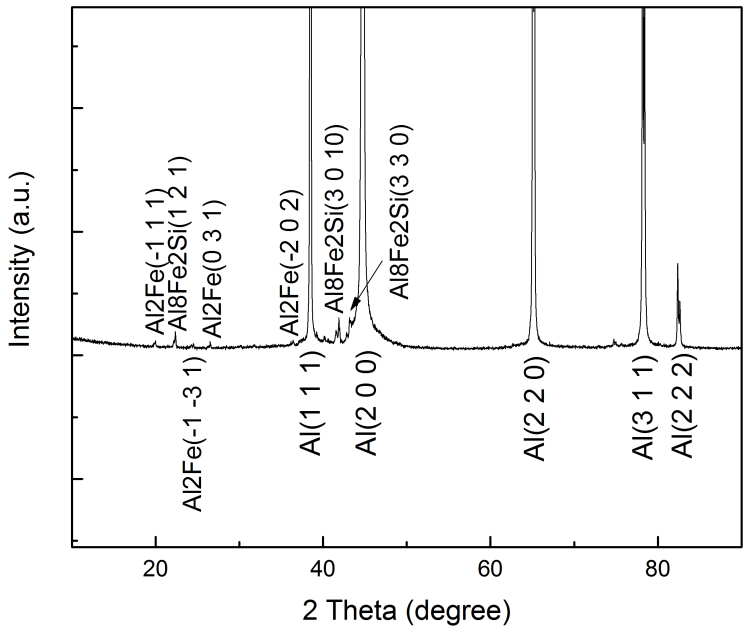



*Figure 31 XRD of the as-received specimens*

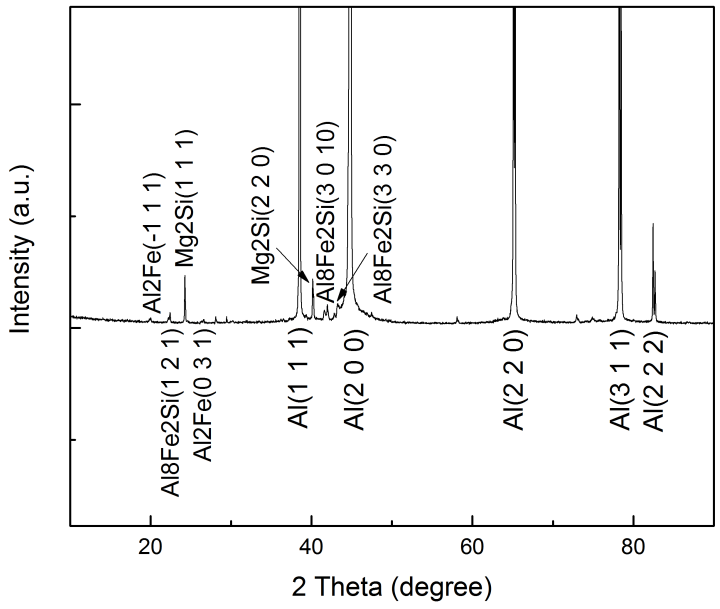



*Figure 32 XRD of the annealed specimens*

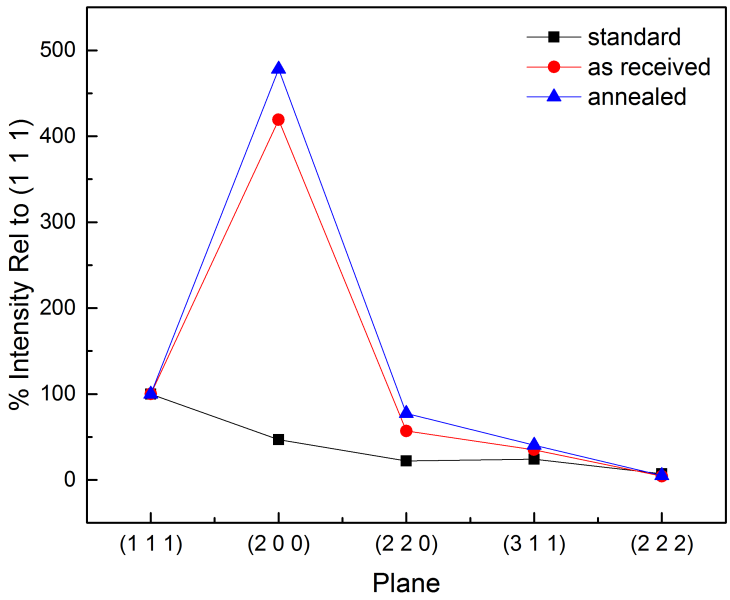



*Figure 33 The texture of as-received and annealed specimens*

## 4.2 Preparation for stress corrosion cracking test

### 4.2.1 DIC error test

#### 4.2.1.1 DIC error induced by surface treatment methods

Five coupon samples with a size of 10 mm x 10 mm were machined to test the DIC error caused by different grinding papers. One was single ground with #400 grinding paper, others were sequential ground from #400 to #600, #800, #1200 and #2500 respectively (Figure 34). Random scratches were introduced by the final grinding paper. Two optical images were taken of each surface, and they were processed by Davis using the subset size range from 5 to 49 pixels with an increment of 4 pixels. Since there is only a slight transition but no rotation between images, the standard deviation of the displacement map was regarded as the displacement measurement error. The relationship between the logarithm of the subset size and the logarithm of the error is shown in Figure 35. In general, the DIC error for each surface decreases with the increase of the subset size. It can be observed that there is no significant difference between the DIC error of the samples treated with different grinding papers, especially when using a subset size larger than 21 pixels. Since the sample treated with #1200 grinding paper has a relatively small error under each subset size, it was chosen to grind the sample.

Two other coupon samples at the size of 10 mm x 10 mm were prepared. One was single ground with #1200 grinding paper, and another remained as-received. Both of them had random scratches applied by #1200 grinding paper. Then they went through the same process as mentioned before to calculate the DIC error under different subset sizes, and were compared with the sample that was sequentially

ground from #400 to #1200. Figure 36 shows that under most subset sizes, the sample that was single ground with #1200 grinding paper has the lowest DIC error. Single grinding is also easier than sequential grinding, so single grinding and the application of random scratches with #1200 grinding paper was chosen as the method of sample treatment. When choosing 33 pixels as the subset size, this method would cause an DIC error of 0.031 pixels.

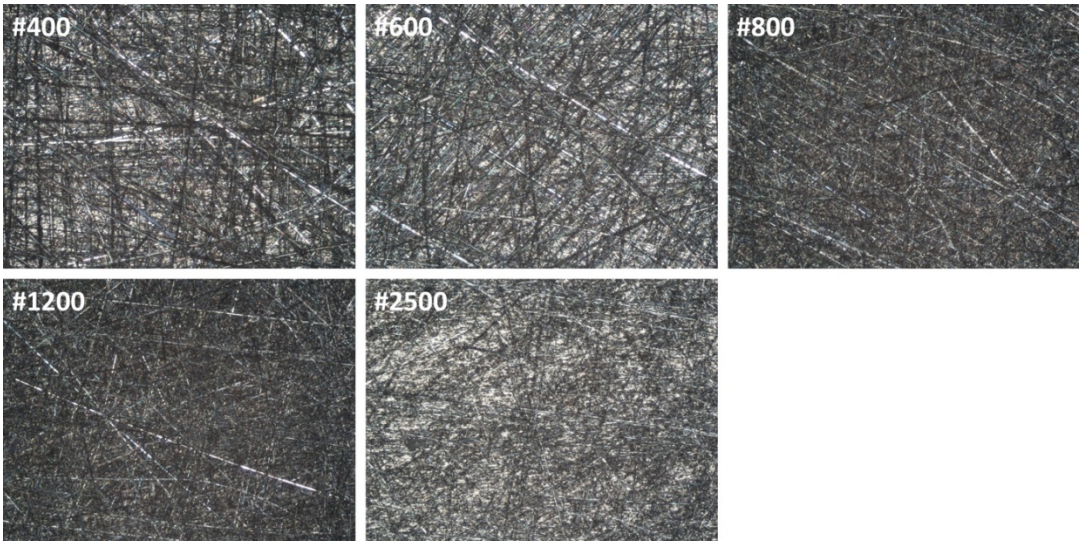



*Figure 34 The optical images of surfaces single grinded with #400 grinding paper and sequential grinded from #400 to #600, #800, #1200, #2500 respectively, the field of view is 1664 x 1248 μm*

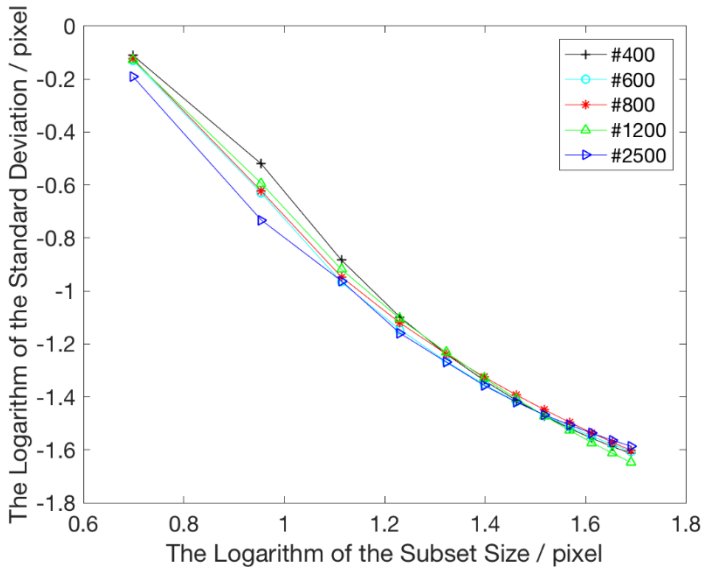



*Figure 35 The change of the standard deviation of the displacement map along with the increase of the subset size for different grinding papers*

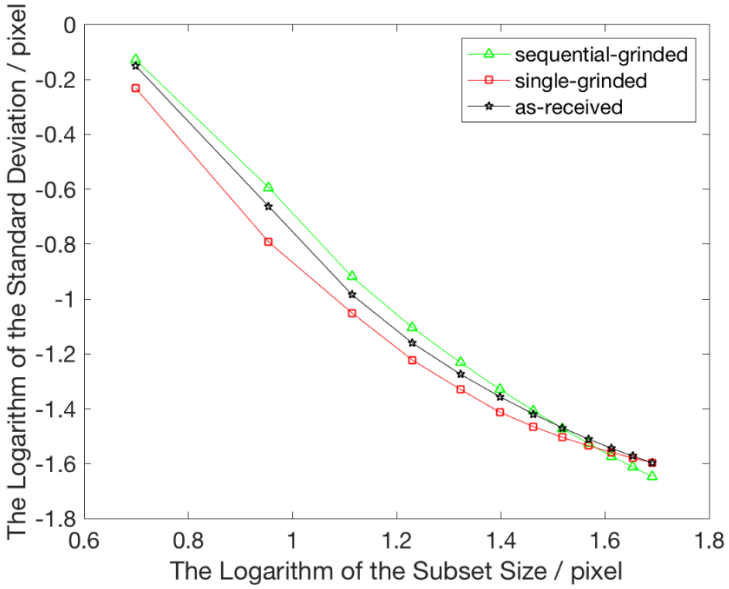



*Figure 36 The change of the standard deviation of the displacement map along with the increase of the subset size for sequential grinded, single grinded and as-received surfaces*

#### 4.2.1.2 DIC error induced by light change and focus change

For the stress corrosion cracking test, optical images of the specimens were captured every day. Since the optical microscope was reset each at each observation, there was a slight difference in the light and focus expected between observations, although care was taken to record images with the same aperture and illumination at the optimal focus.

In order to assess the DIC error introduced by the light change, one tapered specimen was ground, and random scratches were applied with #1200 grinding paper. The reference image was taken at the aperture of 8.45. Nine images were captured as aperture was adjusted from 8.0 to 8.4 and another nine images were captured at an aperture ranging from 8.5 to 8.9, with the increment of 0.05. They were correlated with the reference image with the subset size of 33 pixels, and the standard deviation of the displacement map was calculated as the DIC error. The DIC error for different apertures is shown in Figure 37. It can be observed that the DIC error increases with the increase of the aperture difference between the correlated image and the reference image. Besides, with the same aperture difference from the reference image, the lighter image has a larger error than the dark one. The DIC error for the images captured under the aperture of 8.85 and 8.9 reaches 3, which is too large to show in Figure 37.

Similarly, in order to assess the DIC error introduced by the focus change, one reference image was taken at the focus under the aperture of 8.5. 20 images were captured over a range of $\pm 20$ μm from the focus. The calculated DIC error is shown in Figure 38, which increases with the increase of the distance from the focus point.

In order to simulate the image capturing process, an optical image of tapered sample was captured in the focus with the aperture of 8.45. Then it was removed, and the optical microscope was reset. Later, the sample was replaced and another optical image was captured. In order to minimize the rotation during this process, the specimens were mounted in the jig, described in the experimental methodology, that was also used for the optical image capture in the SCC test. The two images were correlated, and the standard deviation of the displacement map was the DIC error introduced at the resetting and replacement process. Figure 39 shows the calculated DIC error using different subset sizes. When using 33 pixels as the subset size, the DIC error is 1.92, which is larger than the sum of the DIC error that could be introduced by significant changes in the light and focus. This error is caused by the rotation between images introduced during the replacement of the sample on the microscope stage. This is clearly shown in the displacement field, which has not been corrected for rotation (Figure 40). In the SCC test, the aperture variance between images was within ±0.5, and the focus difference was within ±10 μm.

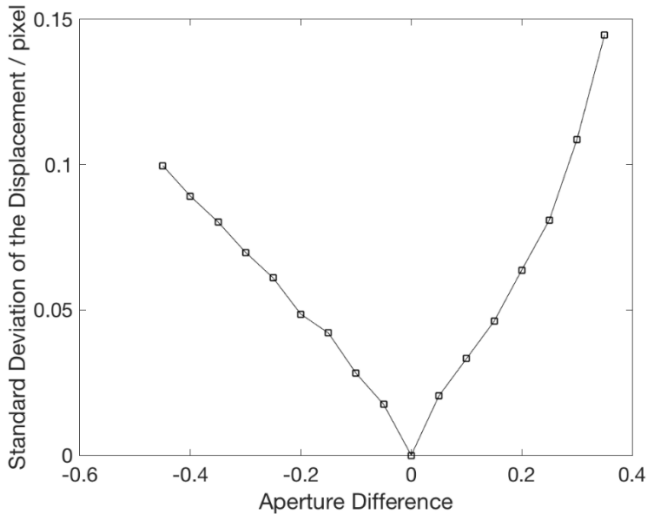



*Figure 37 The relation between the DIC error and the aperture difference*

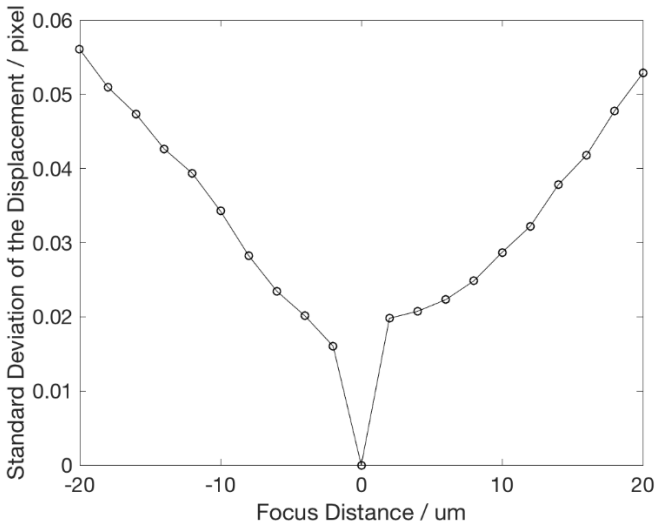



*Figure 38 The relation between the DIC error and the focus difference*

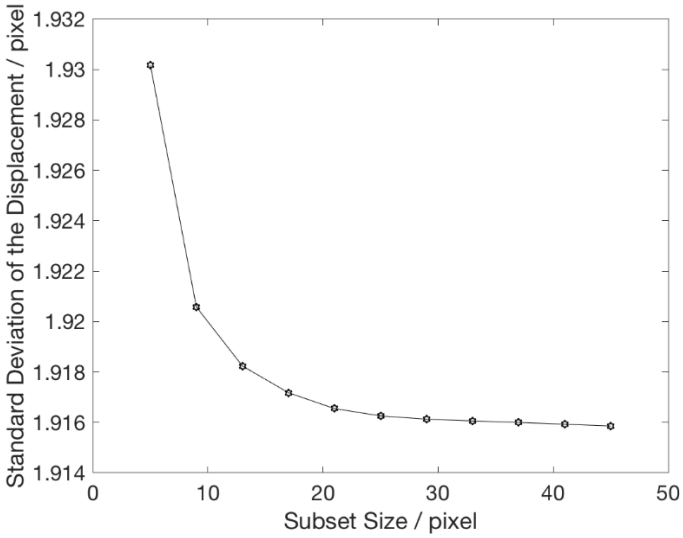



*Figure 39 The change of the DIC error along with the increase of the subset size for the remove & replace images correlation*

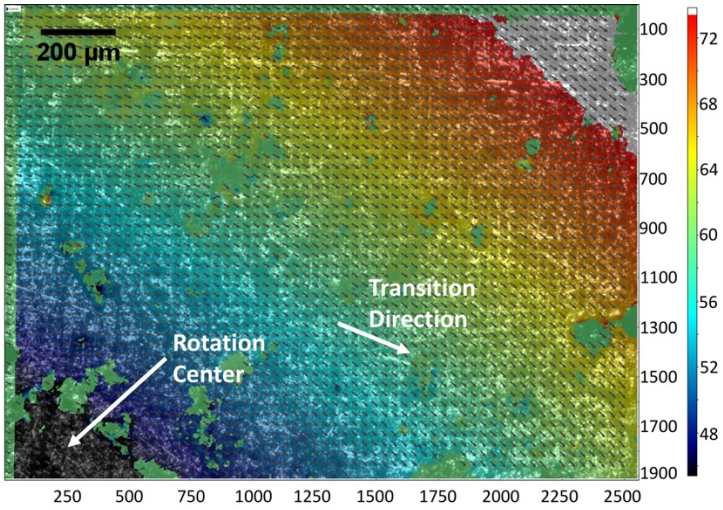



*Figure 40 The displacement map affected by the rotation and transition. The white arrows indicate the rotation center and the direction of transition (all dimensions in pixels)*

### 4.2.2 Pre-pitting test

An example of a coupon sample with 30 salt deposits is shown in Figure 41. SEM images of the surface after 1, 4, 8 and 16 days of corrosion are shown in Figure 42 to Figure 45. From the first day of corrosion, pitting can be found at all 30 salt deposits. In the SEM images of sample after 4-day's corrosion, the corrosion products can be clearly observed near the pitting area. For the sample after 8-day's corrosion, almost all the pitting areas were surrounded by corrosion products. Furthermore, in 12 out of 30 salt deposit locations, it was also observed that the pitting develops from the edge of salt-deposit-covered area to the non-covered area. After 16 days of corrosion, the size of pitting reached 200 µm. X-ray tomography was used to scan the samples after 16 days and 32 days of pitting corrosion, shown in Figure 46. The resolution of the two scans was the same (3.3 µm/pixel), and the size of pitting does not appear to have significant change after the further 16 days of

corrosion. Therefore, for the pre-pitted experiments, the tapered specimens were put into the environmental chamber for 16 days to develop pits before stress corrosion testing.

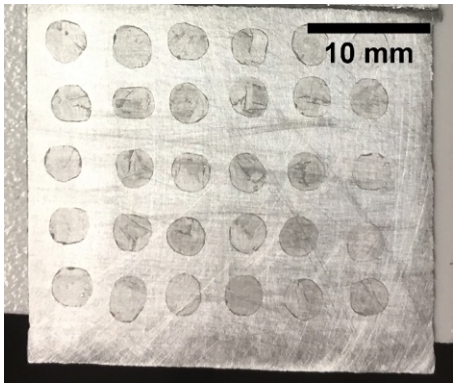



*Figure 41 The square coupon sample for pitting test*

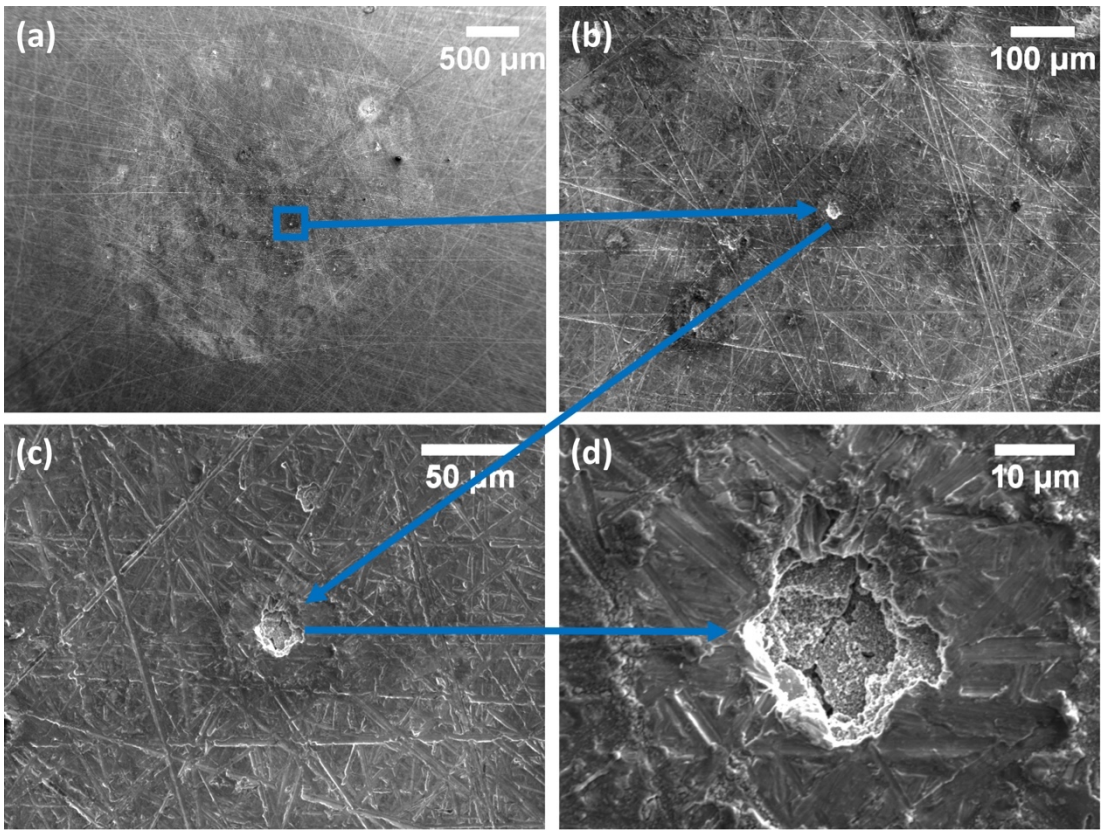



*Figure 42 The SEM images for sample of 1-day's pitting corrosion*

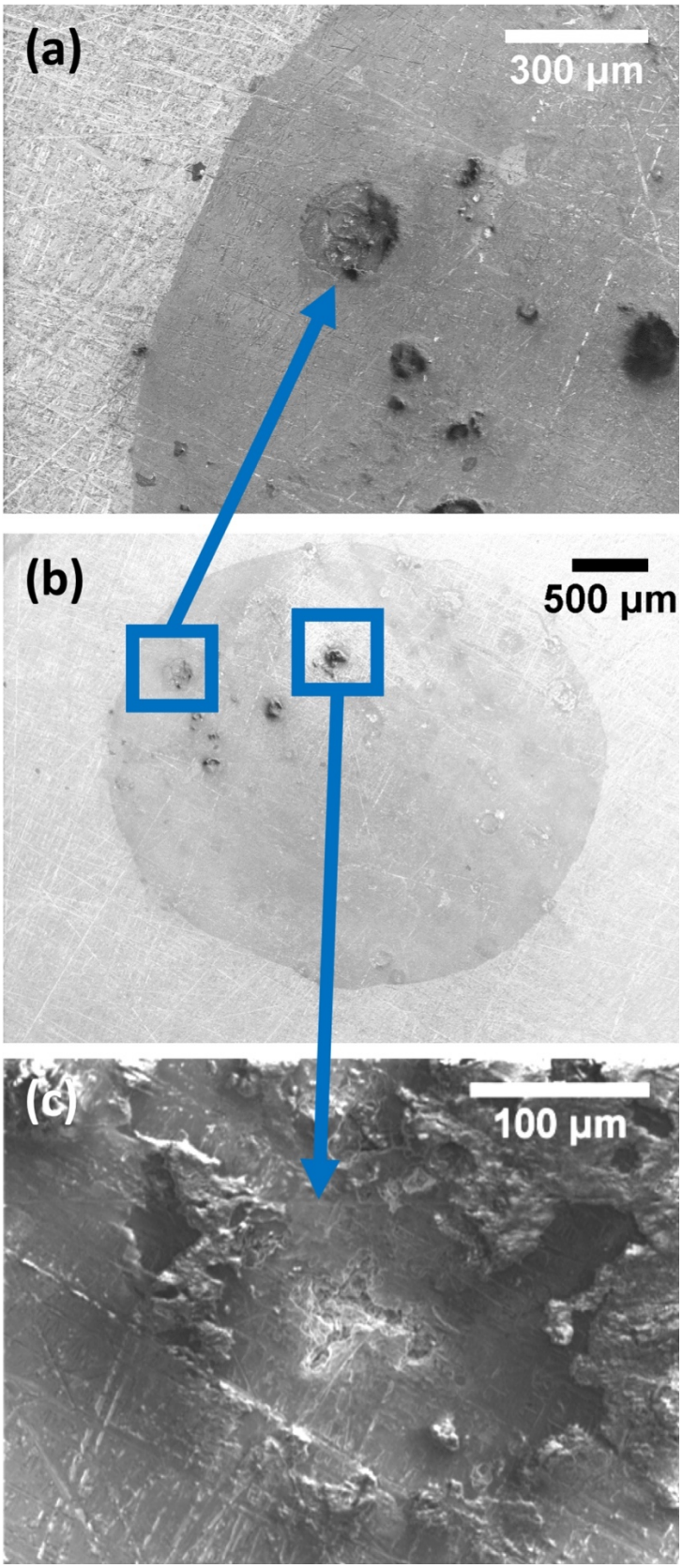



*Figure 43 The SEM images for sample of 4-day's corrosion*

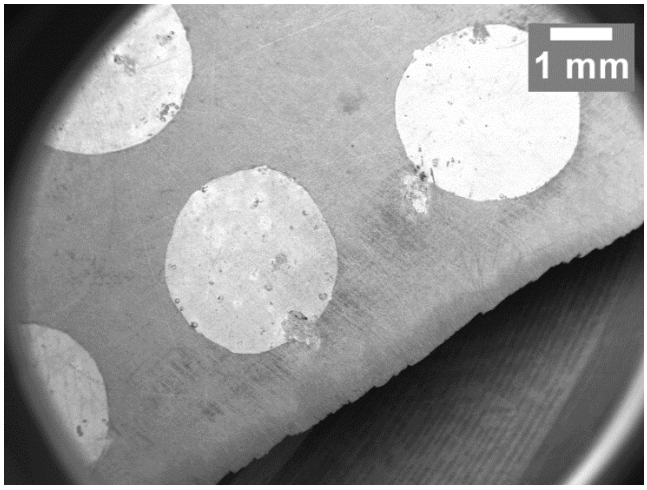



*Figure 44 The SEM images for sample of 8-day's corrosion*

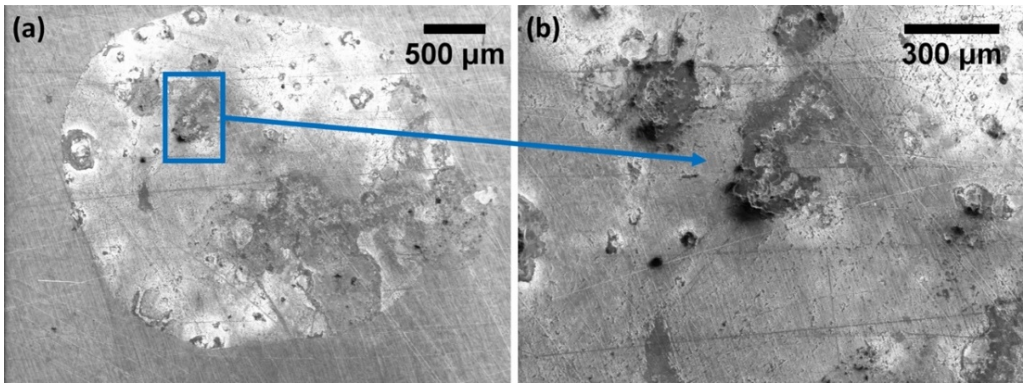



*Figure 45 The SEM images for sample of 16-day's corrosion*

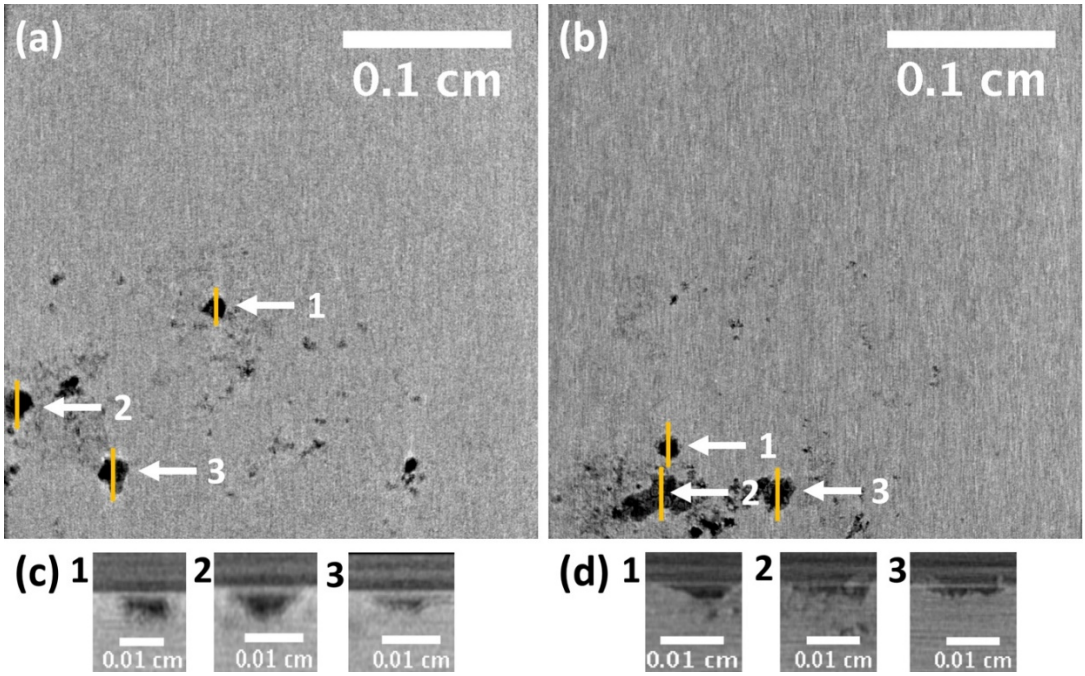



*Figure 46 The Xradia image of a tomography slice for (a) sample after 16-day's pitting corrosion parallel to the surface (b) sample after 32-day's pitting corrosion parallel to the surface (c) sample after 16-day's pitting corrosion perpendicular to the surface (d) sample after 32-day's pitting corrosion perpendicular to the surface*

### 4.2.3 Calibration of the proving ring

The Shimadzu 5 kN loading rig was used to apply five compressive loads of 632 N, 711 N, 790 N, 869 N and 948 N across the diameter of the proving ring, which corresponds to 0.8, 0.9, 1.0, 1.1 and 1.2 times of the tensile yield stress of 6061 T6 aluminum alloy. Maps of the displacement along the x direction (perpendicular to the loading direction) as shown in Figure 47. It can be observed that the displacement of the left edge is around 0 while that of the right edge is positive, which indicates the expansion of the proving ring along the x direction. With the increase of the applied load, the difference between the right and left edge increases. Two areas at the size of 6 mm x 3 mm at the left and right side were selected (A and A' as shown in Figure

47, 790N). The difference between the average value of displacement x between these two areas was calculated as the horizontal diametral expansion, and the sum of the standard deviation of them was used as a conservative estimate of the error, represented in Table 4.

Figure 48 shows the displacement map along the y and z directions of the proving ring under a load of 790 N. The displacement y of the top edge is negative, while that of the bottom edge is around 0, indicating compression along the y direction, which is the direction of the applied compressive load. Similarly, two areas at the size of 6 mm x 3 mm at the top and bottom edge were selected (B and B'). The difference between the average displacement of them is shown in

Table 5. The displacement z of the whole proving ring is around 0±0.004, which means there was no out of plane movement during the compression test.

Figure 49 shows that the horizontally diametral change has a positive linear relationship with the load, whereas the vertically diametral change has a negative linear relationship. The gradient of the horizontal diametral change is 0.225±0.005μm/N, while that of the vertical diametral change is 0.267±0.002 μm/N. For the later SCC test of the 6061 T6 aluminum based composite, a load of 1050 N need to be applied to it. Therefore, a repeated calibration of the horizontally diametral change of the proving ring was conducted again from 50 N to 1100 N, with the increment of 50 N. The horizontally diametral change-load curve for two tests overlaps with each other, verifying the result of the calibration.

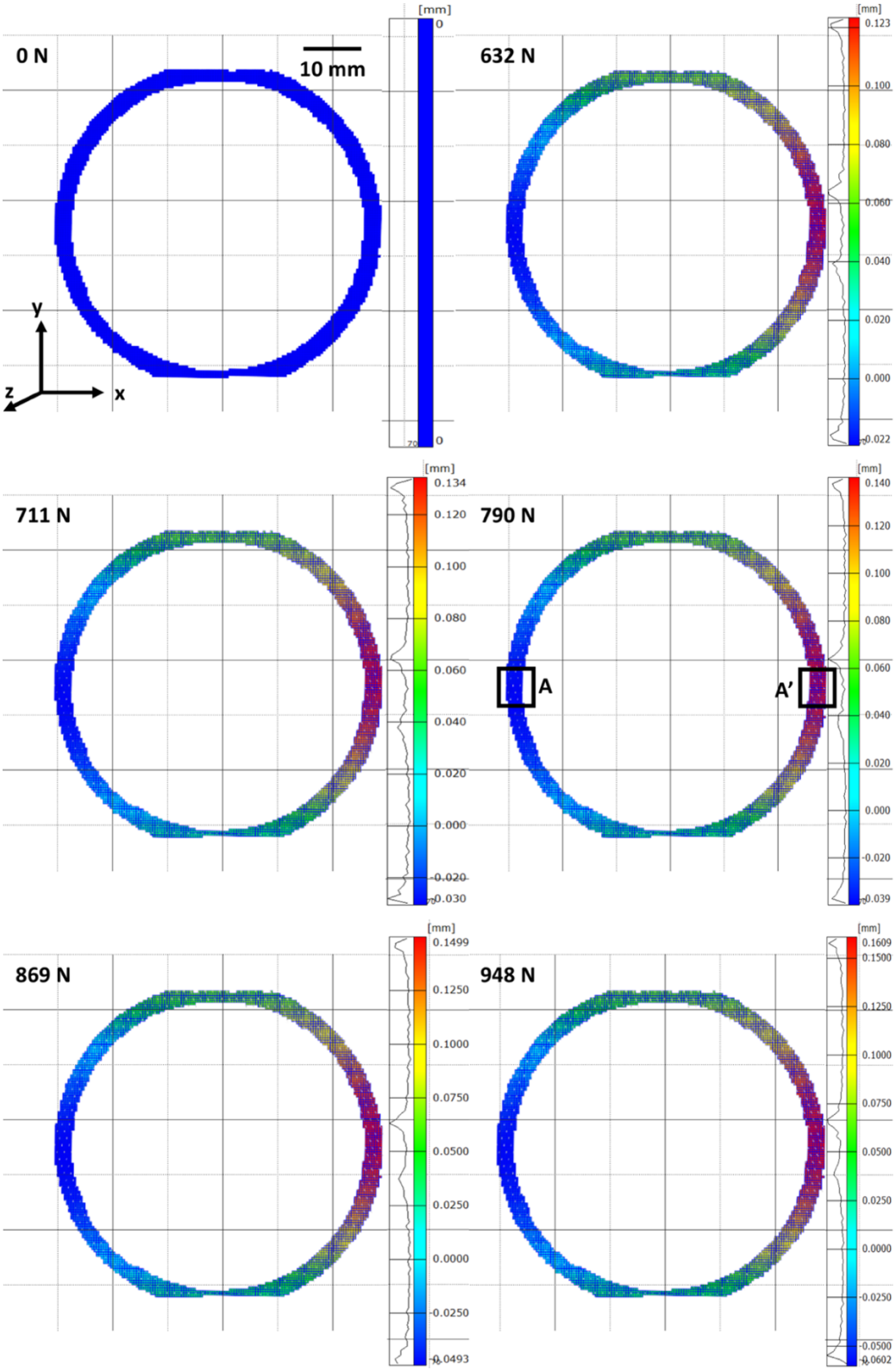



*Figure 47 The map of displacement along x direction of the proving ring under different loads. The load was applied along y direction*

*Table 4 Horizontally diametral change*

| Loads / N | A / mm | A' / mm | Horizontally Diametral Change / mm |
|---|---|---|---|
| 632 | -0.019±0.002 | 0.121±0.001 | 0.140±0.003 |
| 711 | -0.027±0.002 | 0.131±0.002 | 0.158±0.004 |
| 790 | -0.036±0.002 | 0.138±0.001 | 0.174±0.003 |
| 869 | -0.046±0.002 | 0.146±0.002 | 0.192±0.004 |
| 948 | -0.054±0.002 | 0.158±0.002 | 0.212±0.004 |

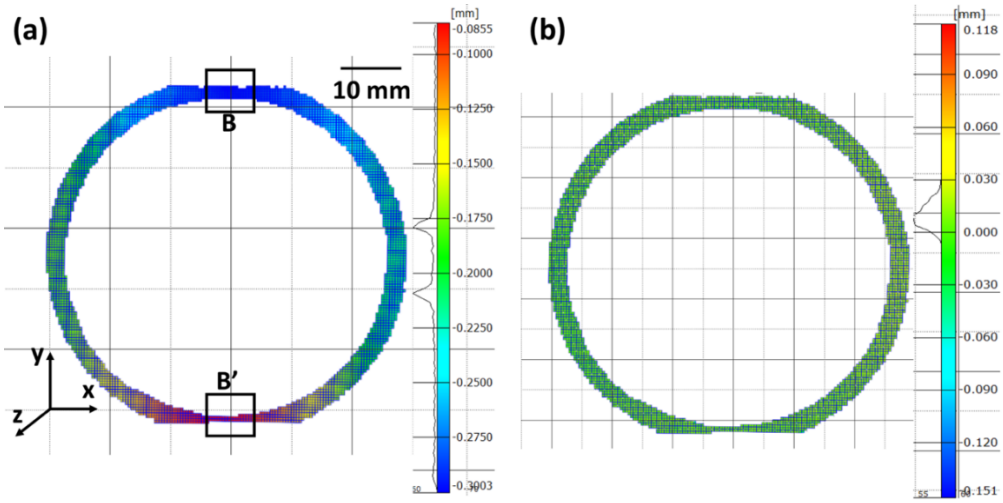



*Figure 48 The map of displacement along (a) y direction and (b) z direction under 790 N*

*Table 5 Vertically diametral change*

| Loads / N | B / mm | B' / mm | Vertically Diametral Change / mm |
|---|---|---|---|
| 632 | -0.240±0.002 | -0.077±0.002 | -0.163±0.004 |
| 711 | -0.267±0.002 | -0.084±0.002 | -0.183±0.004 |
| 790 | -0.294±0.002 | -0.089±0.002 | -0.205±0.004 |
| 869 | -0.322±0.002 | -0.096±0.002 | -0.226±0.004 |
| 948 | -0.348±0.002 | -0.101±0.002 | -0.247±0.004 |

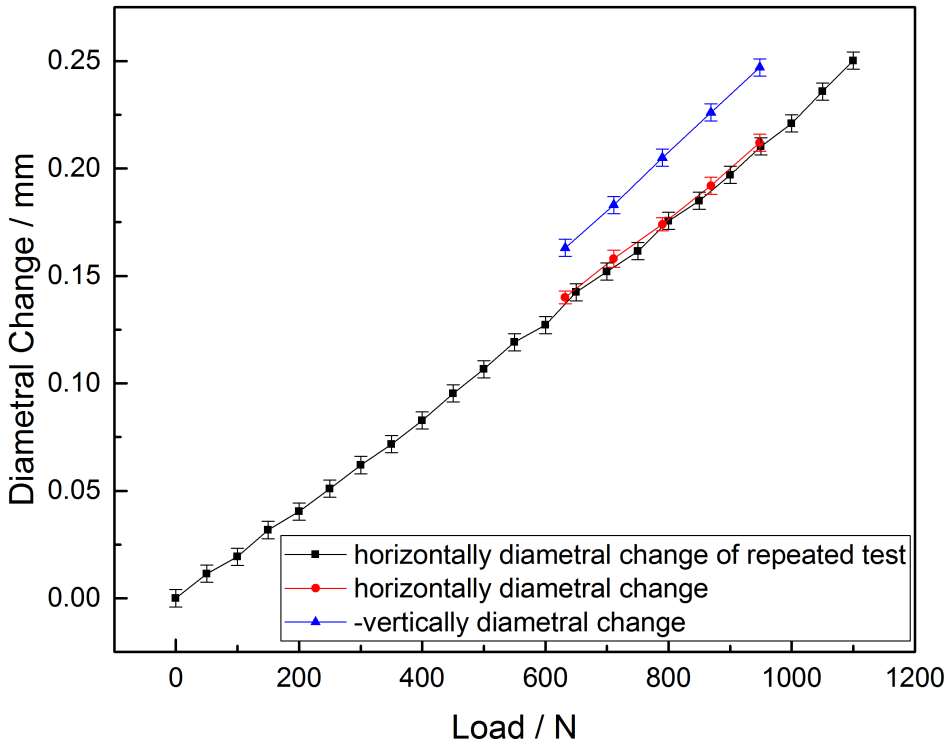



*Figure 49 The change of horizontal diameter and inverse change of vertical diameter along with the increase of load*

## 4.3 Stress corrosion cracking behavior

Stress corrosion cracking testing was conducted on one non pre-pitted tapered sample and three pre-pitted samples. A load of 948±20 N was applied to each using the proving ring and with three $MgCl_2$ salt deposits applied to each sample. The load error is calculated from the uncertainty in the diameter change of 0.004 mm and the calibration gradient.

Figure 50 shows an example of a pre-pitted sample before and after 16 days of testing. The 3 x 3 images have been manually stitched (using PowerPoint). It can be seen that the main features on the surface do not change, and only some areas are corroded as the arrows point to in the figure (the same color arrows point to the same region before and after corrosion). Therefore, DIC could be applied to calculate the displacements and the strain changes during the corrosion process.

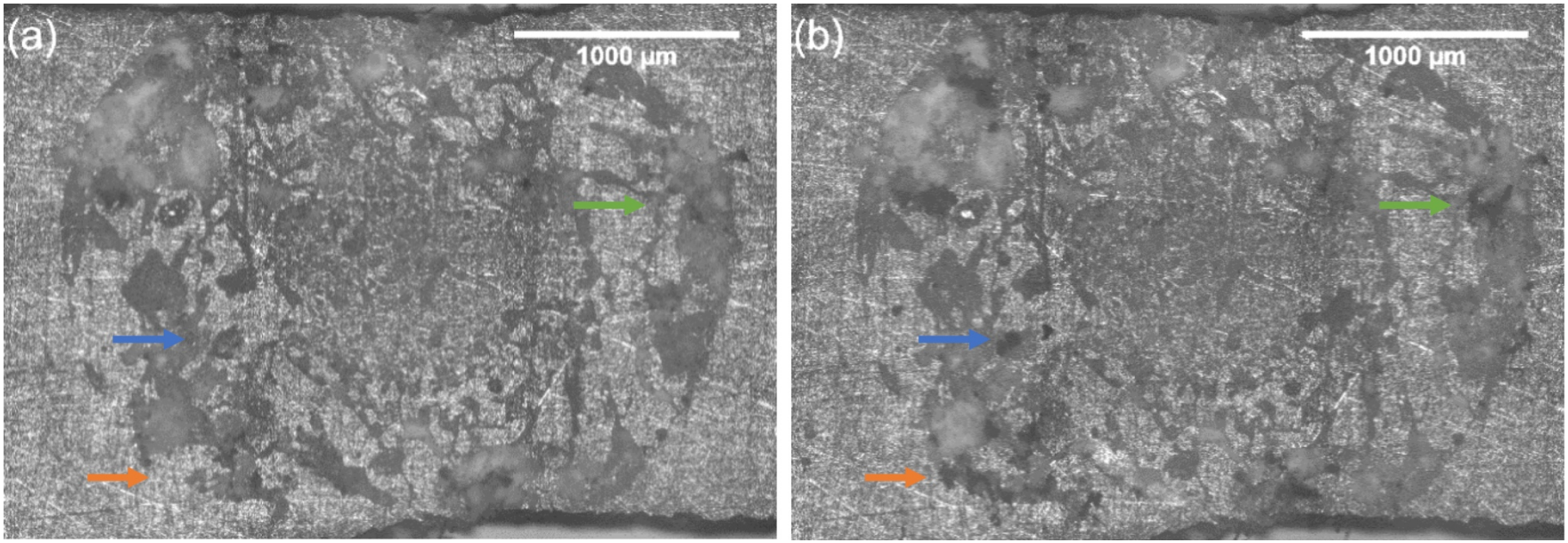



*Figure 50 The stitched optical image of #3 pre-pitted specimen (a) before stress corrosion cracking test and (b) after 16 days of the stress corrosion cracking test*

### 4.3.1 SEM

SEM was used to observe the surface of four specimens after stress corrosion cracking (details in section 3.5.5). Images for the center locations are presented in Figure 51 to Figure 54. The edge of salt deposit is clear on the images of pre-pitted samples, while it is blurred on the image of the non pre-pitted sample since the corrosion develops outwards from the salt deposit area. Cracks can be observed in the pre-pitted samples, and they are perpendicular to the direction of the load. In addition, cracks are concentrated near the edge of salt deposit (the edge of sample). The cracks in #2 and #3 pre-pitted samples develop from the pitting, while those in #1 pre-pitted sample are not. Figure 55 shows an SEM image for the end location of #3 pre-pitted sample, and similarly, only pitting can be found on its surface.

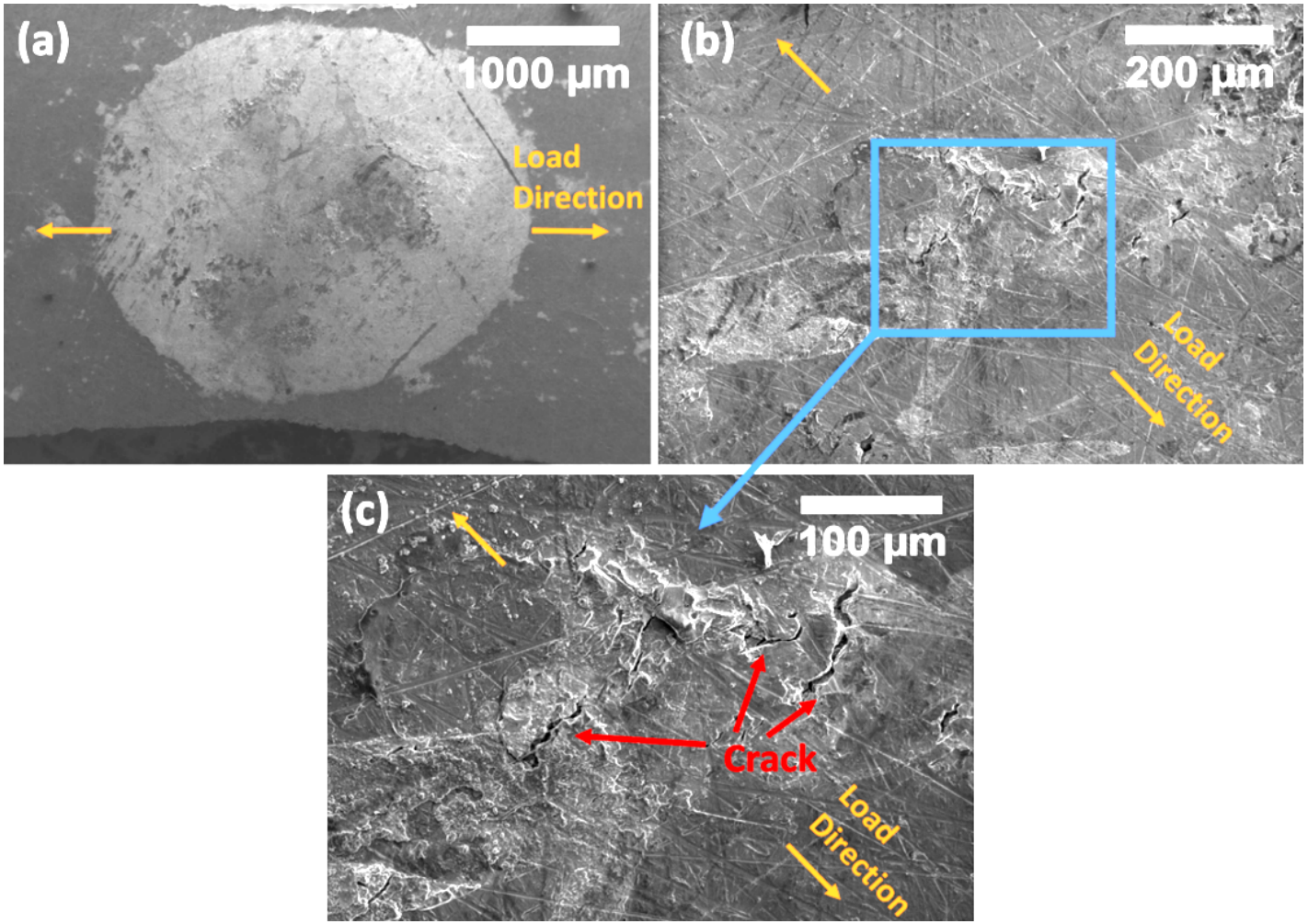



*Figure 51 SEM images for the center location of #1 pre-pitted sample*

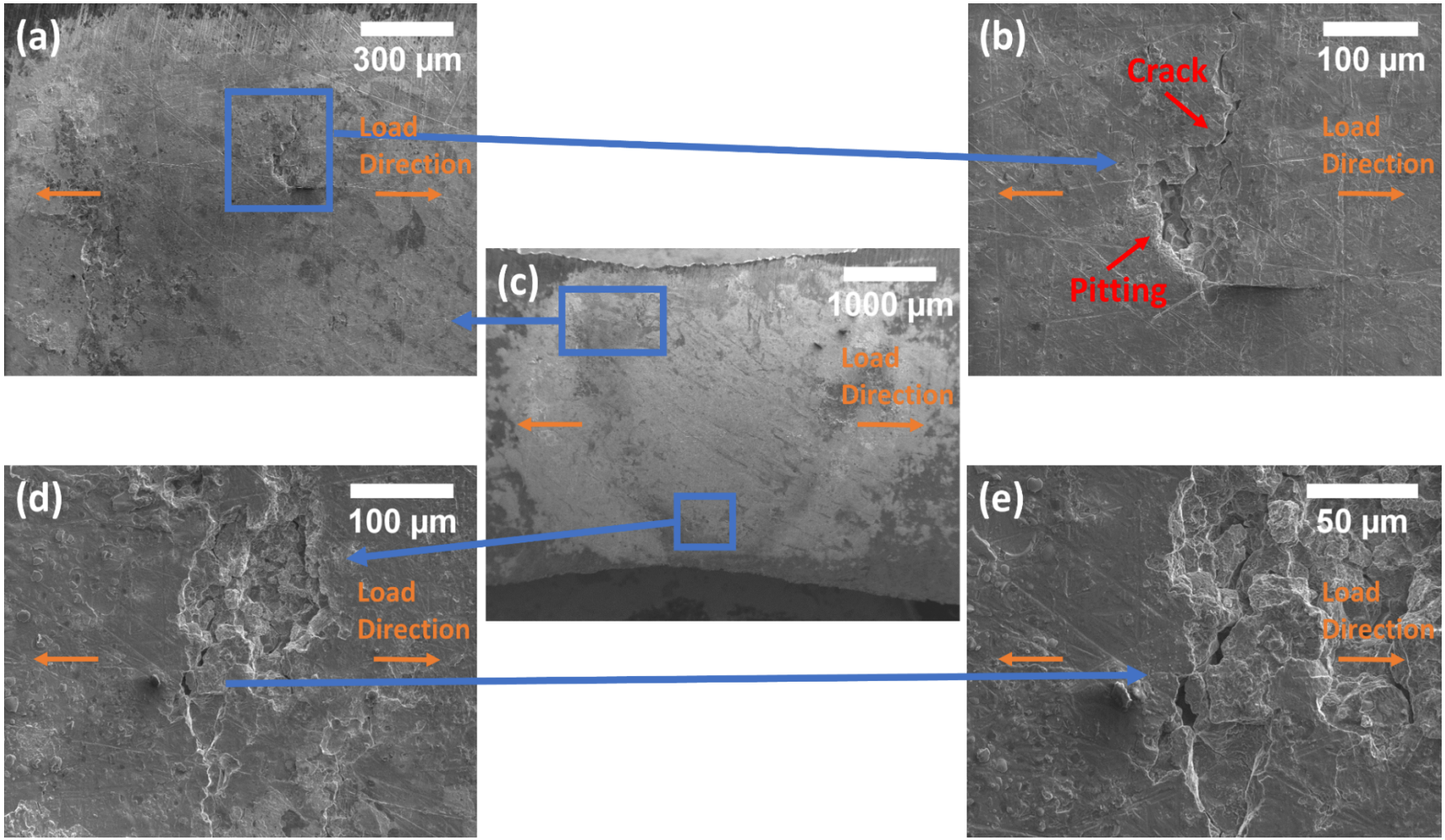



*Figure 52 SEM images for the center location of #2 pre-pitted sample*

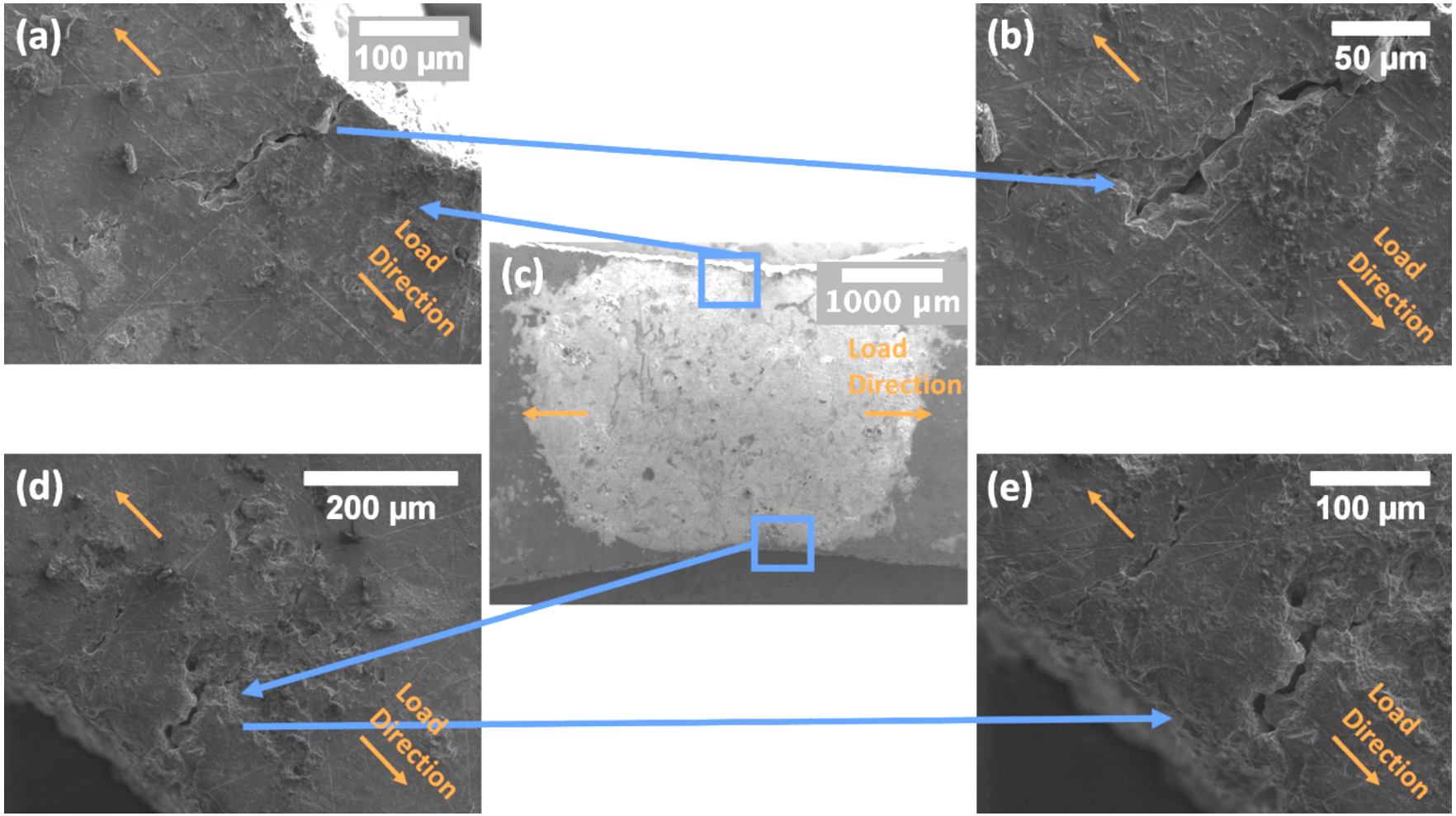



*Figure 53 SEM images for the center location of #3 pre-pitted sample*

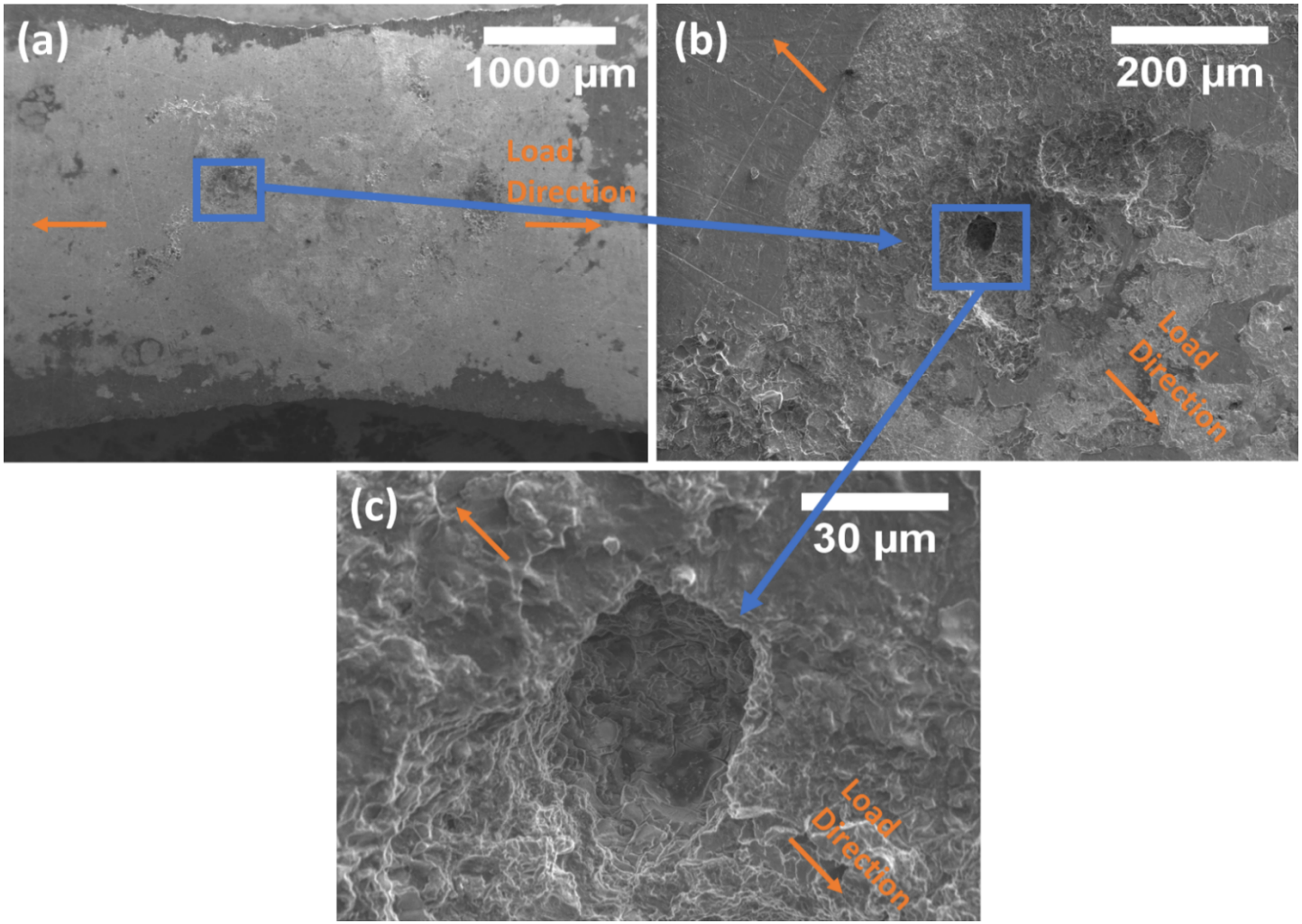



*Figure 54 SEM images for the center location of the non- pre-pitted sample*

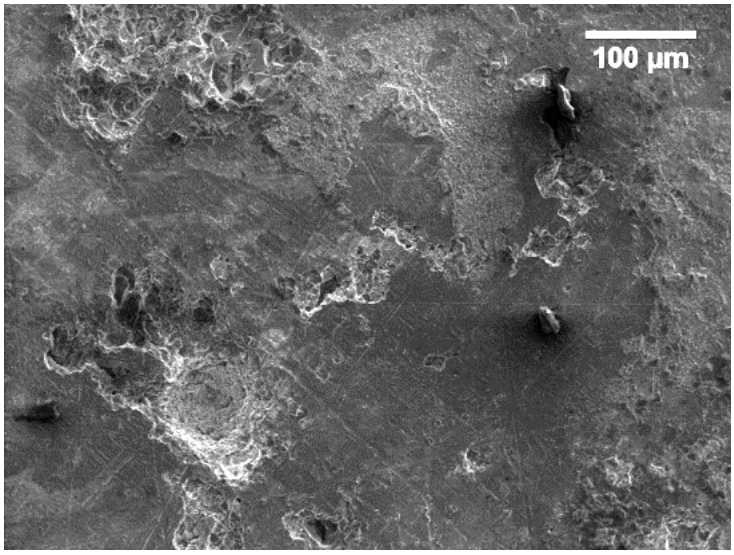



*Figure 55 The SEM image for the end location of #3 pre-pitted sample*

### 4.3.2 DIC

#### 4.3.2.1 Pre-processing

An example optical image from one of the 9 images recorded at each droplet is shown in Figure 56. The raw displacement map, obtained by correlating this with the same location after 16 days, is shown in Figure 57. The displacement vectors show there is clearly a rigid body movement, which needs to be removed. This was done, using the method described in section 3.5.2. The effect of the correction is shown in Figure 58, where Figure 58 (a) show the total displacement before correction and Figure 58 (b) shows the displacements after correction to remove the rigid body translations and rotations. It can be seen that in the middle of the image, the relative displacement now has the minimum value, and it increases evenly in the direction of applied stress (x) from the middle to the two edges. There is no significant change in displacement perpendicular to the applied load.

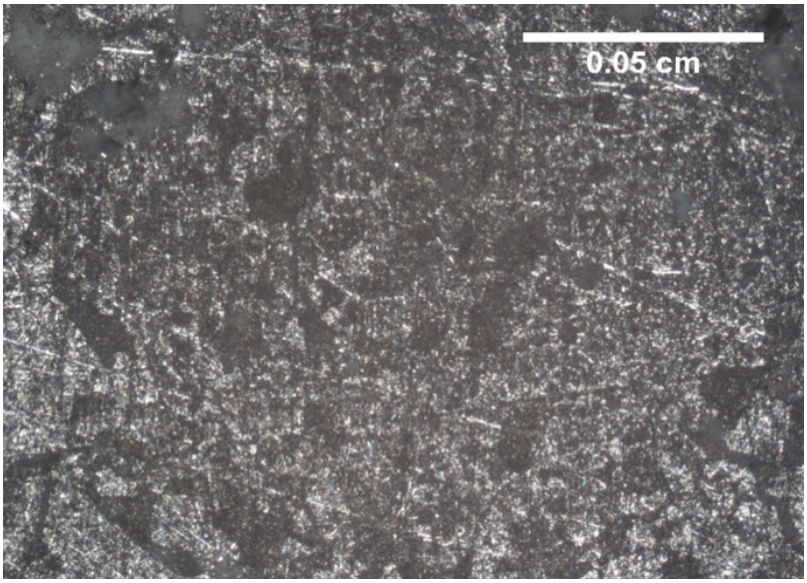



*Figure 56 One of the reference images of the center location of #3 pre-pitted sample*

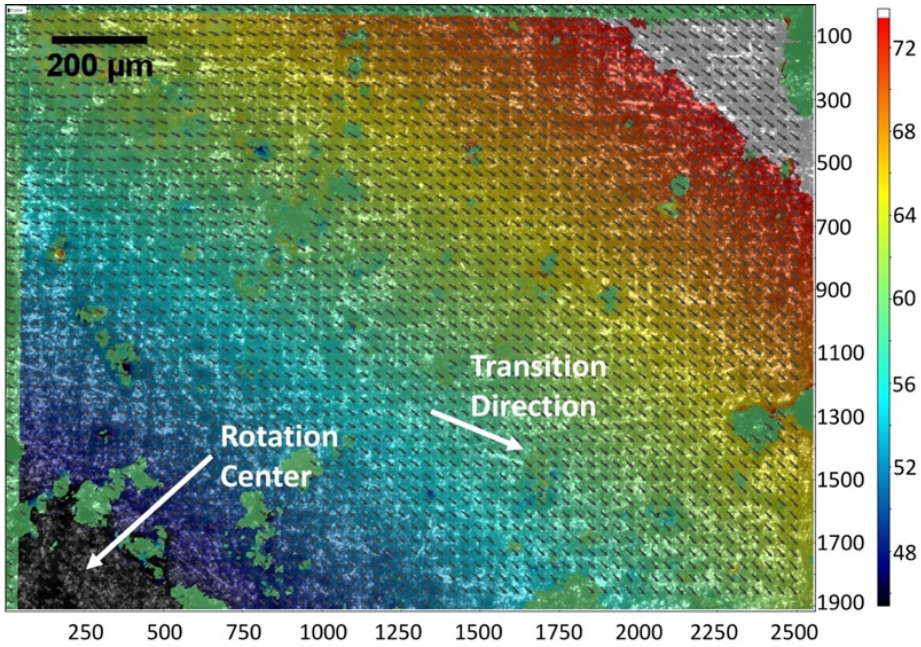



*Figure 57 The displacement map affected by the rotation and transition. The white arrows indicate the rotation center and the direction of transition (all dimensions in pixels)*

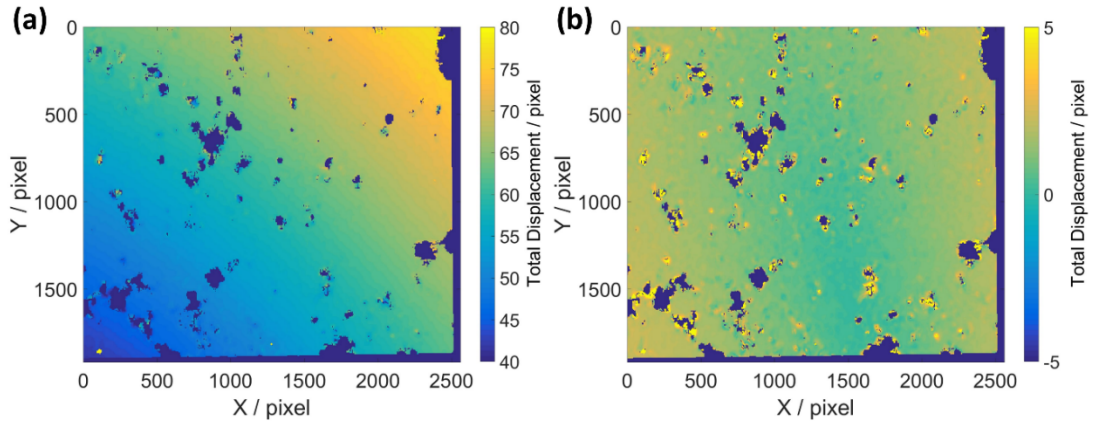



*Figure 58 The total displacement map of one part of the center location of #3 pre-pitted sample (a) before processed and (b) after processed (the pixel size is 0.65 μm/pixel)*

#### 4.3.2.2 Image stitching

Figure 59 shows the stitched displacement x maps from the center droplet of the four different specimens (#1 to #3 pre-pitted and #4 is non-pre-pitted), after 9 days of the stress corrosion cracking test. The dark blue areas are the areas that cannot be correlated caused by the existence of salt deposits and corrosion products. For the non pre-pitted sample, the dark blue area is much larger than that of the pre-pitted sample. The displacement x maps of the two end locations of #3 pre-pitted sample after 16 days are shown in Figure 60. Compared with the center location, the difference between the left and right edge of the displacement x map of the end location is visibly smaller, and the change is not obvious after 16 days of stress corrosion.

Figure 61 shows the displacement x map change for the center salt deposit location of #3 pre-pitted sample over 16 days (d1 to d16). Along with the increase of the corrosion time, the number of dark blue area increases, as does the difference

between the right and left edge of the map. Maps that show the change in displacement y of #3 pre-pitted sample over 16-day's is shown in Figure 62.

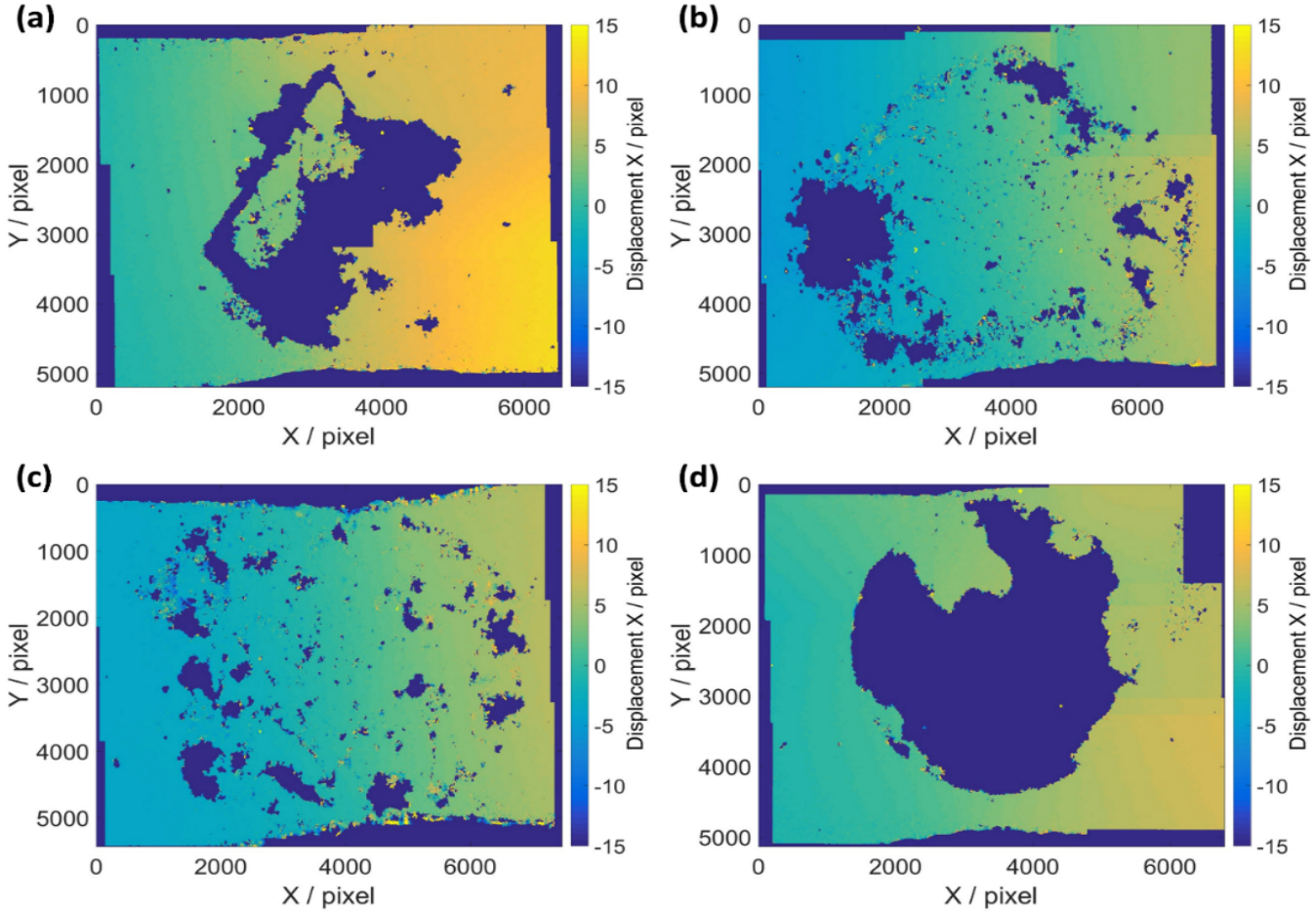



*Figure 59 Stitched displacement maps of the center location of (a) #1 pre-pitted sample (b) #2 pre-pitted sample (c) #3 pre-pitted sample and (d) #4 non pre-pitted sample after 9-days of the stress corrosion cracking test (the pixel size is 0.65 μm/pixel)*

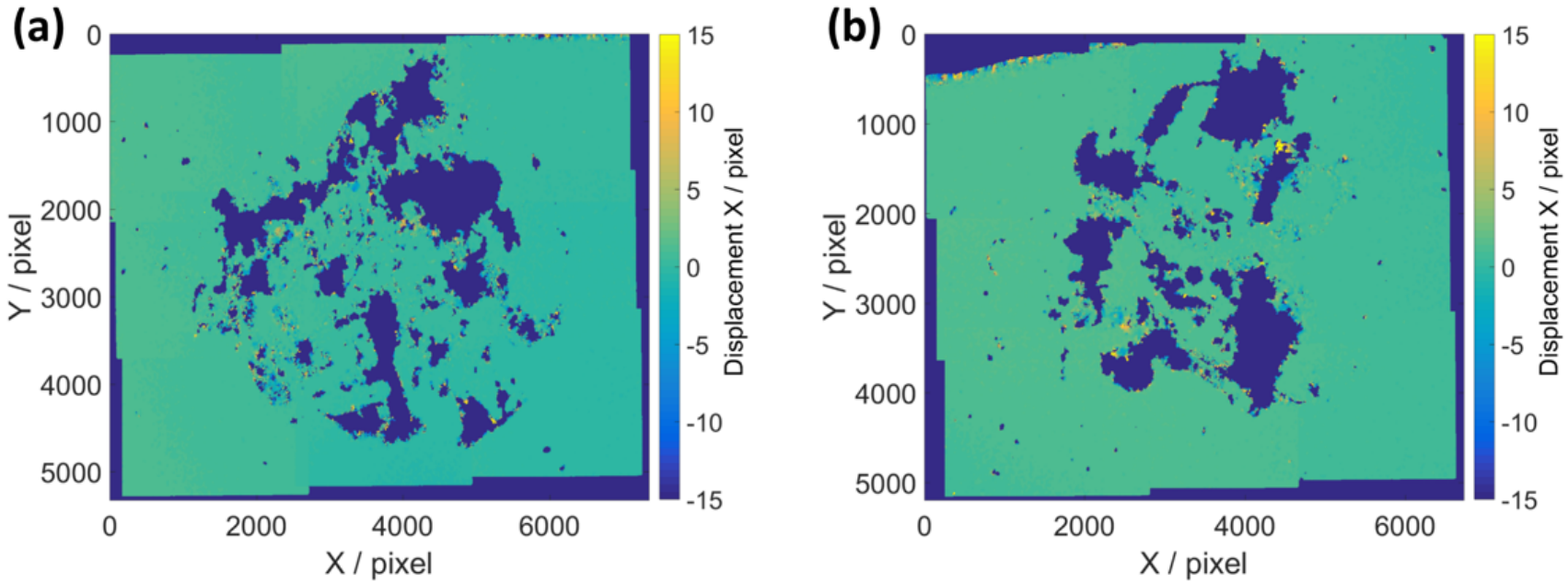



*Figure 60 The stitched displacement x map of (a) the right location of #3 pre-pitted sample and (b) the left location of #3 pre-pitted sample after 16-day SCC test (the pixel size is 0.65 μm/pixel)*

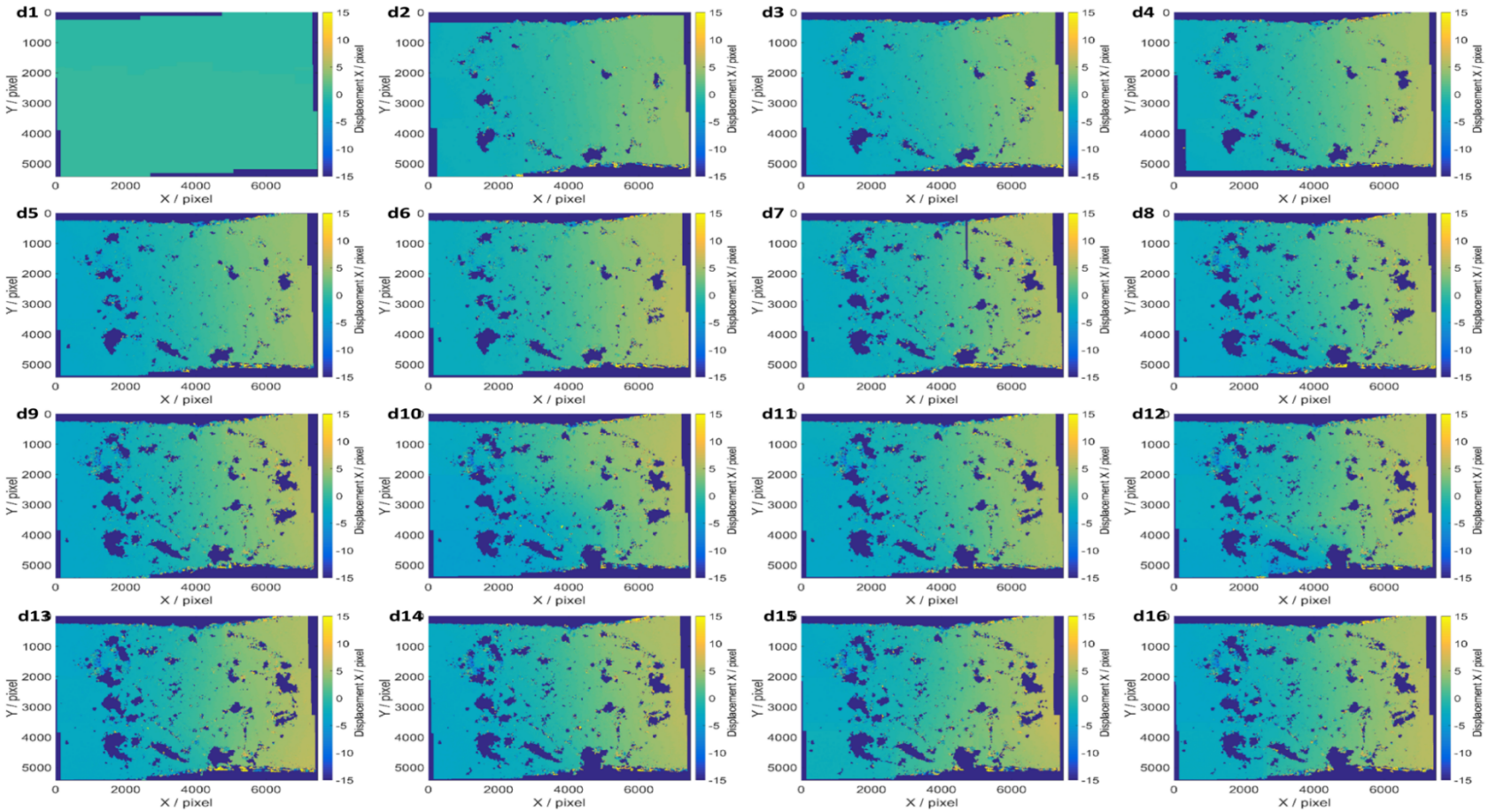



*Figure 61 The change of the displacement x map of #3 pre-pitted sample in the center location over 16-days (d1 to d16) of the stress corrosion cracking test (the pixel size is 0.65 μm/pixel)*

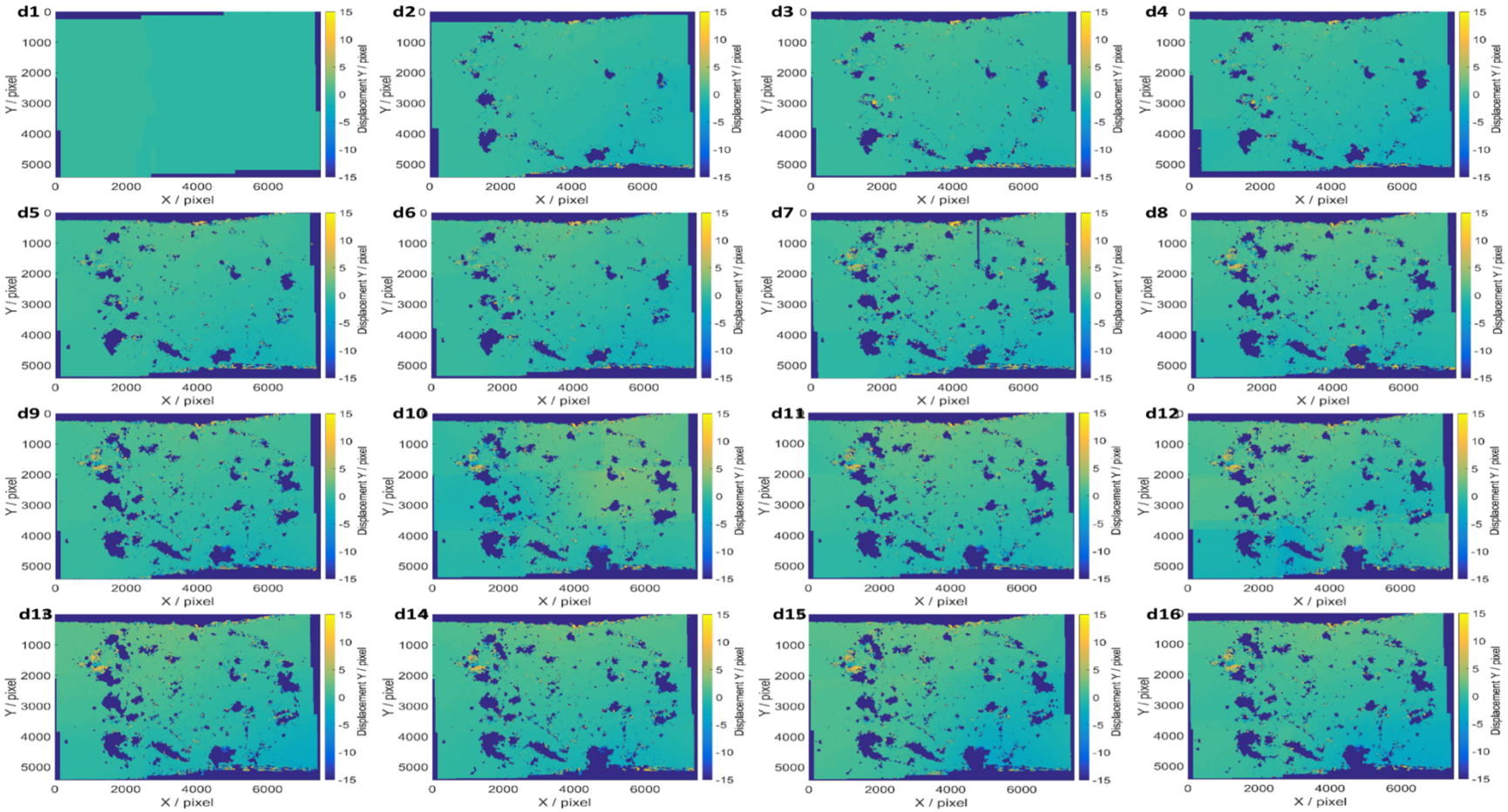



*Figure 62 The change of the displacement y map of #3 pre-pitted sample in center location for 16-day's stress corrosion cracking test (the pixel size is 0.65 μm/pixel)*

#### 4.3.2.3 Analysis

In order to quantitatively compare the displacement maps in detail, the strain change over the salt deposit during the stress corrosion process is calculated, as described in section 3.5.4. A horizontal band with the width of 40 pixels in the middle of the stitched data was selected to calculate the specimen's extension along the load direction (from A1 to A2 in Figure 63). With the step size of 5 pixels, the width of 40 pixels contains 8 points in the displacement map. By calculating the average value of 8 points (NaN value excluded), the displacement x vs. x coordinate curve along this band is obtained, and the gradient of this curve is the strain (this curve is shown in Figure 64, 'Unsmoothed curve'). Similarly, a vertical band with the width of 40 pixels was selected to calculate the specimen's strain perpendicular to the load direction (from B1 to B2 in Figure 63)

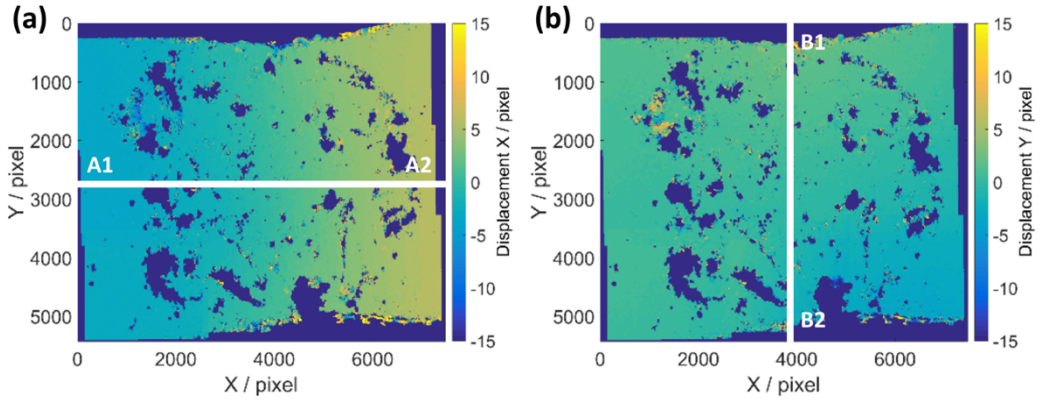



*Figure 63 The schematic diagram of the data selected to calculate the strain change along the (a) x direction (A1A2) and (b) y direction (B1B2)*

In order to remove the background noise, seven different filters were tested on the data of #3 pre-pitted sample to smooth the same curve. The filter was applied through Matlab, calculating the value of elements by moving average, and the span size refers to the size of the neighboring elements selected to calculate. The result is

shown in Figure 64, and it can be observed that further filtering with ‘loess’, ‘lowess’, ‘remove average’ and ‘sgolay’ can reduce the noise, but the noise still exists. The ‘median’ filter makes the curve lose many points. The curve treated by ‘rloess’ is not as smooth as that treated by ‘rlowess’, and the shape of curve is changed at the tail. Therefore, the filter ‘rlowess’ gives the best result, and it was chosen to process the data. If one compares the data after smoothing with each of the seven different filters with the unsmoothed data, it can be observed that none of filters change the gradient of the curve (Figure 65).

Figure 66 shows the data smoothed with ‘rlowess’ filter using different span size. As the span increases from 5 to 150, the curve becomes smoother. However, increasing from 150 to 200 does not visibly improve the performance of filter. Therefore, 150 was chosen as the span size. The gradient of each point at the smoothed curve was calculated by Matlab to obtain a gradient-x coordinate curve. This result was also smoothed with ‘rlowess’ filter and 150 span size, as shown in Figure 67 (a).

The gradient is around zero in the area outside of the salt deposit. It gradually increases then reaches a plateau in the middle of the deposit. 400 points on the displacement map with maximum values are selected, and this range corresponds to a length of 1.3 mm (2000 pixels) in the middle of the 3 mm salt deposit location. The average value of these 400 central values was calculated and represents the strain over the salt deposit location, and the standard deviation is the uncertainty in the strain. The same approach was used to analyze the strain in the y-direction, perpendicular to the applied load.

Figure 68 shows the x-strain of the center salt deposit location for the four specimens as a function of time. It can be observed that for both non pre-pitted sample and pre-pitted samples, the strain increases significantly at the beginning of the stress

corrosion test, and then remains stable. However, the strain of the non pre-pitted sample is smaller than that of the pre-pitted sample after the same corrosion time. The strain of non pre-pitted sample increases over a longer time.

The comparison of the strain along the x direction of the center and end salt locations for pre-pitted sample #3 is shown in Figure 69. The strain $\varepsilon_x$ of the center location increases with the corrosion time, while that of the end locations fluctuates around zero. Figure 70 shows the strain along the y direction at these locations. The strain $\varepsilon_y$ decreases with time, but their magnitude it is much smaller than that of the strain $\varepsilon_x$. Of the three locations, the center location has the largest strain $\varepsilon_y$ decrease.

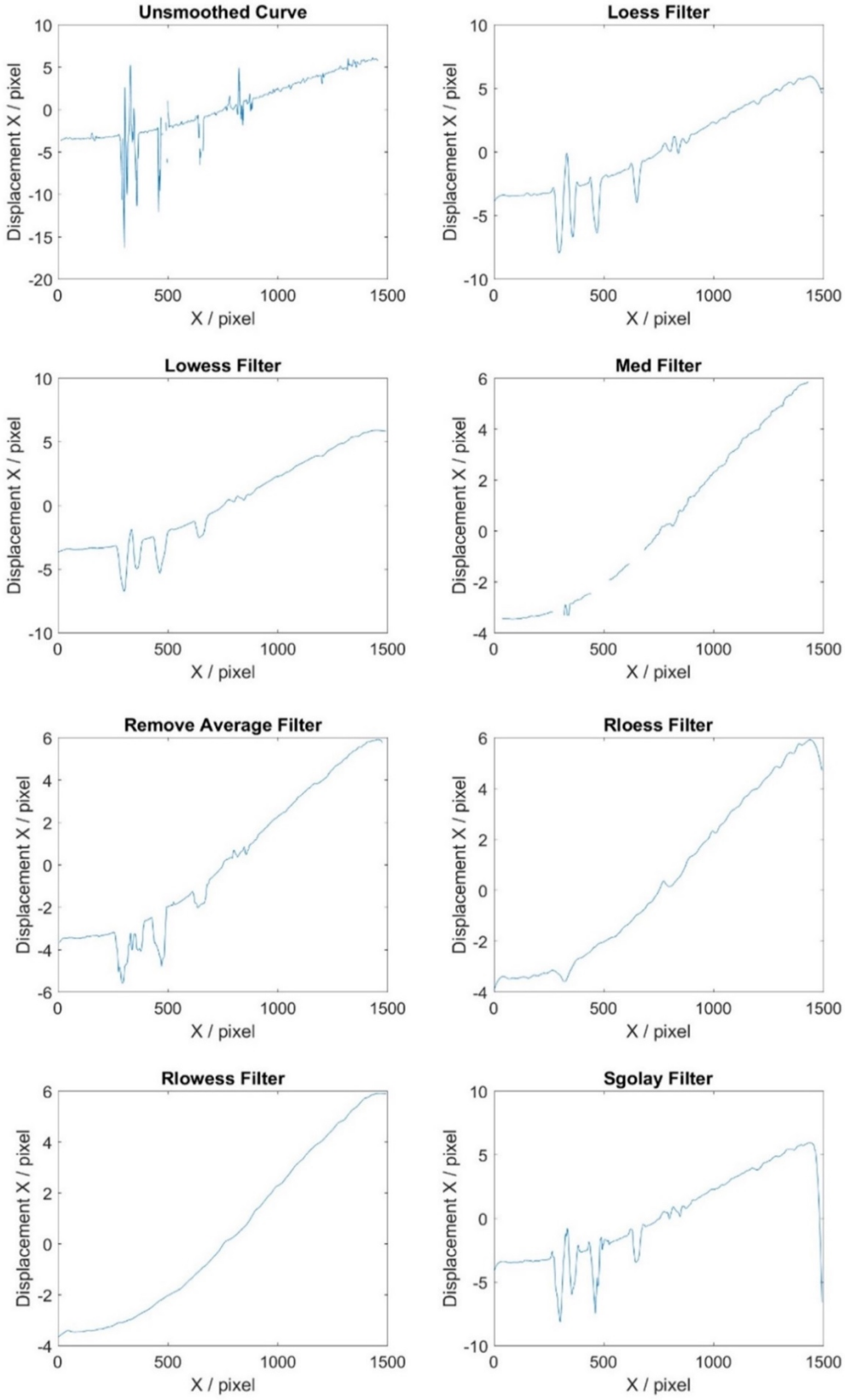



*Figure 64 Curves smoothed with different filters*

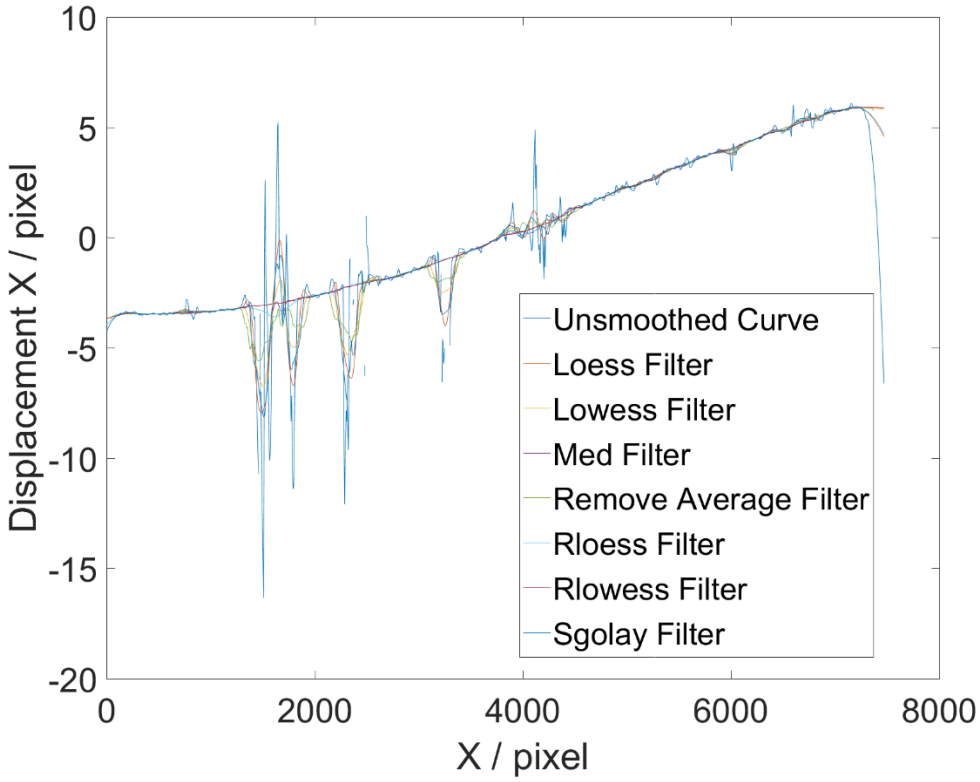



*Figure 65 The filters do not change the gradient of the curve*

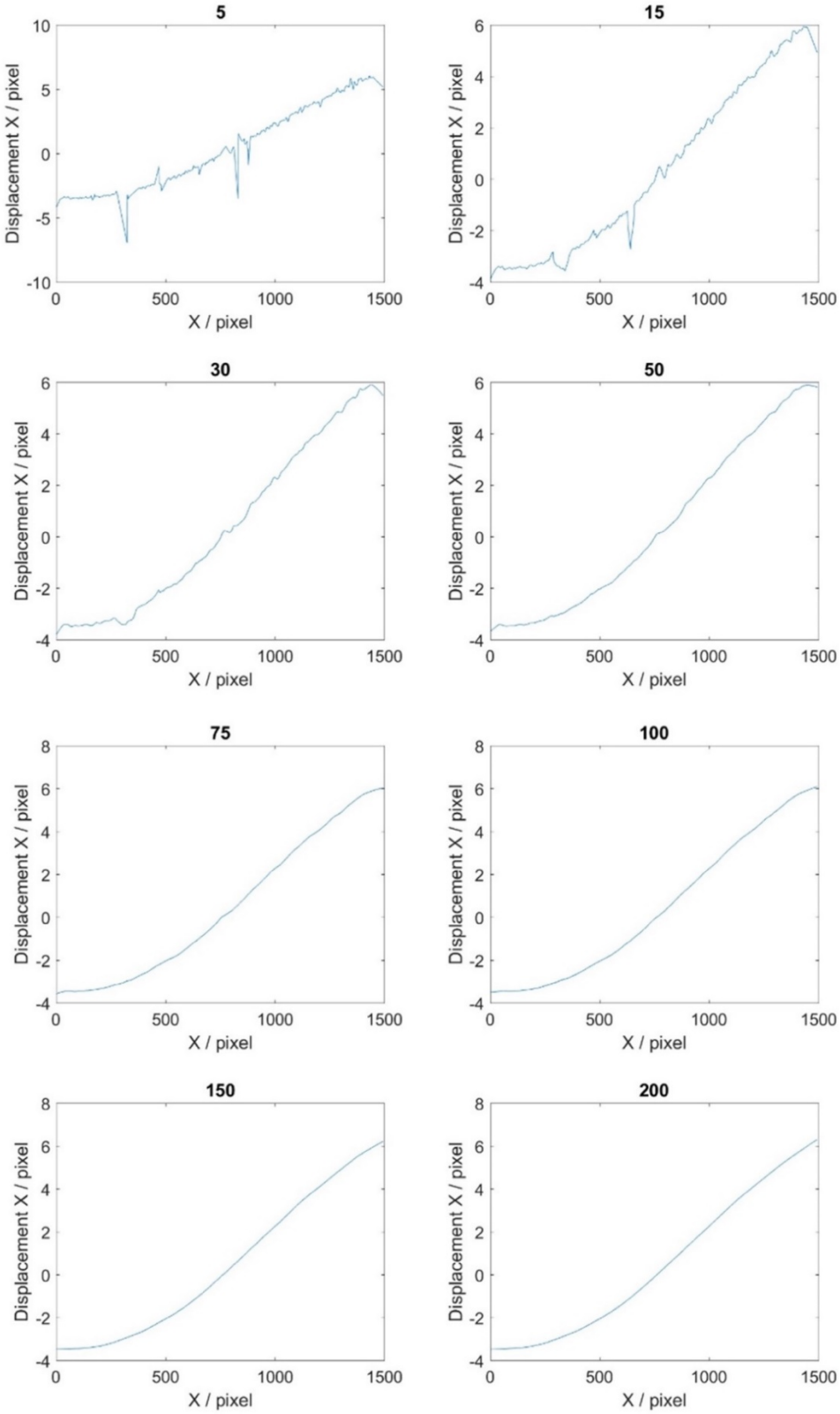



*Figure 66 Curves smoothed with 'rlowess' filter but different span sizes*

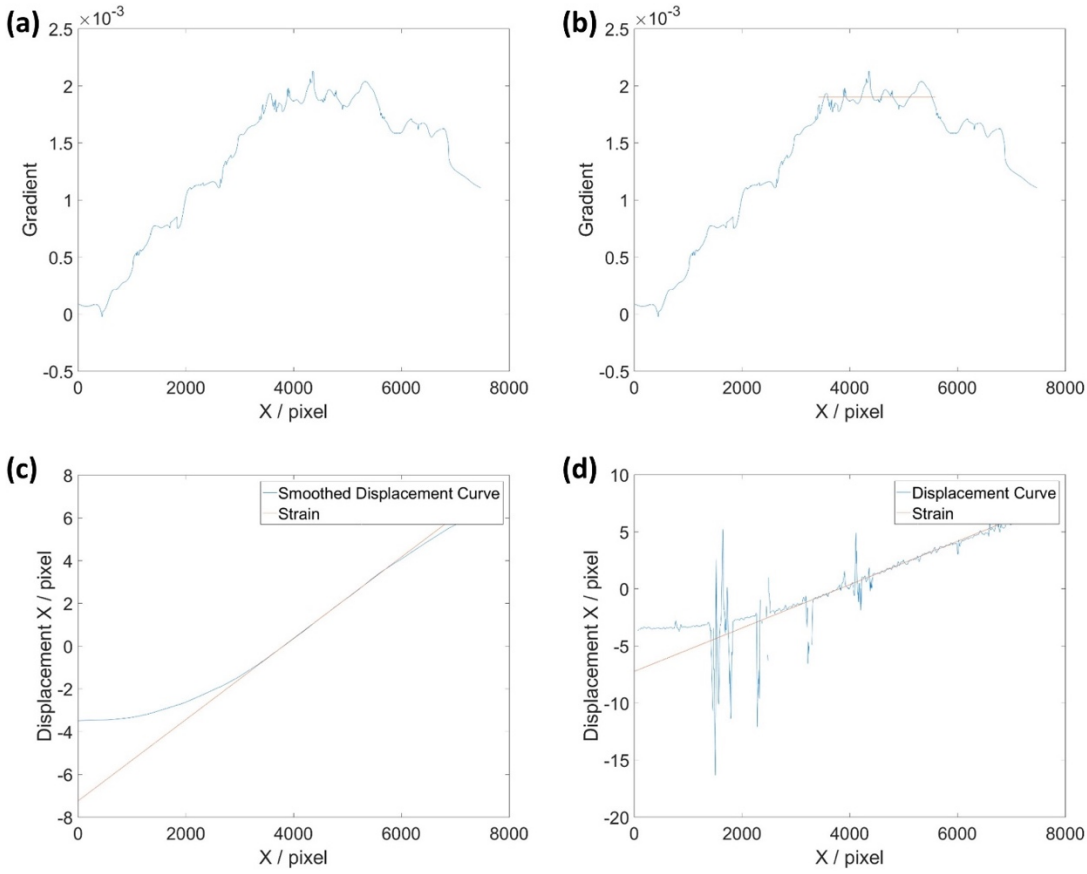



*Figure 67 (a) The gradient of each point on the smoothed displacement x curve (b) the range of 400 central values and the average value of them (c) the smoothed displacement x curve with a line of the calculated gradient (d) the original displacement x curve with a line of the calculated gradient*

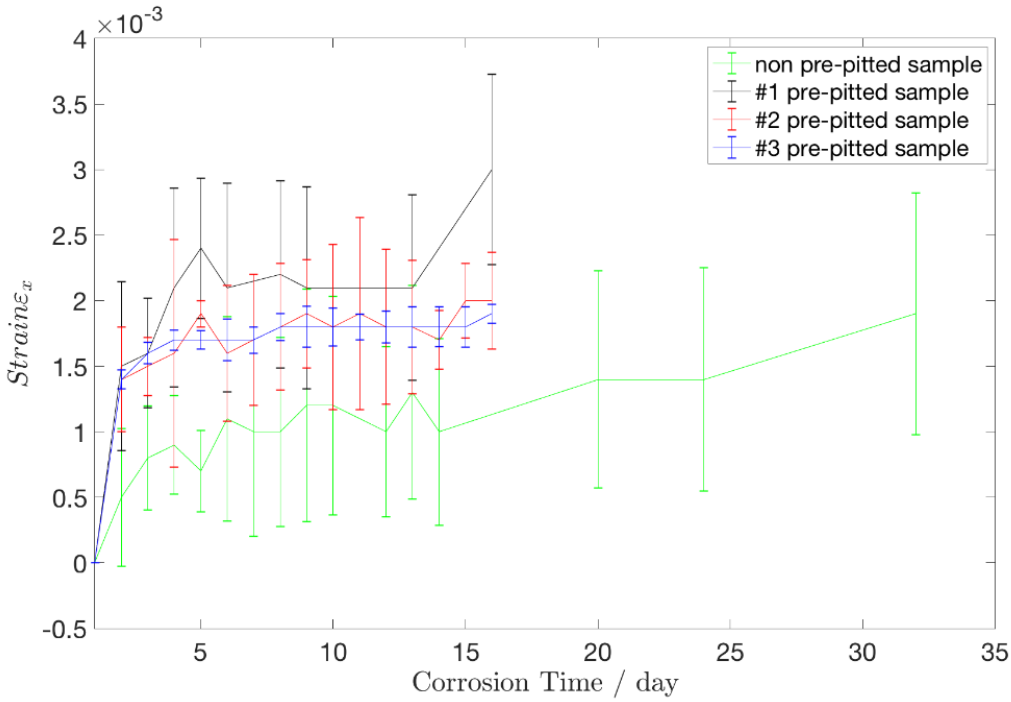



*Figure 68 Strain $\varepsilon_x$ -corrosion time curve for the center location of four specimens*

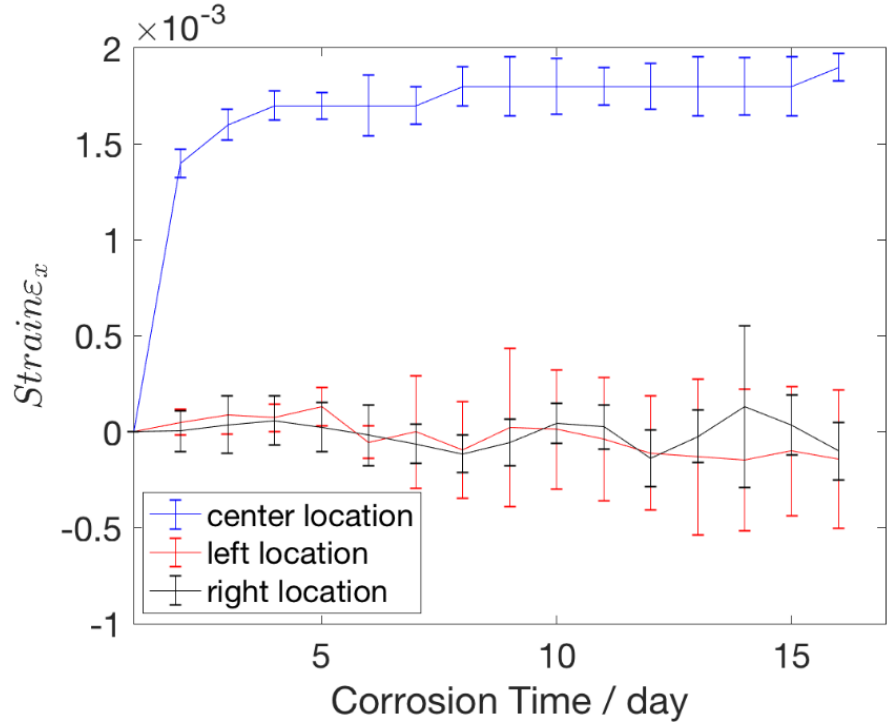



*Figure 69 Strain $\varepsilon_x$ -corrosion time curve for different salt locations of #3 pre-pitted sample*

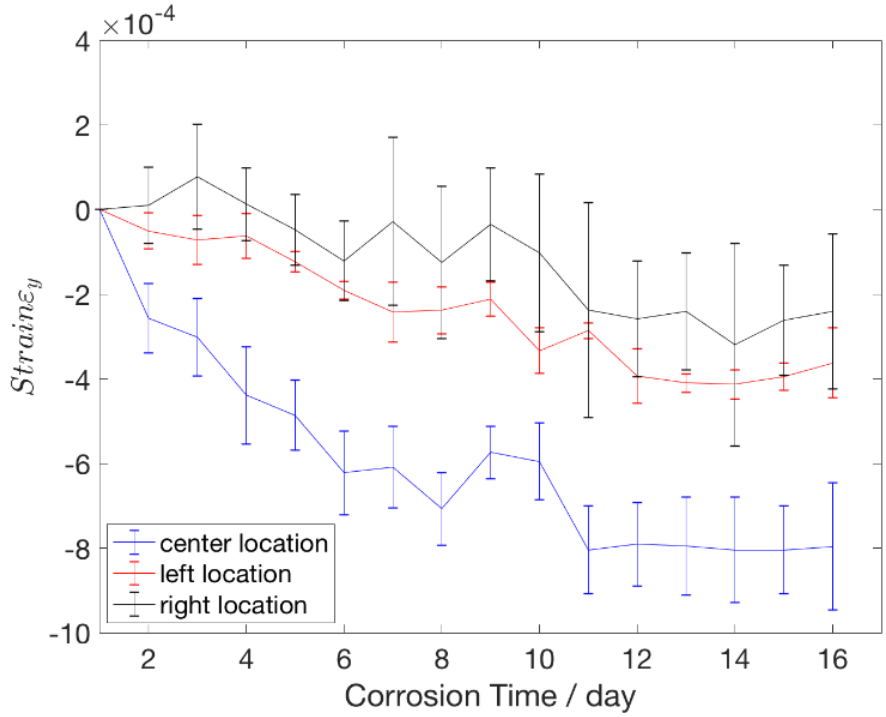



*Figure 70 Strain $\varepsilon_y$ -corrosion time curve for different salt locations of #3 pre-pitted sample*

### 4.3.3 X-ray Tomography

X-ray tomography was used to scan the center and one end corrosion location of the #2 pre-pitted specimen and non pre-pitted specimen (details in 3.5.5). They were firstly scanned in the Deben without load with the resolution of 2.11 μm/pixel, then they were applied a load of 500 N by the Deben and scanned again. According to the X-ray images, no further cracks appeared after loading. Therefore, they were loaded using the Shimadzu to 900 N, and were scanned with a resolution of 1.53 μm/pixel. After reconstruction, a set of images containing 3D data of the samples could be obtained. They can be resliced along different directions to get images of the internal structure of the samples. Figure 71 and Figure 72 show a slice of data closely parallel to the surface of #2 pre-pitted sample, center location and end location, before and

after loading by Shimadzu. Figure 73 and Figure 74 show that of non pre-pitted sample, center location and end location, before and after loading by Shimadzu. In the images of the center location of #2 pre-pitted specimen, many cracks can be observed. The zoomed images of six corrosion areas of #2 pre-pitted sample-center-load are shown in Figure 75, and the 3D visualization of one crack deriving from the pit is shown in Figure 76. The cracks have developed from the pits and are perpendicular to the direction of loading. Similarly, cracks can be observed in the image of the center location of the non pre-pitted sample (Figure 73), but the number of cracks observed in the non pre-pitted sample is smaller than that observed in the pre-pitted sample. By contrast, in the images for the end locations, most corrosion is caused by pitting. Compared the image before and after loading, there is no small crack appearing after the elongation.

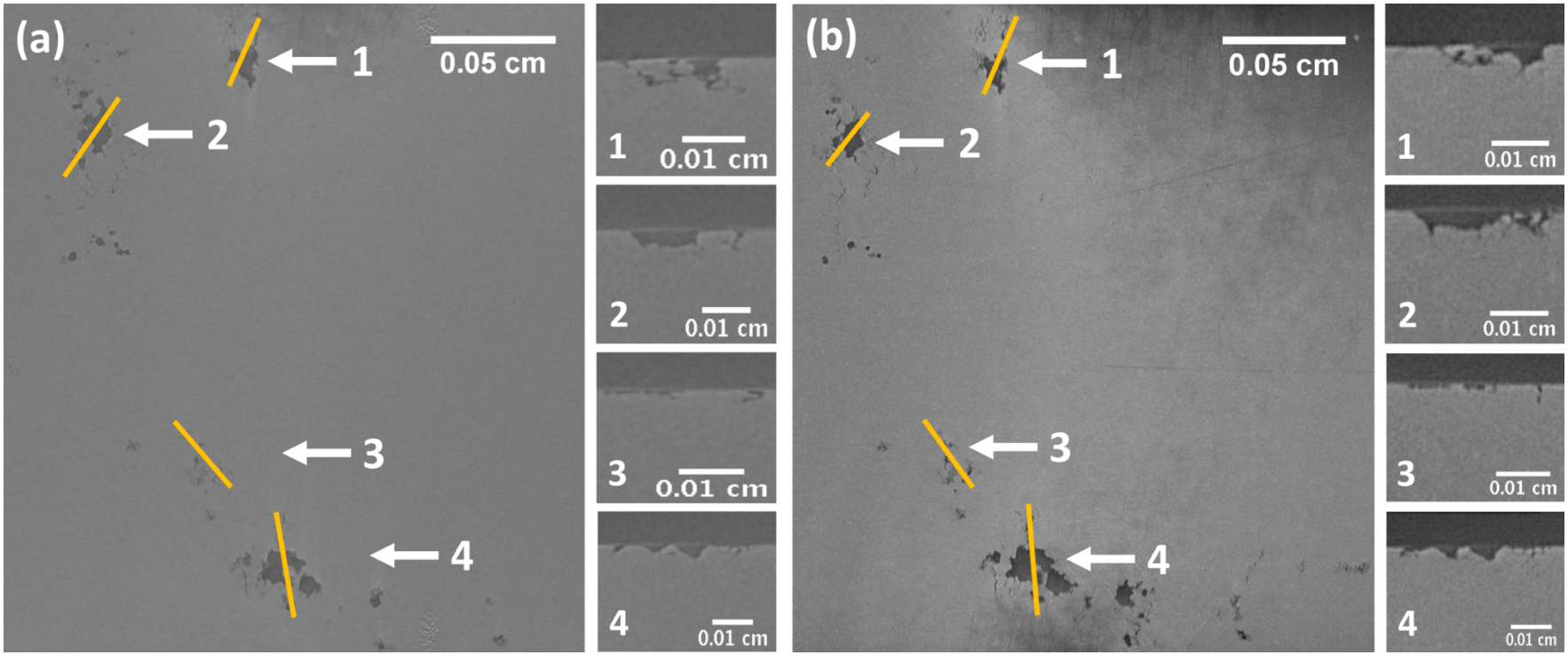



*Figure 71 Xradia image of the center location of #2 pre-pitted specimen (a) before loading and (b) after loading (the load was applied along the horizontal direction)*

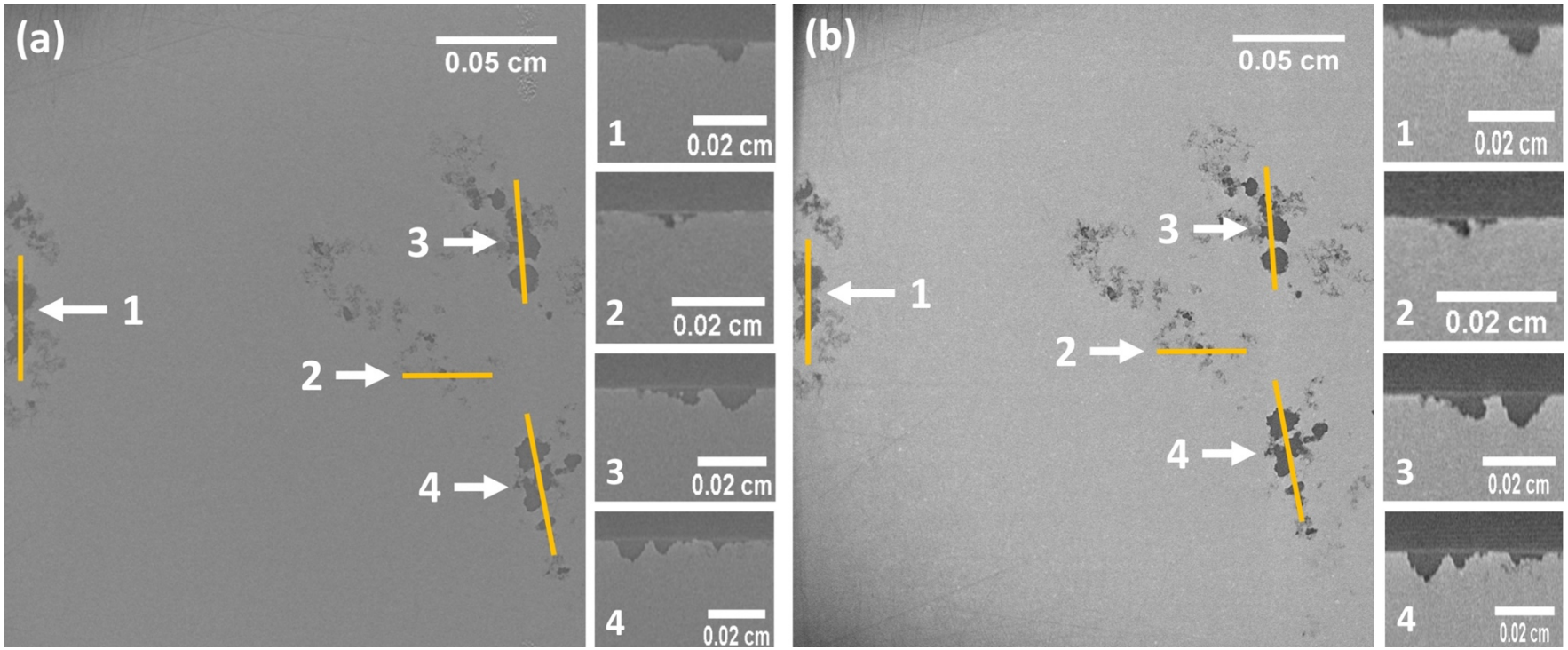



*Figure 72 Xradia image of the end location of #2 pre-pitted specimen (a) before loading and (b) after loading (the load was applied along the horizontal direction)*

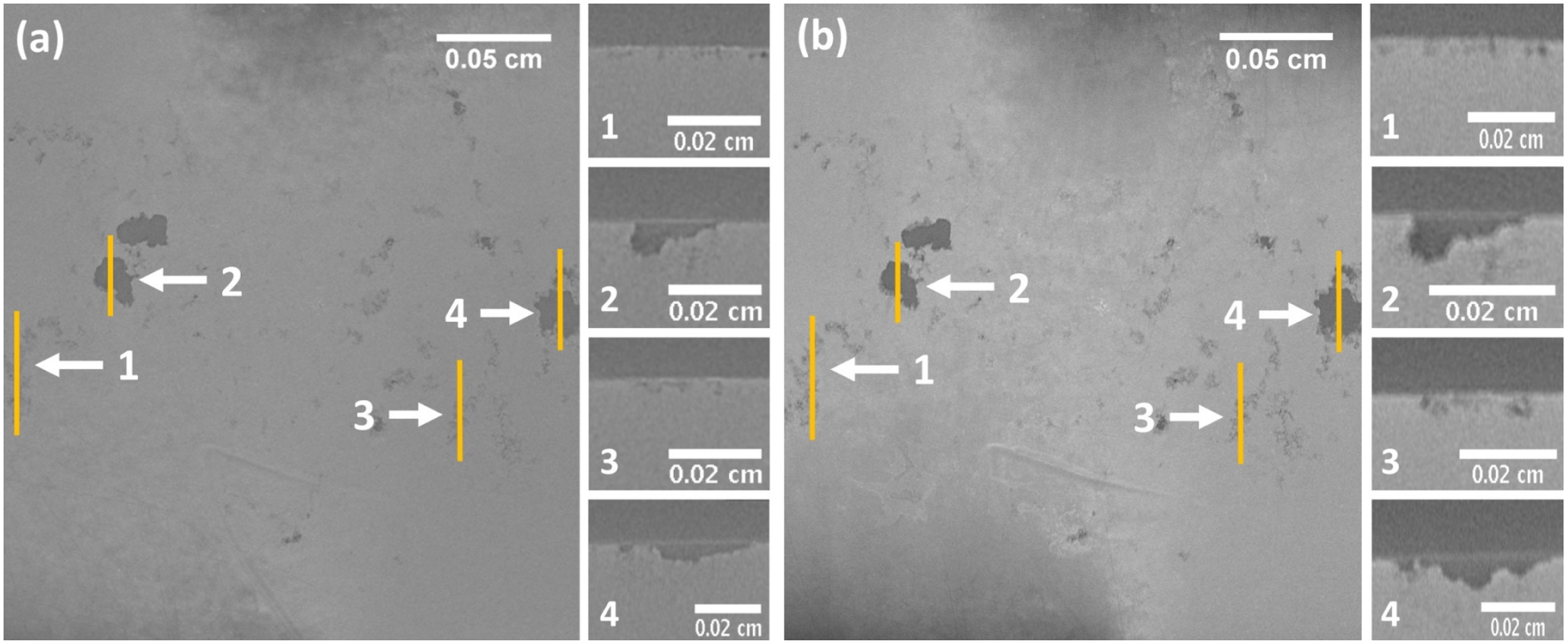



*Figure 73 Xradia image of the center location of non pre-pitted specimen (a) before loading and (b) after loading (the load was applied along the horizontal direction)*

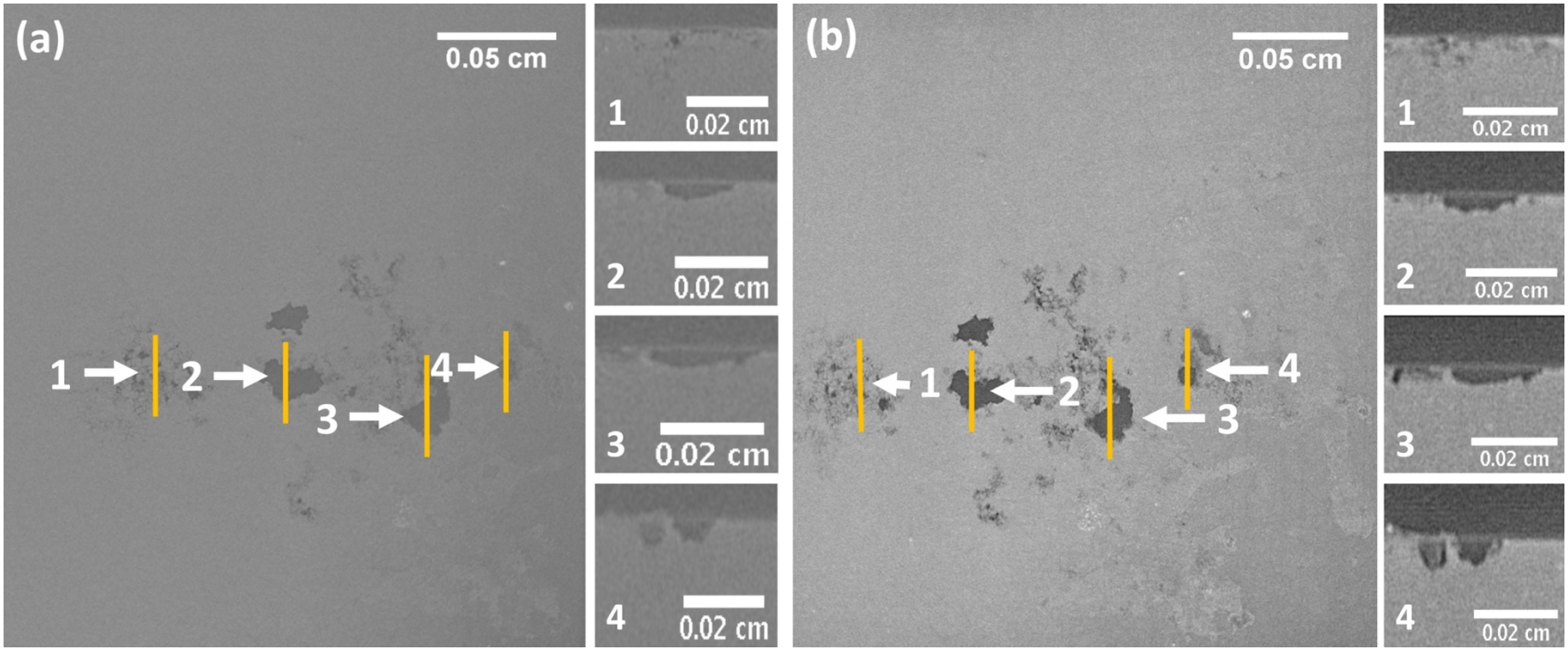



*Figure 74 Xradia image of the end location of non pre-pitted specimen (a) before loading and (b) after loading (the load was applied along the horizontal direction)*

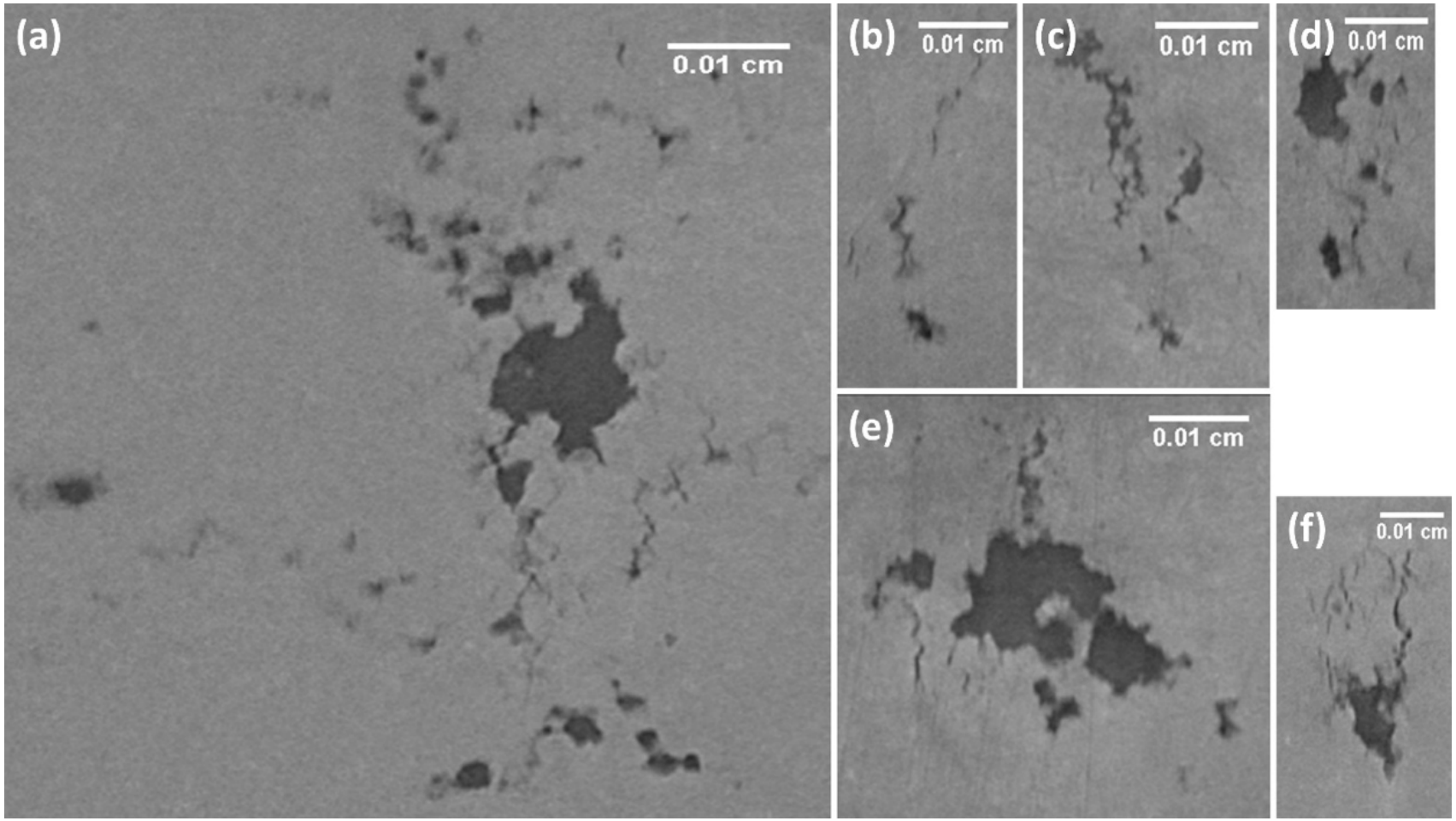



*Figure 75 Zoomed images of six corrosion areas of #2 pre-pitted sample-center-load (the load was applied along the horizontal direction)*

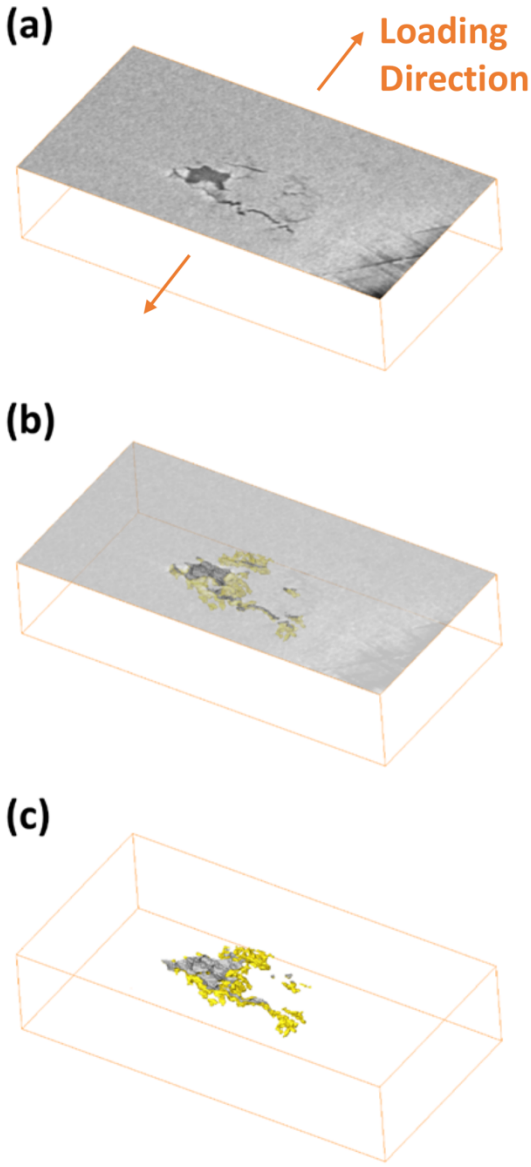



*Figure 76 3D visualization of the crack deriving from the pit. The work was done by James Edmiston, Magdalen College School, work experience student*

In order to quantitatively compare the corrosion on different locations and different specimens, Image J was used to measure the depth of pitting and cracks developing from it. Figure 77 shows the measurement process. The 3D data was resliced into a series of images parallel to the surface with the gap of 1 pixel. For example, for the

corrosion area as shown in location 2 of Figure 71, Figure 77 (a) is the image when the pitting and crack is about to appear, and (b) shows when the pitting and crack appear together. Then, with the increase of depth, the pitting disappears while the crack still exists (c). By counting the number of images between (a) and (c), and multiplying it with the resolution, the depth of pits can be obtained. Later, with the further depth increase, the crack also disappears, and the depth of it can be measured using the same method. The uncertainty of measurement comes from the miscounting of the number of images, and it will not exceed two images (two pixels). On the center location and one end location of each specimen, four locations were measured, as highlighted from Figure 71 to Figure 74, and the results are represented in Table 6. '/' represents there is no crack near that pitting area, or a single crack did not develop from the pitting. They are drawn as stacked columns in Figure 78 to Figure 81. The height of the black columns is the depth of pitting, while that of the red columns is the additional depth of cracks after the pitting disappears. The total height of the stacked columns is the depth of that corrosion area.

It can be observed that for two locations on two specimens, the depth appears to increase after loading, but the increment is not significant. The depth is not related with the location (applied strain), since the average depth of the end location of #2 pre-pitted sample (61±8 μm before loading) is larger than that of the center location (54±8 μm before loading), while the average depth of the end location of non pre-pitted sample (58±8 μm before loading) is smaller than that of the center location (84±8 μm before loading).

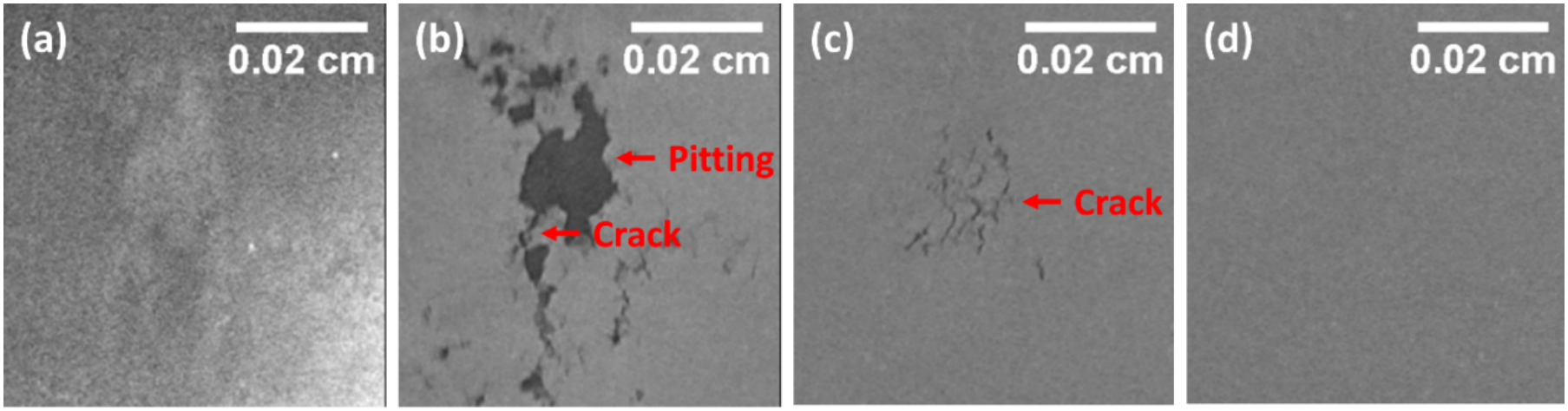



*Figure 77 X-ray images of the pre-pitted sample when (a) the pitting and crack are about to appear, (b) both pitting and crack appear, (c) the pitting disappears and (d) the crack disappears*

*Table 6 The depth of pitting and cracks developing from it (all dimensions in μm)*

| Location | | | 1 | 2 | 3 | 4 |
|---|---|---|---|---|---|---|
| Pre-pitted sample Center location | Unload | Pitting | 36±4 | 38±4 | 8±4 | 36±4 |
| | | Crack | 32±4 | 27±4 | 23±4 | 15±4 |
| | Load | Pitting | 37±3 | 41±3 | 12±3 | 35±3 |
| | | Crack | 32±3 | 26±3 | 23±3 | 15±3 |
| Pre-pitted sample End location | Unload | Pitting | 44±4 | 70±4 | 65±4 | 66±4 |
| | | Crack | / | / | / | / |
| | Load | Pitting | 47±3 | 73±3 | 67±3 | 70±3 |
| | | Crack | / | / | / | / |
| Non pre-pitted sample Center location | Unload | Pitting | 27±4 | 67±4 | / | 44±4 |
| | | Crack | 38±4 | 29±4 | 101±4 | 29±4 |
| | Load | Pitting | 28±3 | 69±3 | / | 46±3 |
| | | Crack | 50±3 | 20±3 | 108±3 | 34±3 |
| Non pre-pitted sample End location | Unload | Pitting | 86±4 | 57±4 | 42±4 | 46±4 |
| | | Crack | / | / | / | / |
| | Load | Pitting | 86±3 | 61±3 | 44±3 | 49±3 |
| | | Crack | / | / | / | / |

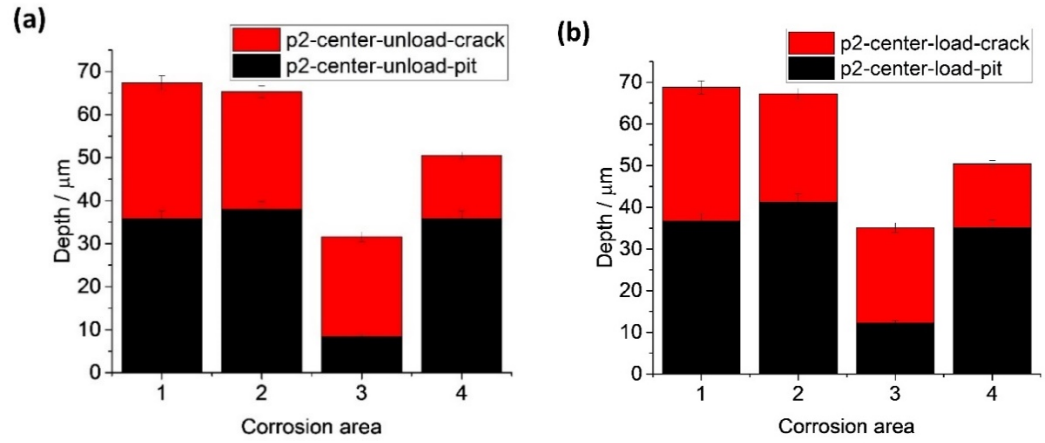



*Figure 78 The depth of pitting and cracks of the center location of #2 pre-pitted sample (a) before loading and (b) after loading*

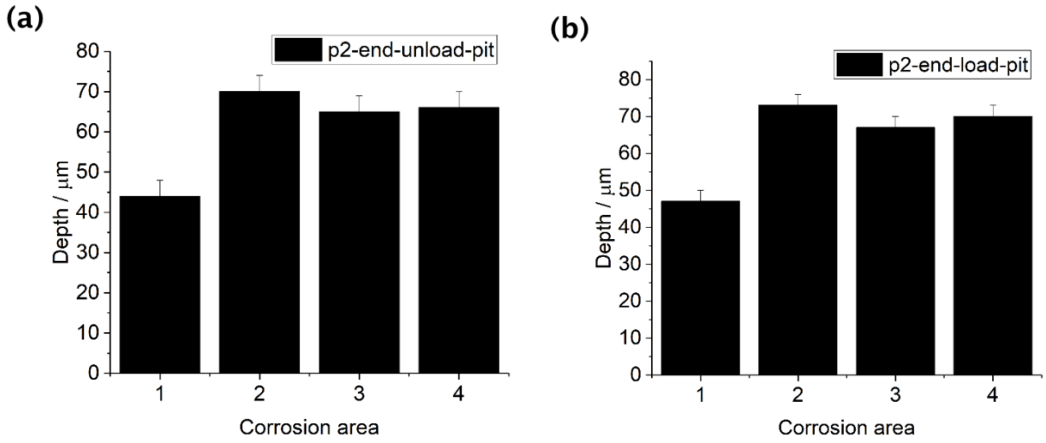



*Figure 79 The depth of pitting and cracks of the end location of #2 pre-pitted sample (a) before loading and (b) after loading*

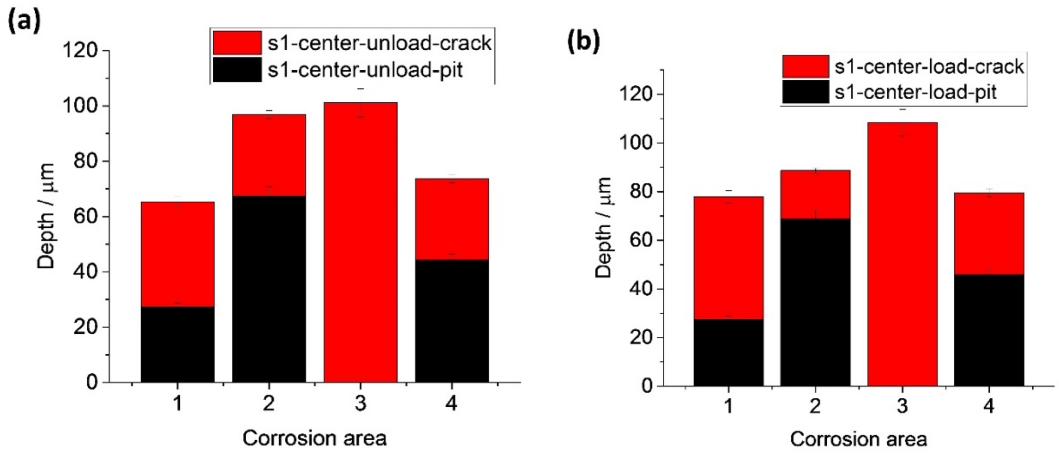



*Figure 80 The depth of pitting and cracks of the center location of non pre-pitted sample (a) before loading and (b) after loading*

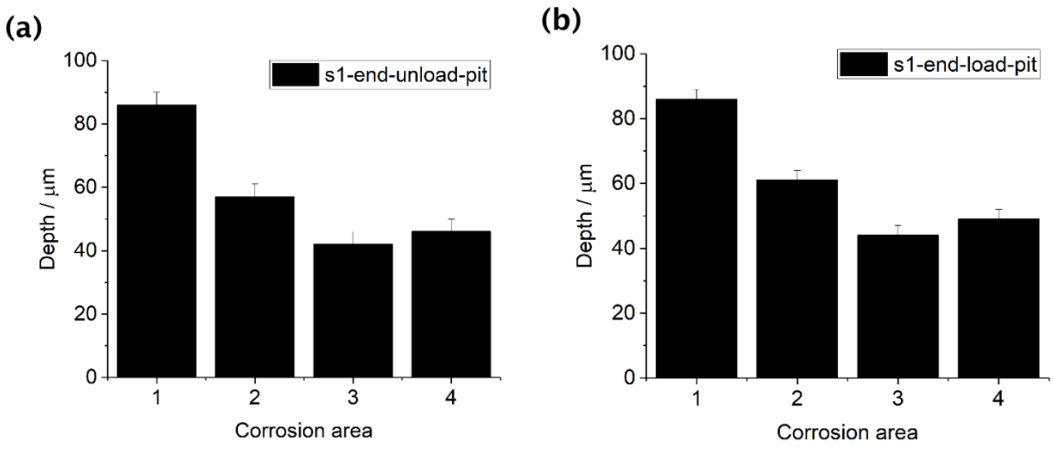



*Figure 81 The depth of pitting and cracks of the end location of non pre-pitted sample (a) before loading and (b) after loading*

## 4.4 Summary

In many literatures, the 6061 T6 aluminum alloy is reported to be immune to the stress corrosion. However, in this experiment, stress corrosion cracks were observed on the 6061 T6 aluminum alloy specimens.

The 6061 T6 aluminum alloy sheet was machined into taper-shape specimens. On each specimen, three salt deposits were applied by the evaporation of aqueous $MgCl_2$ solution. One salt deposit was at the center of the tapered specimen, while the other two were at the end (see Figure 21). The load was applied through the proving ring, and the applied stress was calculated from the load and the area of cross-section. Because of the taper shape, the applied stress of the center salt deposit location is 1.2±0.1 times of that of the end location. The applied strain was measured by Aramis Gom by correlating images of the tapered specimen before and after loading. Therefore, the effect of the applied stress and strain on the SCC is studied.

To study the effect of the pre-pitting on SCC, three specimens were put in the environmental chamber (40 °C and 30% RH) without load to develop pits for 16 days. Then they were loaded to conduct SCC tests at 40 °C and 30% RH. The results were compared with that of one tapered specimen that was tested under the same environment condition, but without pre-pitting. The microstructure was characterized by XRD, and optical imaging with DIC, SEM, and X-ray tomography were used to investigate the SCC process.

The main observations are summarized as:

- The 6061 T6 aluminum alloy has a hardness of 127±2 HV, a yield stress of 263.2±1.7 MPa, and is mainly textured in (200) direction.
- Using different grinding paper to treat the sample surface does not have

significant influence on the DIC error. When choosing #1200 grinding paper to single grind surface and apply random scratches, with a subset size of 33 pixels and a step size of 5 pixels, the displacement measurement error by DIC was 0.031 pixels (1 pixel is 0.65 μm).

- When specimens had droplets of $MgCl_2$ salt (concentration of 6.48 g•$dm^{-3}$), deposited on their surface and were exposed to a condition of 40 °C and 30% relative humidity without load for 16 days, the surface length of the developed pitting reaches around 0.2 mm, and the depth reaches 0.096±0.017 mm.
- At the load applied in the SCC test, the average strain of an area of 3 mm x 3 mm at the center location is 9.0±2.0% (stress = 316.0±6.7 MPa), and that at the end location is 1.5±1.0% (stress = 263.3±5.6 MPa).
- After 16 days' stress corrosion, under a stress of 316±6.7 MPa (center location) and in an environment of 40 °C and 30% RH, the average strain at the location of an evaporated droplet shows a significant increase in the direction of the applied load. There was a corresponding decrease in strain perpendicular to the direction of the applied load. In locations where the stress was 263±5.6 MPa (end location), there was no measurable change in strain.
- Comparing the strain $\varepsilon_x$ increment of the center location of both the pre-pitted sample (i.e. 16 days pitting before SCC test) and non pre-pitted sample after 16 days' stress corrosion, the average strain $\varepsilon_x$ increment of three pre-pitted samples is (20±1)x$10^{-4}$, while that of the non pre-pitted sample is (13±8)x$10^{-4}$. After a total of 32 days stress corrosion, the strain $\varepsilon_x$ increment of the non pre-pitted sample reached (19±9)x$10^{-4}$.
- Cracks developed that are perpendicular to the loading direction. Almost all

the cracks observed on the pre-pitted sample derived from the pitting, while cracks observed on the non pre-pitted sample did not.

- There is no obvious difference of the depth of pitting and cracks between pre-pitted samples and non pre-pitted sample, and also between the different salt deposit locations (i.e. center and end).

# 5 6061 T6 aluminum based composite

Professor Marina Galano's group has developed a 6061 T6 aluminum based composite which contains 15 wt.% SiC nano particles[58] (details in 3.1). Compared with 6061 T6 aluminum alloy, it has higher strength, but its corrosion resistance had not been studied. As described in chapter 4, the optimal experimental methodology was established when investigating the stress corrosion cracking behavior of 6061 T6 aluminum alloy. In this chapter, the same methodology was adopted to investigate the SCC behavior of 6061 T6 aluminum based composite. Hardness and tensile tests and XRD characterization were also conducted.

## 5.1 Characterization of 6061 T6 aluminum based composite

### 5.1.1 Hardness and yield stress

The average hardness from six impressions was 139±2 HV. Dr. Xia Jiang in Prof. Marina Galano's group has previously studied this material[58], and measured a similar hardness of 137.6±1.7 HV. Therefore, the yield stress tested in that work experiment (307 MPa) has been taken as the yield stress of the composite material in this experiment.

### 5.1.2 Tensile test

Similar to the 6061 T6 aluminum alloy, the tensile test was conducted on the tapered specimen of 6061 T6 aluminum based composite to examine the strain distribution in the SCC test. The samples were prepared and tested using the same method for the 6061 T6 aluminum alloy specimen.

Two areas at the size of 3 mm x 3 mm at the center and one end location (i.e. the locations to be used for droplet placement in the SCC tests) were selected for investigation, as shown in Figure 82. The average strain of two areas is calculated, and the change with the increase of applied load is shown in Figure 83.

Under 1050 N (the load applied to the tapered specimen in the SCC test), the average strain of an area of 3 mm x 3 mm at the center location is 2.1±1.1%, and that at the end location is 0.6±0.3%.

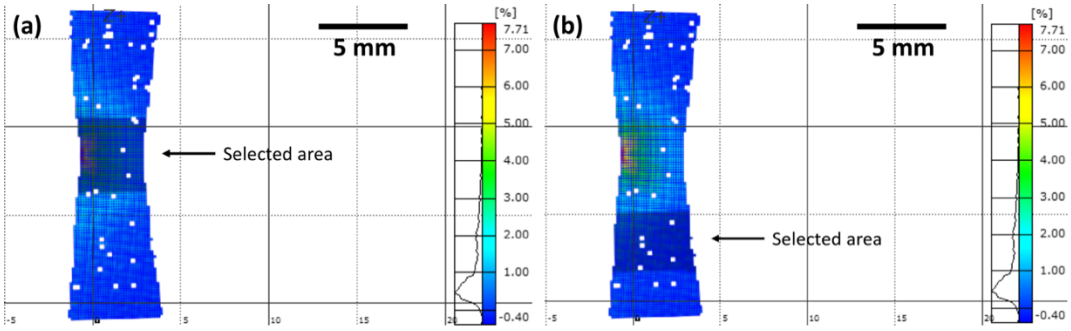



*Figure 82 The map of strain of aluminum alloy based composite specimen along the perpendicular direction (loading direction) under 1050±20 N. (a) the area selected at the center location (b) the area selected at the end location. The blank areas are the areas that cannot be correlated*

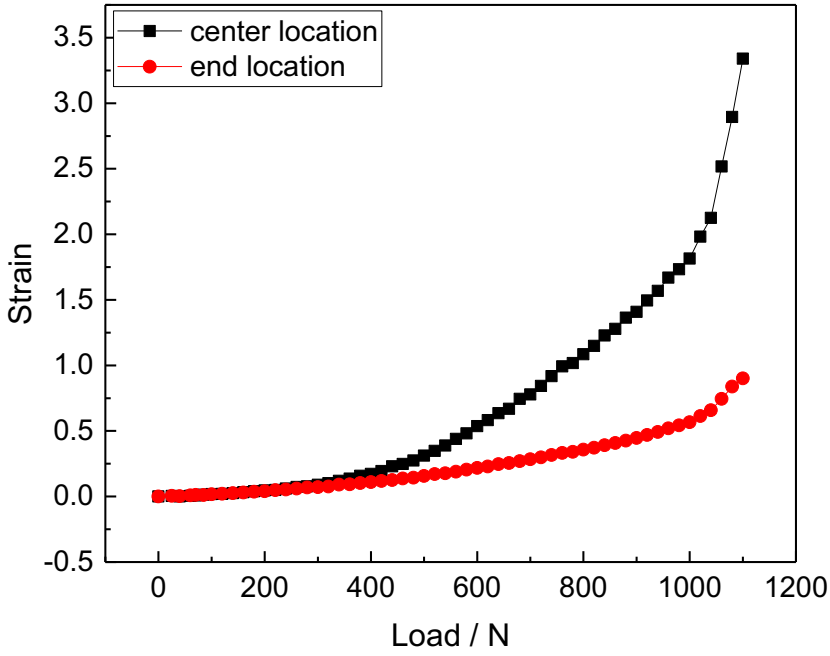



*Figure 83 The strain for two locations of aluminum alloy based composite specimen under different loads*

### 5.1.3 X-ray Diffraction (XRD)

One square coupon sample at the size of 7.5 mm x 7.5 mm was machined from the 6061 T6 aluminum based composite. This section is parallel to the extrusion direction. XRD test was then conducted on this sample, and the result is shown in Figure 84. Similar to the XRD result of the aluminum alloy, the peaks are found at 2 theta values of 38.5°, 44.7°, 65.1°, 78.2° and 82.4°, corresponding to the (111), (200), (220), (311) and (222) planes of aluminum. Because of the addition of SiC particles, peaks of 6H-SiC are found at 34.2°, 35.6°, 41.6°, 60.1°, 71.9°, 73.6°, and 75.7° corresponding to the (101), (102), (104), (110), (116), (203) and (0012) planes.

Figure 85 shows the relative intensity of five aluminum peaks with respect to (111). Compared with the standard pattern for the aluminum, the relative intensity of (220) has the largest difference, which indicates this coupon sample is mainly textured along the (220) direction.

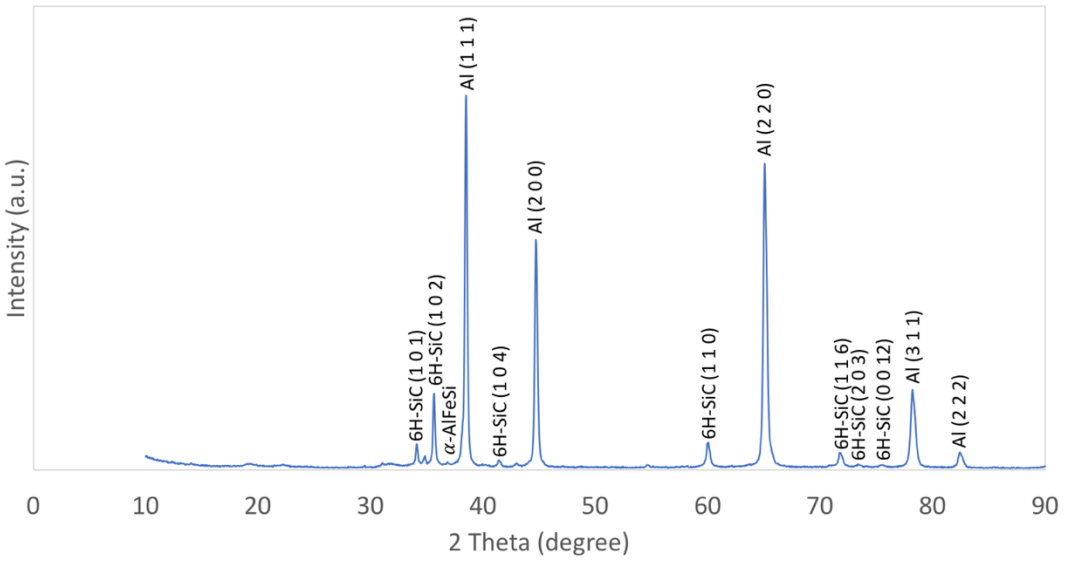



*Figure 84 XRD result of the aluminum alloy based composite*

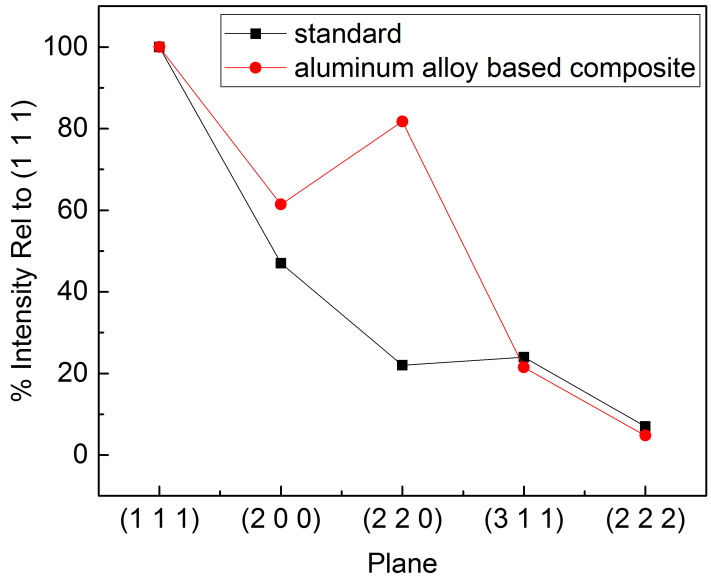



*Figure 85 The relative intensity of peaks with respect (1 1 1)*

## 5.2 Stress corrosion cracking behavior

### 5.2.1 SEM

Stress corrosion cracking testing was conducted on one non pre-pitted sample and one pre-pitted sample of the composite. A load of 1050±20 N was applied to each using the proving ring, and the horizontally diametral change of the proving ring was 0.236±0.004 mm. Three salt droplets were applied to each sample by the evaporation of 5 μl $MgCl_2$ aqueous solution. They were put in the environmental chamber under a constant environmental condition of 40°C and 30% relative humidity for 16 days, and were taken out to capture optical image every day.

After 16 days stress corrosion cracking test, specimens were unloaded from the proving rings, and Zeiss Evo MA10 was used to observe the specimens' surfaces at 7.5 mm working distance, 5 kV working voltage, and 50 pA working current. The center location and one end location of both the pre-pitted specimen and the non pre-pitted specimens were observed. Pitting can be observed on these images, but no cracks are observed. Figure 86 to Figure 88 are example SEM images of the center location and one of the end locations of the non pre-pitted sample, and SEM images of the center location of the pre-pitted sample.

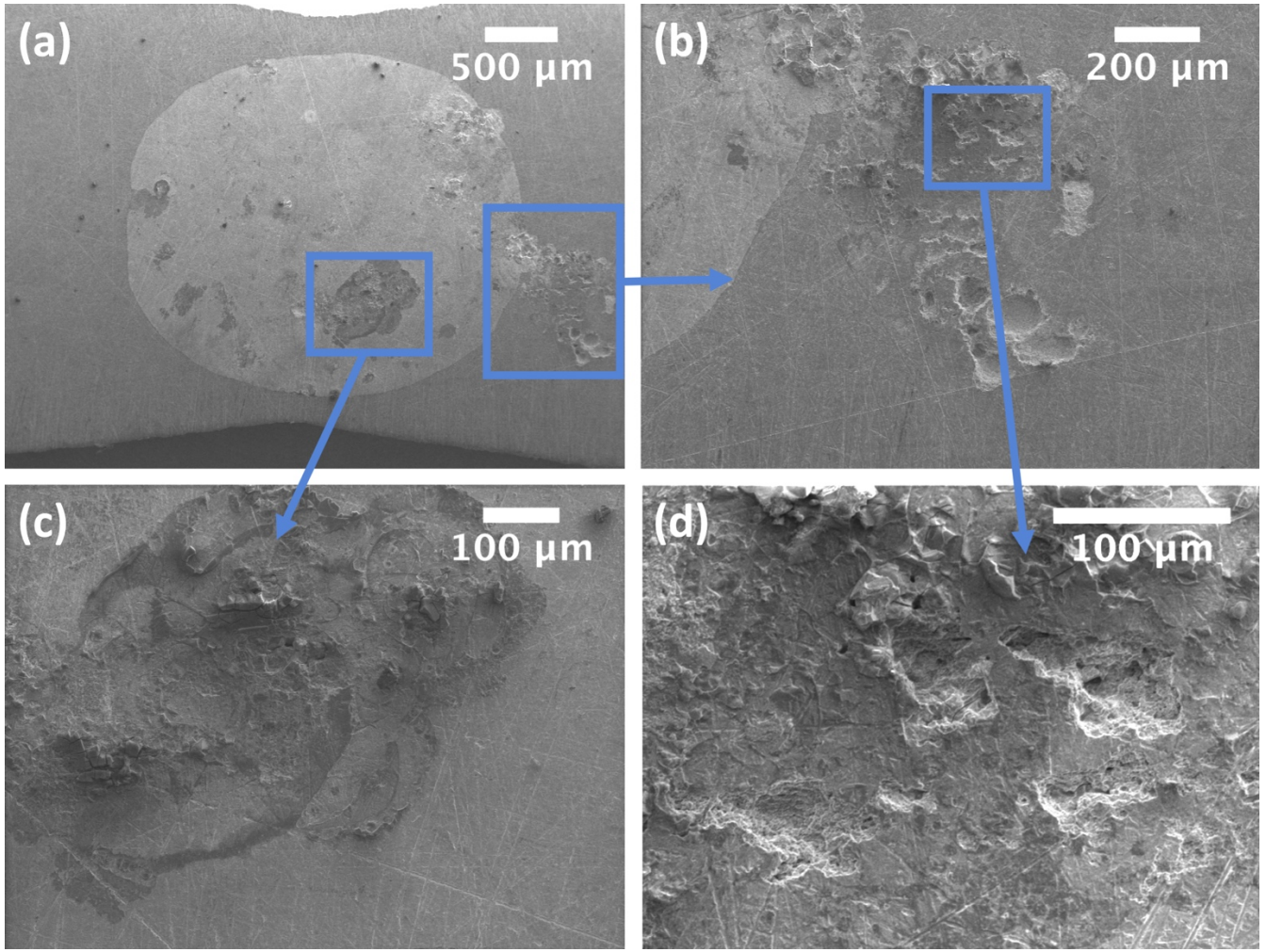



*Figure 86 SEM images for the center location of the non pre-pitted sample*

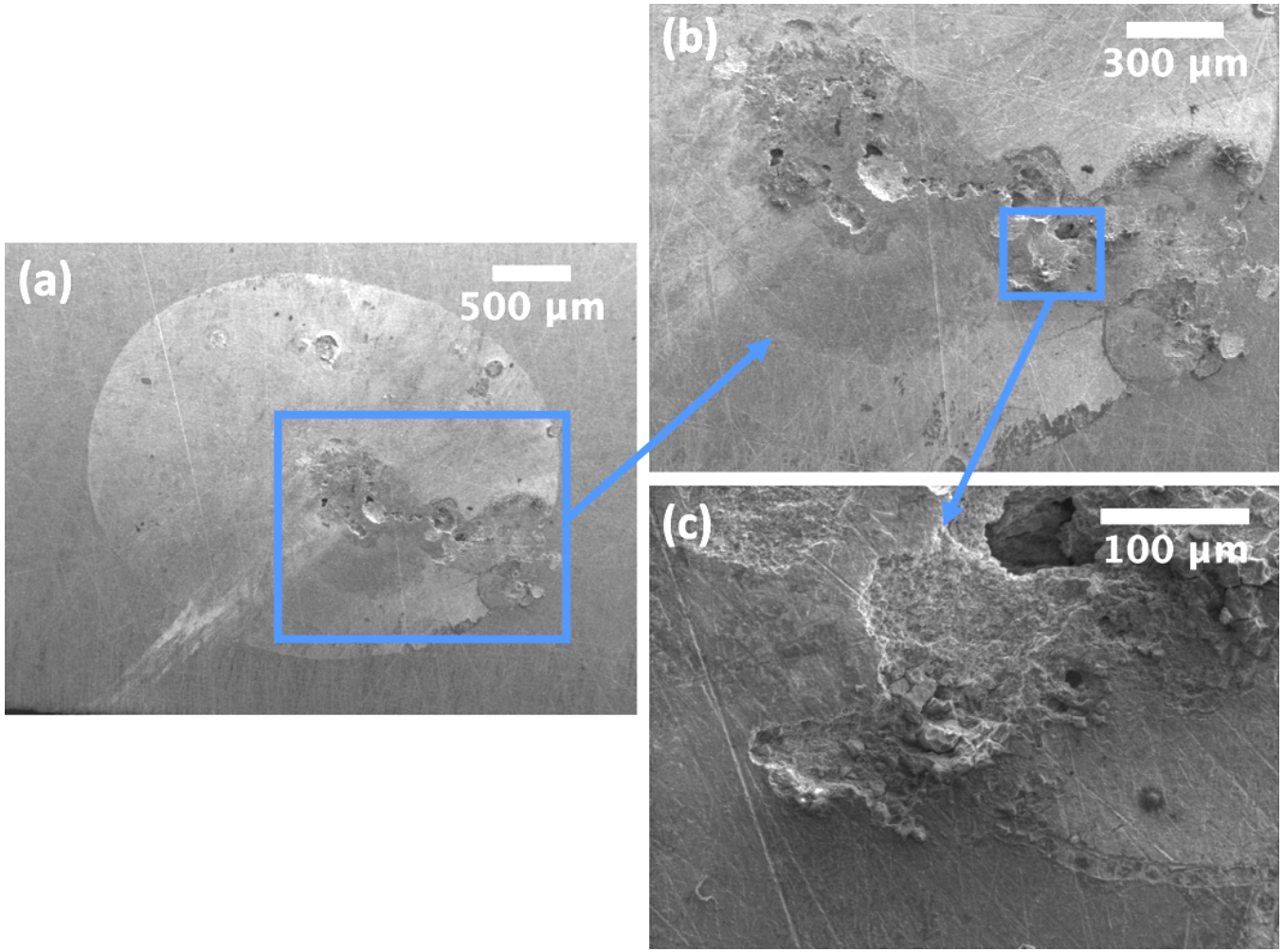



*Figure 87 SEM images for the end location of the non pre-pitted sample*

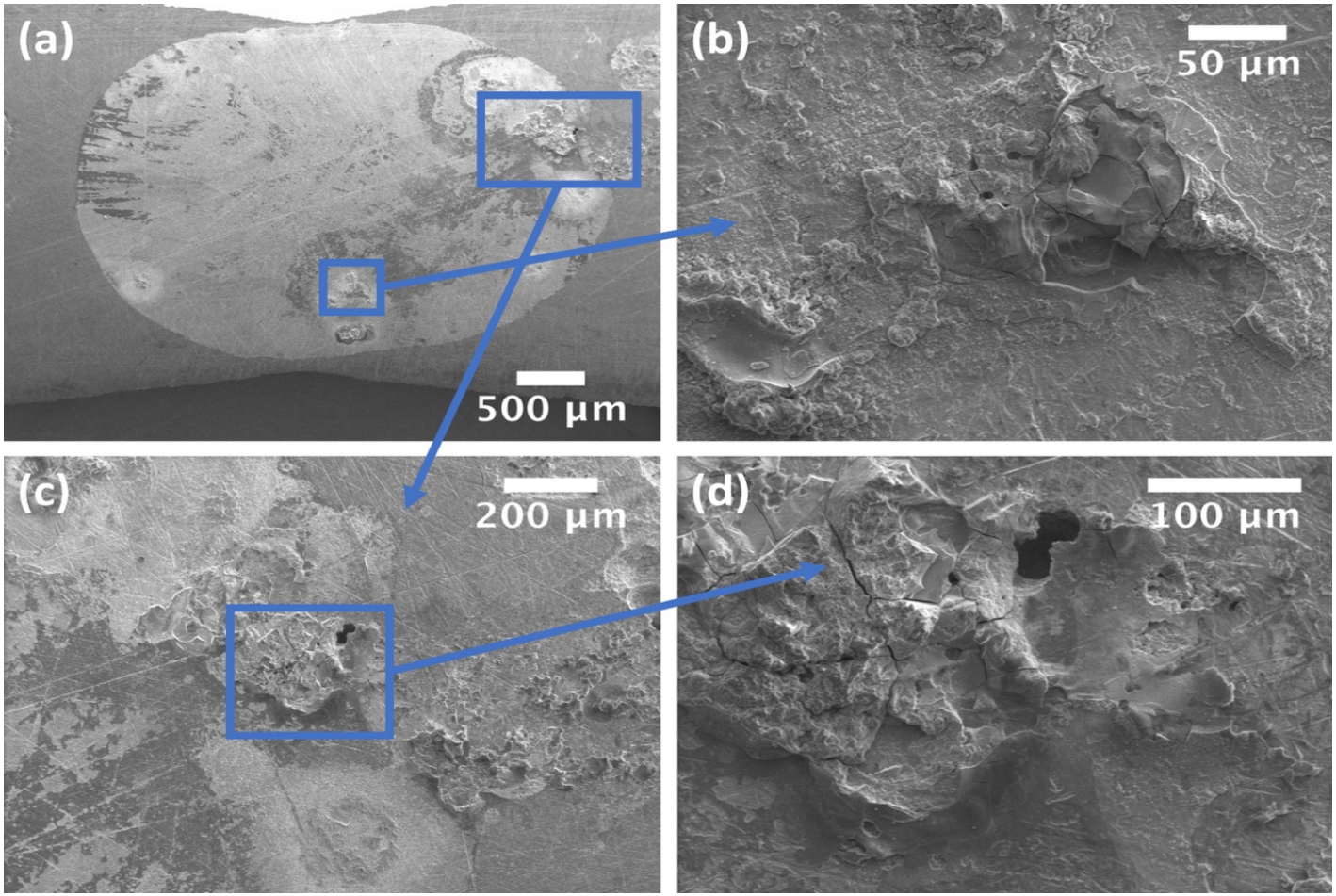



*Figure 88 SEM images for the center locatoin of the pre-pitted sample. In (d), there are cracks on the corrosion products instead of on the sample*

### 5.2.2 DIC

Displacement maps were calculated from the optical images by digital image correlation with the reference of images captured at the start of the SCC test, using the same method used for the 6061 T6 aluminum alloy sample. Stitching of the maps also followed the same method. Figure 89 shows the map of displacement x at the center location for the non pre-pitted sample and pre-pitted sample respectively. After 16 days' stress corrosion, the displacement increment along the loading rection over the salt deposit location is 2.84±0.01 pixels (1.846±0.007 μm) for the pre-pitted specimen, and 1.33±0.01 pixels (0.865±0.007 μm) for the non pre-pitted specimen. These values are significantly smaller than that of the 6061 T6 aluminum alloy specimen. Figure 90 shows the displacement y of the center location of the pre-pitted sample. Similarly, there is only a slight difference of the displacement along the y direction which is 0.36±0.02 pixels (0.234±0.013 μm).

Following the same method as previous (details in 4.4.1.3), a horizontal band with a width of 40 pixels (8 points in the displacement map with the step size of 5 pixels) in the middle of the stitched data was selected, to obtain the specimen's extension along the load direction (x direction). The extension-x coordinate curve was then smoothed with 'rlowess' filter and 150 span size (Figure 91). The gradient of each point at the smoothed curve was calculated by Matlab to obtain a gradient-x coordinate curve. Then, the curve was smoothed again with 'rlowess' filter and 150 span size, and 400 points (1300 μm) over the central maximum were selected. The average value of these points is the strain $\varepsilon_x$ over the location, and their standard devation was calculated as the uncertainty. The change of the strain along the loading direction (x direction) during the SCC testing for both samples are shown in Figure 92. After 16

days' stress corrosion, the strain increment at the center salt deposit location for the pre-pitted sample is $(3.98\pm4.33)\times10^{-4}$, while that for the non pre-pitted sample is $(2.50\pm3.17)\times10^{-4}$. These two strain increment values are equal within the error range. Furthermore, the values fluctuate around 0, indicating that there was no total deformation developed during the test.

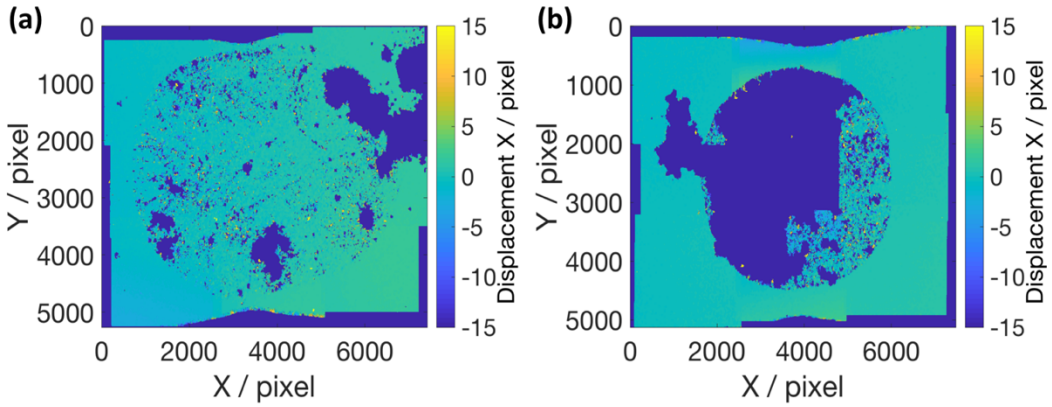



*Figure 89 The stitched map of displacement x at the center location of (a) the pre-pitted sample after 16 days' corrosion, and (b) the non pre-pitted sample after 15 days' corrosion*

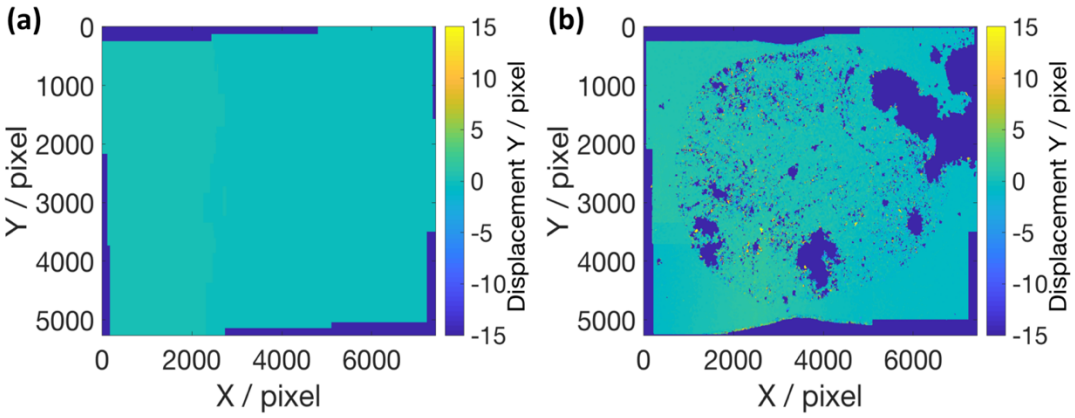



*Figure 90 The stitched map of displacement y at the center location of the pre-pitted sample (a) before corrosion and (b) after 16 days' corrosion*

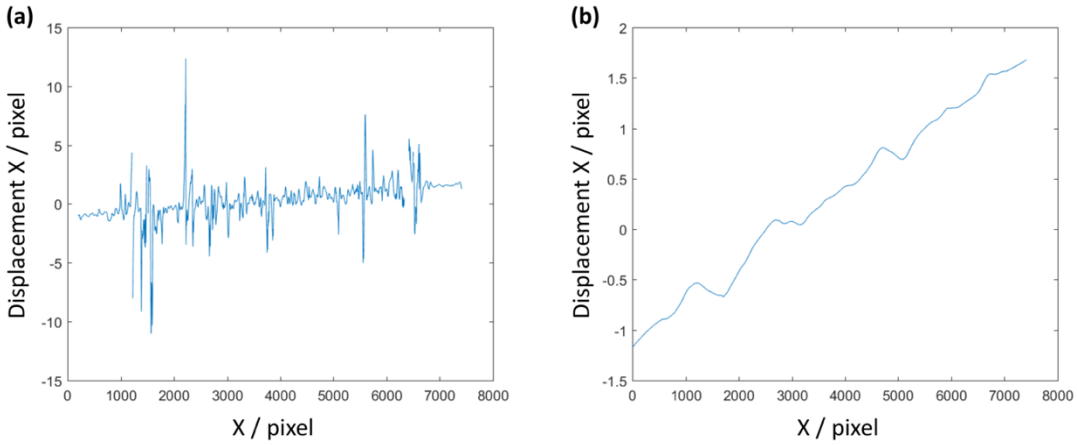



*Figure 91 The displacement x-x curve of the center location of pre-pitted sample after 16 days' stress corrosion. (a) is the original curve, while (b) is smoothed with 'rlowess' filter and 150 span size*

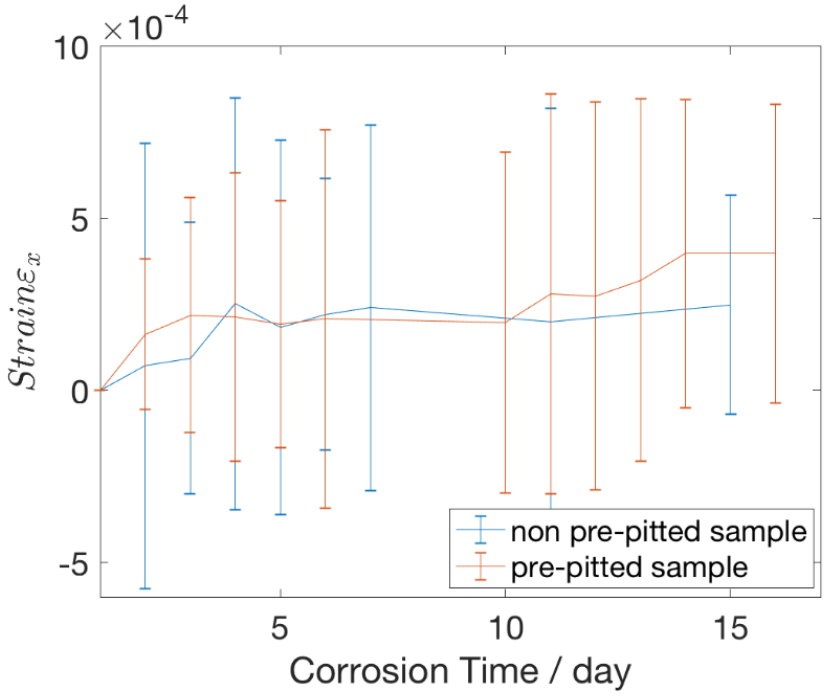



*Figure 92 The change of the strain along x direction along with the increase of corrosion time for the center location of non pre-pitted sample and pre-pitted sample*

### 5.2.3 X-ray Tomography

X-ray tomography was used to scan the center and one end corrosion location of both non pre-pitted and pre-pitted samples in the Deben at 2.11 μm/pixel. They were firstly scanned without load. Then, in order to check if there is any small crack, a load of 1000 N was applied through the Deben, and samples were scanned again under the load. It was observed that 1000 N is the maximum load that can be applied to these samples. After that point, the strain increases, but the load remains the same, which indicates that plastic deformation is occurring.

Figure 93 shows the tomographs of the center location of the non pre-pitted sample. (a) and (b) are slices of the 3D data closely parallel to the surface, before and during loading respectively. Four pitting locations (as the white arrows point to) were selected to measure their depths, and the cross section (as the yellow lines indicate) images of these four locations are shown in (c) and (d). Similarly, Figure 94 to Figure 96 shows the tomographs of the end location of the non pre-pitted sample, the center and end location of the pre-pitted sample respectively. On images of the slices parallel to the surface, only pitting but no cracks are observed at the four locations. The depth of the pitting was measured by counting the number of slices between the images when pitting appears at the surface and disappears. The gap between slices is 1 pixel, and the resolution is 2.11 μm/pixel. Therefore, the depth of the pitting can be calculated. The error is introduced by defining when the pitting appears or disappears. This error is no more than 2 slices, which is ~4 μm.

In

Figure 97, it can be observed that there is no obvious difference between the pitting depth of the pre-pitted sample and the non pre-pitted sample, nor is there any effect of stress on the depth of pitting.

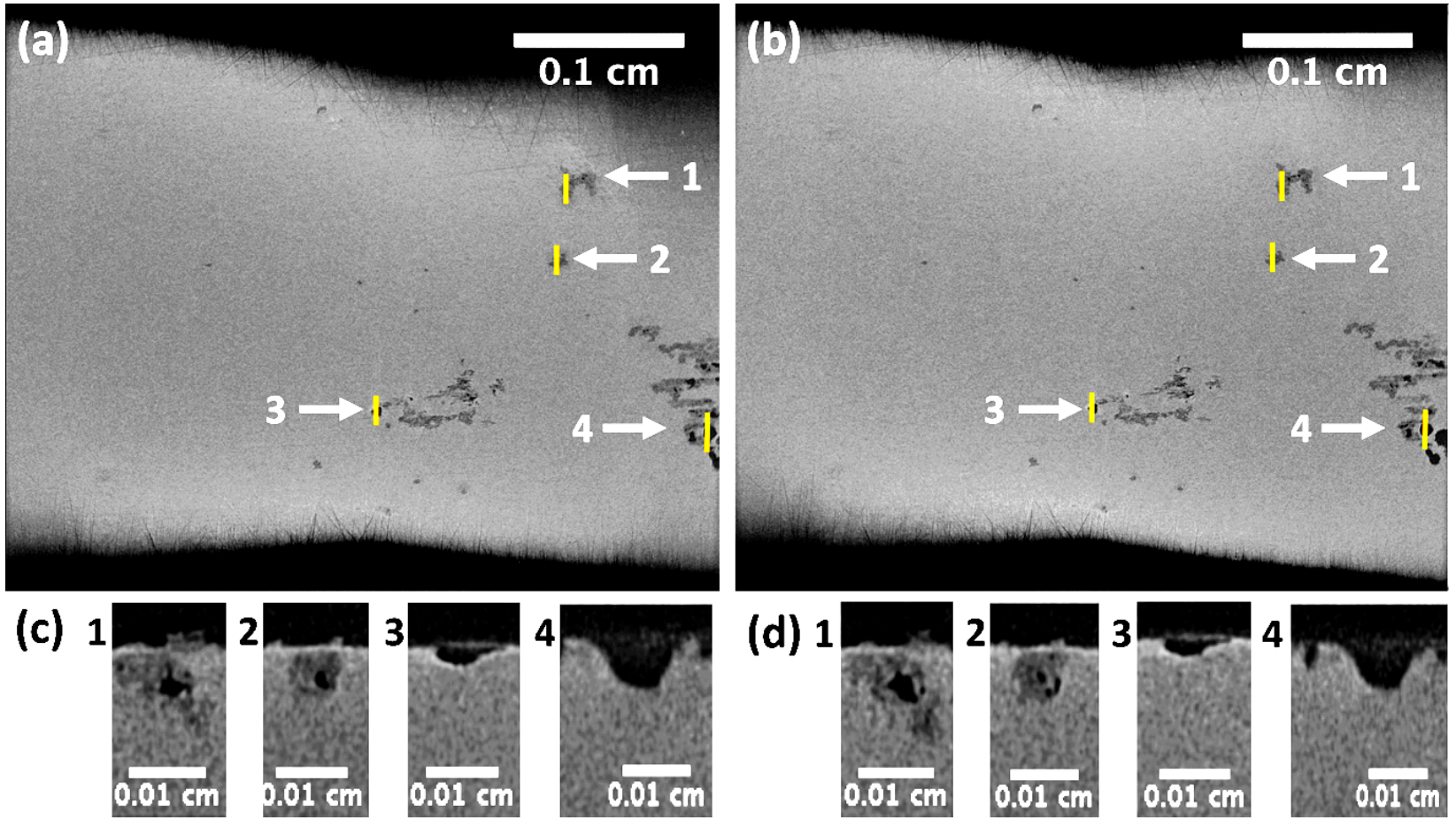



*Figure 93 Xradia image of the center location of the non pre-pitted sample (a) before loading and (b) after loading (the load was applied along the horizontal direction)*

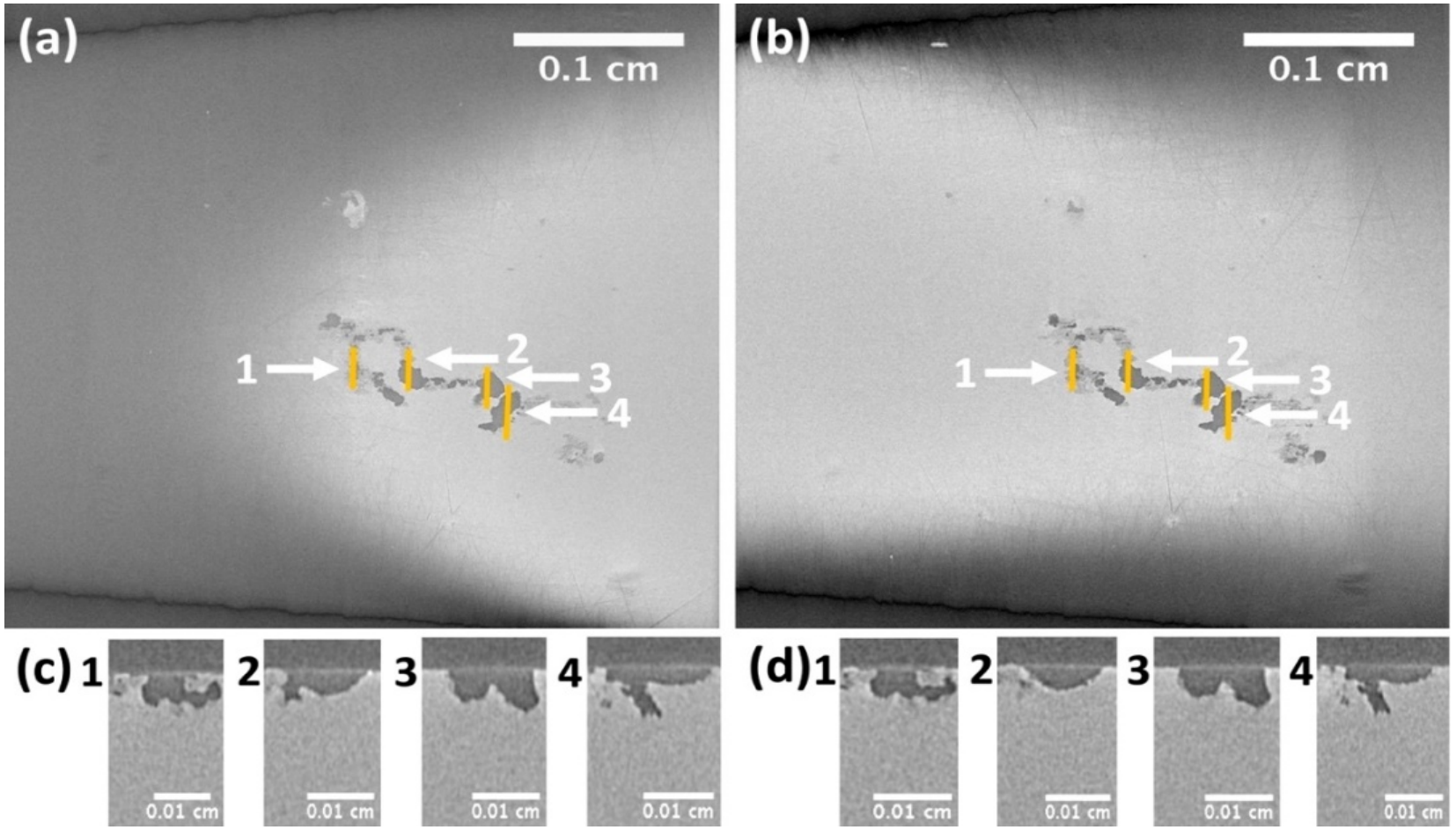



*Figure 94 Xradia image of the end location of the non pre-pitted sample (a) before loading and (b) after loading (the load was applied along the horizontal direction)*

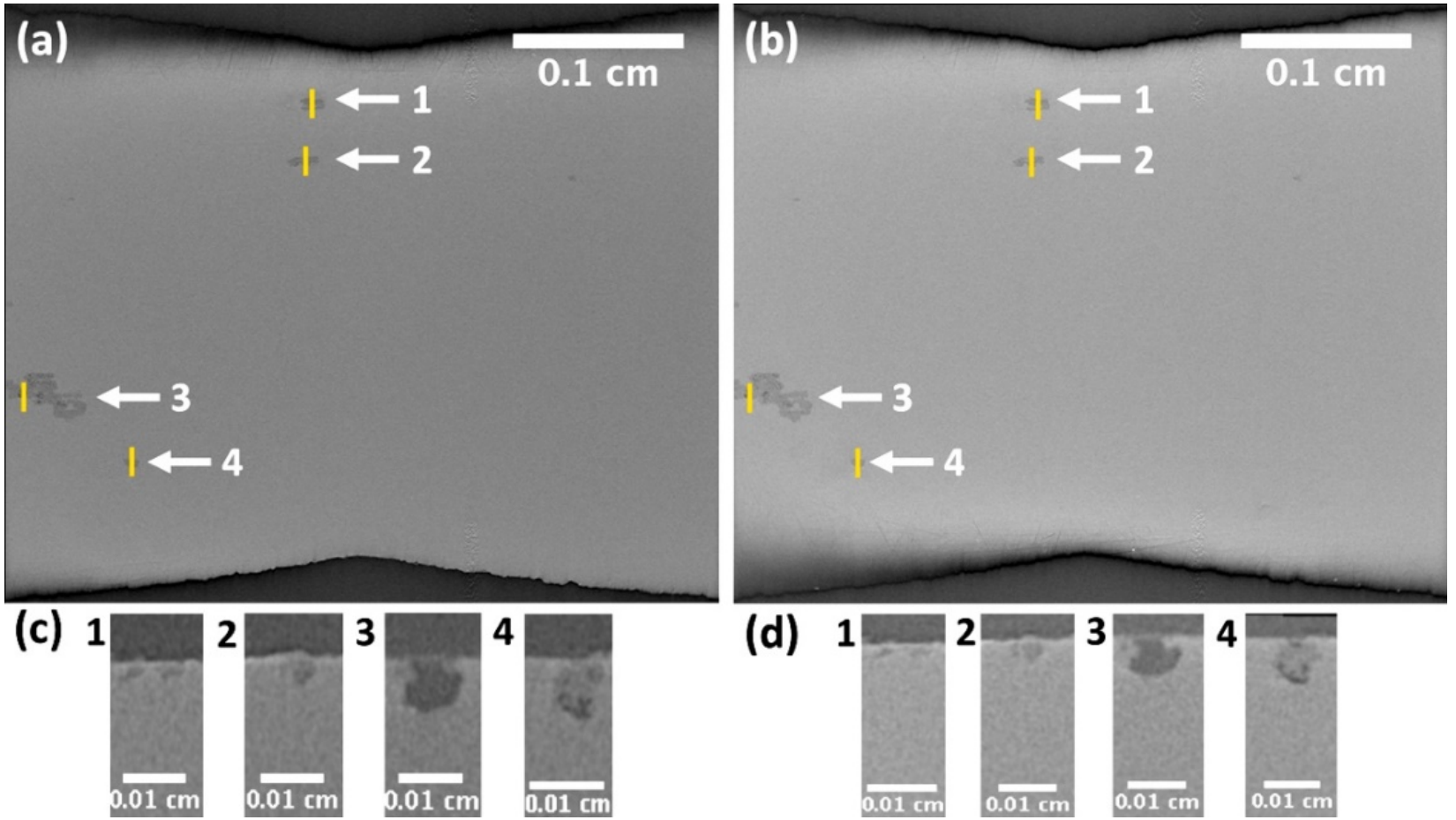



*Figure 95 Xradia image of the center location of the pre-pitted sample (a) before loading and (b) after loading (the load was applied along the horizontal direction)*

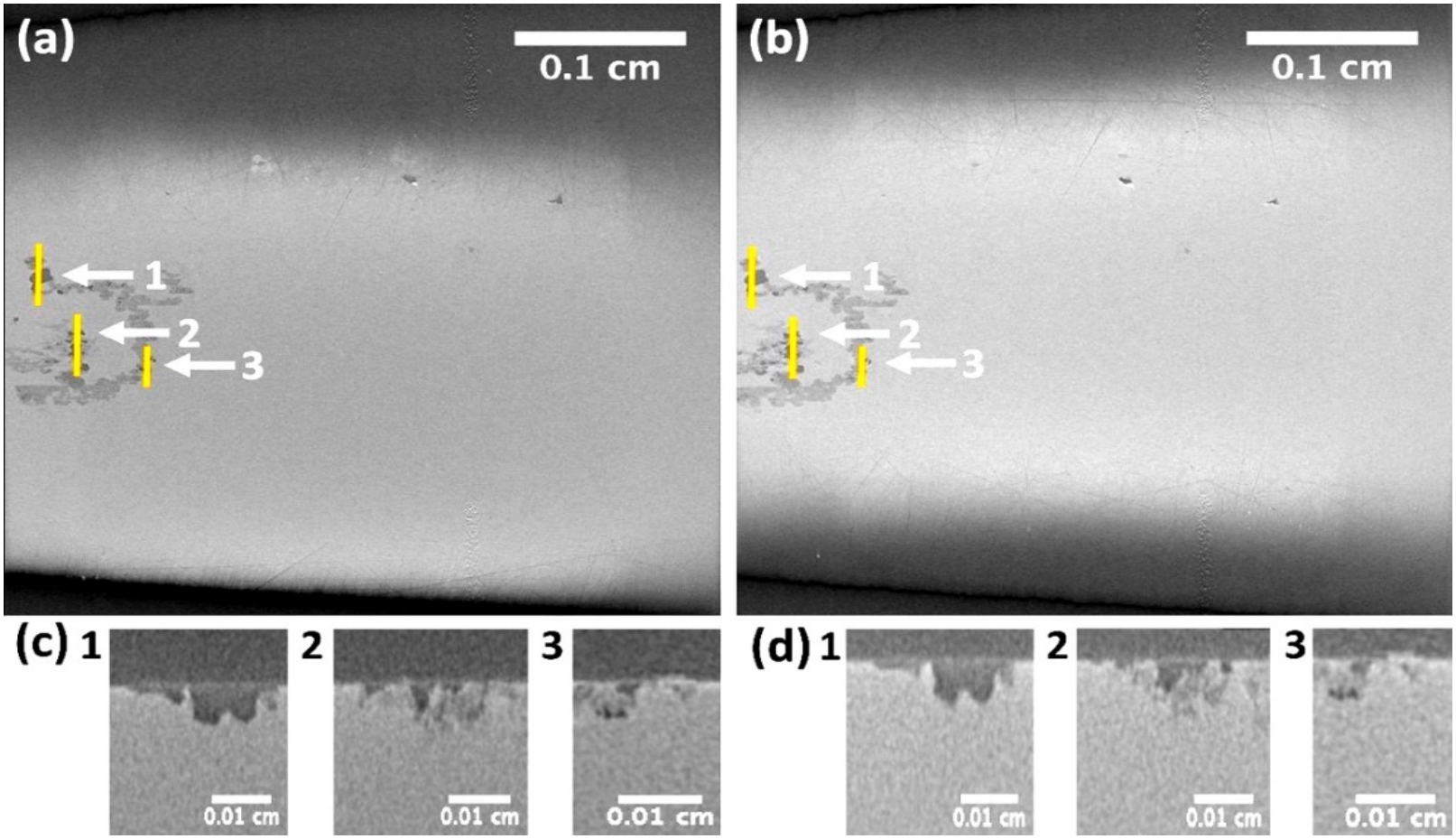



*Figure 96 Xradia image of the end location of the pre-pitted sample (a) before loading and (b) after loading (the load was applied along the horizontal direction)*

*Table 7 The depth of pitting (μm) on four SCC samples*

| Location | | 1 | 2 | 3 | 4 |
|---|---|---|---|---|---|
| Non Pre-pitted Sample | Unload | 84±4 | 72±4 | 24±4 | 89±4 |
| Center Location | Load | 86±4 | 70±4 | 26±4 | 93±4 |
| Non Pre-pitted Sample | Unload | 72±4 | 56±4 | 88±4 | 88±4 |
| End Location | Load | 72±4 | 56±4 | 88±4 | 88±4 |
| Pre-pitted Sample | Unload | 40±4 | 50±4 | 86±4 | 84±4 |
| Center Location | Load | 40±4 | 50±4 | 88±4 | 84±4 |
| Pre-pitted Sample | Unload | 76±4 | 76±4 | 52±4 | / |
| End Location | Load | 76±4 | 76±4 | 52±4 | / |

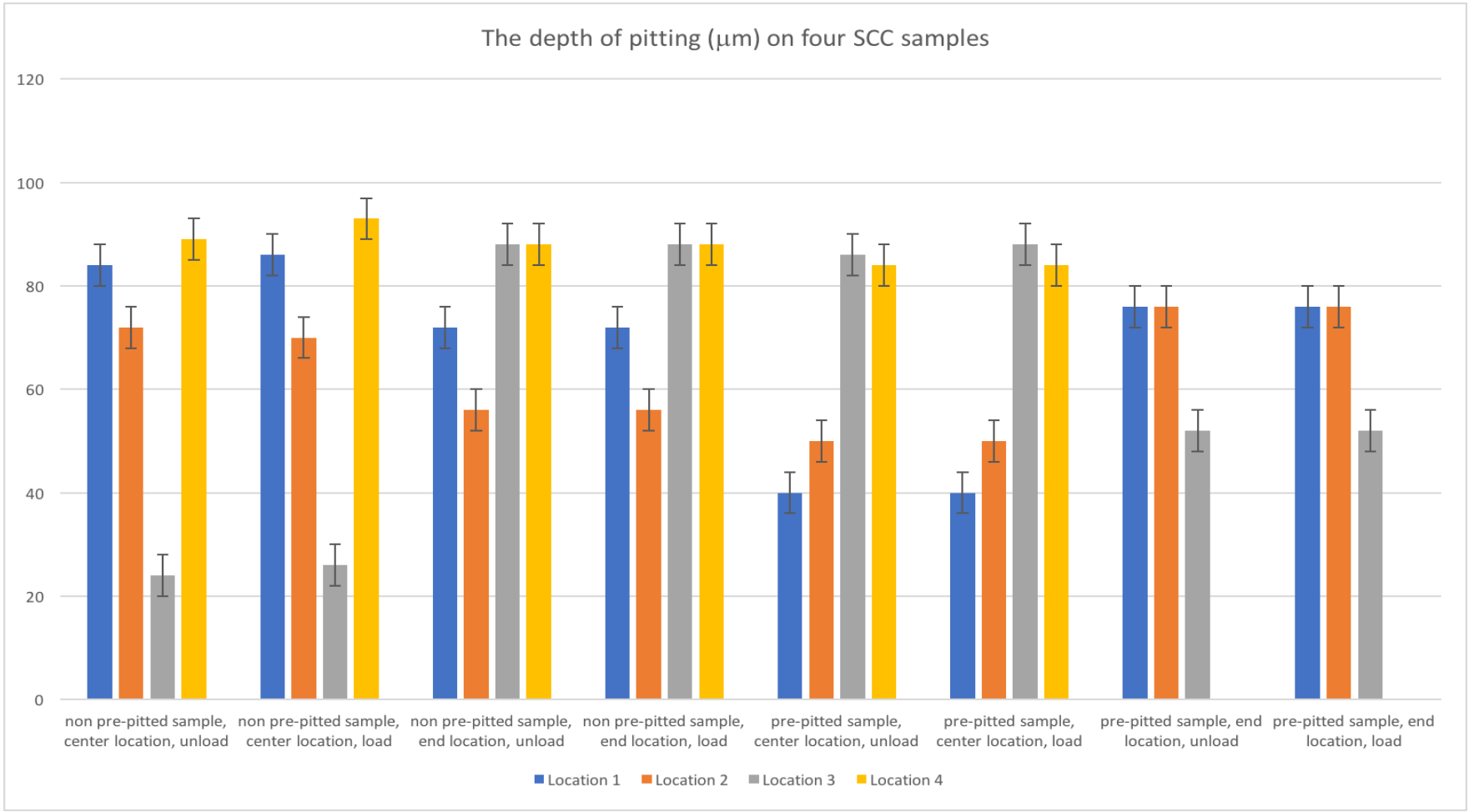



*Figure 97 The depth of pitting (μm) on four SCC samples*

## 5.3 Summary

In this chapter, SCC tests were conducted on the SiC nano particles reinforced 6061 T6 aluminum using the same methodology as applied to the 6061 T6 aluminum alloy.

The main results are summarized as follows:

- The composite material has a hardness of 139±2 HV, and is mainly textured along the (220) direction.
- At the applied load of the SCC test, the average strain of the area at the center location in the tapered specimen is 2.1±1.1% (stress = 350.0±6.7 MPa), while that at the end location is 0.6±0.3% (stress = 291.7±5.6 MPa).
- After 16 days' stress corrosion under a load of 1050±20 N and an environment of 40 °C and 30% RH, the strain along the loading direction (strain $\varepsilon_x$) over the center salt deposit location for all specimens shows a small apparent increase but essentially fluctuates around 0.
- Comparing the strain $\varepsilon_x$ increment of the center location of both the pre-pitted sample and non pre-pitted sample after 16 days' stress corrosion, the strain $\varepsilon_x$ increment of the pre-pitted sample is $(3.98\pm4.33)\times10^{-4}$, while that of the non pre-pitted sample is $(2.50\pm3.17)\times10^{-4}$.
- Pitting but no cracking was observed.
- There is no obvious difference of the depth of pitting between pre-pitted samples and non pre-pitted sample, and also between the different salt deposit locations of one sample.

# 6 Discussion

## 6.1 6061 T6 aluminum alloy

### 6.1.1 Characterization

#### 6.1.1.1 Hardness

The Vickers hardness of 6061 T6 aluminum alloy was 127 ± 2 HV. Khairia Salman Hassan et. al. tested the hardness of 6061 T6 aluminum alloy, which is 100 HV[90]. ASM Aerospace Specification Metals, Inc. reported a hardness of 107 HV. The tested hardness of the 6061 T6 aluminum alloy in this program is higher than the result of other researchers by at least 17%. The possible reason is the aluminum alloy in this program is machined by rolling. According to Bo Wang et. al.'s research on AA 5052 aluminum alloy, when the rolling reduction reaches 87%, the hardness of the rolled aluminum alloy can be as high as two times of that of the as-homogenized one[91].

#### 6.1.1.2 Yield stress

The yield stress of the 6061 T6 aluminum alloy was 263.2±1.7 MPa. That reported by MakeItFrom.com is 270 MPa, which is slightly higher than tested value in this project by 6.8±1.7 MPa. This difference may be because of orientation. The sample was machined along the rolling direction. According to Latifah Mohd Najib's research, as the angle between the sample and the rolling direction increases, the tensile strength increases as well[92].

#### 6.1.1.3 Texture

The XRD test shows the aluminum alloy sheet is textured in (200) direction (Figure 33), and the annealing process did not remove the texture. Carlos Reyes-Ruiz et. al. did the XRD test on a 6061 T6 aluminum alloy bar, and found it was also textured in (200) direction[93]. This preferred orientation is a result of the grains slip and rotation during the deformation of rolling, and is determined by the applied forces[94]. The texture coefficient of (200) is calculated according to the Equation 3[95,96]:

*Equation 3* $$T.C_{(hkl)} = \frac{I_{hkl}/I_{0(hkl)}}{(1/N)\sum_{i=1}^{N} I_{i(hkl)}/I_{0i(hkl)}}$$

where $I_{i(hkl)}$ is the intensity of the peak of (hkl) plane of the tested material, while $I_{0(hkl)}$ is that of a completely random sample from the Powder Diffraction File (PDF) card. N is the number of reflections.

It is calculated that the texture coefficient of the (200) plane for the as-received 6061 T6 aluminum alloy rolled sheet is 3.06, while that of the annealed sample is 2.97, decreasing by 2.9%. The texture may only reduce a little because of the insufficient annealing temperature and time. Ejaz Ahmad et. al. investigated the texture change of the rolled low alloy steel under different annealing temperatures, and found its deformation texture along (200) direction gradually reduced with the increase of annealing temperatures[94].

### 6.1.2 DIC precision

In order to test the effect of different grits with SiC paper on the DIC precision, 400, 600, 800, 1200 and 2500 grit with SiC paper were used to grind the sample surface respectively. According to the result (Figure 35), there is no obvious difference of DIC error between the samples treated by different grinding papers. A. Cook et. al.

tested #400, #600, #800 and #1200 grinding paper, and also did not find measurable difference. Besides, in their experiment, when choosing a subset size of 32 x 32 pixels, the DIC error is 1.2 pixels[80]. In this experiment, a subset size of 33 x 33 pixels was selected to correlate images, and the DIC error is 1.9 pixels. The main reason for the difference is that in A. Cook et. al.'s experiment, although the sample was removed and replaced under microscope, the focus and light of the microscope were fixed. Therefore, the DIC error was mainly induced by the transition and rotation when placing the sample. In this study, apart from the DIC error induced by the position change of the sample, there is also the DIC error caused by small changes in the microscope setup between observations. As shown in Figure 37 and Figure 38, an aperture difference of 0.5 results in a DIC error of 0.45 pixels, while a focus difference of 20 μm results in a DIC error of 0.06 pixels.

### 6.1.3 Pitting

In order to observe the pitting corrosion of 6061 T6 aluminum alloy, coupon samples were applied 5 μl of $MgCl_2$ solution with the concentration of 6.48 g•$dm^{-3}$. Then by the evaporation, the solution droplet turned into $MgCl_2$ salt deposit with the density of 460 μg•$cm^{-2}$. Later coupon samples were put in the environmental chamber with the constant temperature of 40 °C and relative humidity of 30%, in which corrosive environment the salt deposit can form a layer of aqueous solution on the surface[80]. After 1 day's corrosion, pitting at the size of 20 μm can be observed on the surface under SEM (Figure 42). R. Braun also investigated the pitting corrosion of 6061 T6 aluminum alloy sheet. It was immersed in an aqueous chloride-peroxide solution for 24 hours, and obtained a pitting size of 100 μm on the surface[97]. The larger pitting

size in his experiment may be mainly attributed to the $H_2O_2$/ $H_2O$ reaction, which gradually increases the pH of solution[98].

In the corrosion process, the Al-Fe-Si phase in the 6061 T6 aluminum alloy served as the cathode, and its effect depends on the pH of the solution. At high pH, the material tends to have general corrosion with pitting on the grain boundary[99]. H. Ding immersed the 6061 T6 aluminum alloy in 3.15 wt% NaCl solution containing $NaHCO_3$ for 90 days, and observed pitting on the surface is around 10μm[100].

In this study, after 8 days' corrosion, it can be observed that pits develop outwards from the salt deposits (Figure 44). This phenomenon was also observed in M. S. Thomson et. al.'s study[101].

### 6.1.4 Stress corrosion cracking

As mentioned in the literature review, 6061 T6 aluminum alloy is reported to be not susceptible to stress corrosion cracking. For instance, R. Braun conducted SCC tests on 6061 T6 aluminum alloy using two-point and four-point loaded bent beam specimens, and applied a stress of 80% to 90% of the yield stress. They were alternately immersed in 3.5% NaCl solution, but did not fail during 90 days' test[97]. In this study, cracks were observed on the specimens that had been stressed to 120% of the yield stress with a concentrated $MgCl_2$ salt film. The possible reasons for this difference in behavior may therefore be the corrosive environment, applied stress, and the application of pre-pitting. These parameters will be discussed below.

#### 6.1.4.1 Corrosive environment

For stress corrosion cracking, a higher temperature and relative humidity will prompt this process and accelerate the corrosion rate (discussed in the literature review,

noted by Joseph R. Davis[9]). In this experiment, the specimens were put in a constant temperature of 40°C and relative humidity of 30%. This is a relatively mild condition, and below 40°C, the SCC is mainly assigned to anodic dissolution and grain boundary deformation[102].

The $MgCl_2$ was used in this experiment for the corrosive solution, since the required concentration to form an aqueous solution under 40°C and 30% RH had already been identified[80]. One study found there was no obvious difference between the corrosion potential of the NaCl and $MgCl_2$ droplets[101]. The SCC process mainly depends on the concentration of $Cl^-$, since it interacts with the oxide film at the crack tip[103]. Furthermore, the concentration of $Cl^-$ plays a key role in the process of crack initiation from the pitting[104].

#### 6.1.4.2 Applied stress

According to the experiment result, the cracks were found at the location applied 120% of the yield stress (applied strain 9.0±2.0%) but were not found at the location where the stress was at 100% of the yield stress (applied strain 1.5±1.0%) for both non pre-pitted sample and pre-pitted sample. According to previous researches, there is a threshold stress for the SCC, and below that value, the crack cannot initiate. This value can be dramatically affected by the environment, but the mechanism of it remains unknown[44]. As mentioned in the literature review, there are three possible mechanisms for the SCC, and one of them is active path dissolution. Precipitates at the grain boundaries can be active during the corrosion process, and therefore, the localized corrosion may happen near these places. When applied a load, the stress concentrates near these locations because of the geometry (i.e. mismatch between the deformation of adjacent grains). A minimum stress may be required to open and

connect these corrosion areas to form intergranular cracks. For this experiment, it can be concluded that the threshold stress for the crack initiation is between 1 to 1.2 times of the yield stress, which corresponds to 263 MPa to 316 MPa. The stress that can induce the stress corrosion cracks is therefore near the ultimate stress of the material. According to the stress-strain curve obtained at the center location of the tapered sample, the ultimate stress is 320±3 MPa. However, this is another possibility that the observed SCC is attributed to the intergranular corrosion, and the applied stress opened the corroded pathways.

Cracks were observed at the center location of both pre-pitted sample and non pre-pitted sample of 6061 T6 aluminum alloy (Figure 71 and Figure 73). All of the observed cracks are almost perpendicular to the loading direction.

This can be explained by the Griffith criterion, which points out that the driven force for the crack propagation is to lower the total system energy. When applied a load, the strain energy of the specimen increases along the loading direction[105]. With the propagation of the crack along a direction perpendicular to the loading direction, new free surfaces appear, and the strain energy of these areas are released[106].

Another phenomenon is that the strain across the salt deposit location only increases at the first day of SCC test for the pre-pitted sample and then reaches the plateau of $(20\pm1)\times10^{-4}$. For the non pre-pitted sample, the strain increases slowly, and finally ends at $(19\pm9)\times10^{-4}$ (Figure 68).

The possible reason is that during the material's deformation process, the grain boundaries inhibit the crystal slip, and the piled-up dislocations generate large shear stress around these areas[107]. The large stress promotes the propagation of cracks. However, with the development of cracks, the local stress decreases, and so does the crack propagation rate. This suggests that cracking is driven by the local stresses that

result from the incompatibility of plastic deformation in the grains. That is why SCC is mostly observed at the locations that have been strained above the yield stress.

#### 6.1.4.3 Pre-pitting

Comparing the result of the center location of pre-pitted sample and non pre-pitted sample, it can be observed that the strain increase over the salt deposit location of the pre-pitted sample reaches the plateau after one-day's SCC test, but that of the non pre-pitted sample gradually increases (Figure 68).

Comparing the DIC result of the center location and the end location of the specimens, it can be concluded that only cracks and not pitting can result in the obvious strain increment (Figure 69). Therefore, this indicates that with the existence of pitting, the crack initiation and propagation speed is accelerated, but it does not affect the strain that is developed, which is dependent on the total amount of cracking.

One possible reason for this phenomenon is that the pitting can accelerate the SCC process since stress concentrates around this area, and also the localized corrosion causes an aggressive solution chemistry[108, 109]. From the X-ray images of the pre-pitted sample, it can be observed that most cracks derive from the pitting (Figure 75). By contrast, for the non pre-pitted sample, cracks did not derive from the pitting (see Figure 73, location 1 and 3). According to the literature review, the local corrosion of the slip plane can induce cracks without pre-pitting, but it takes longer time for crack to develop. The cracks are more likely to initiate from the pitting that has an aspect ratio larger than 0.5[42]. The X-ray tomography result shows, after 16 days corrosion without load, the aspect ratio of the 6061 T6 aluminum alloy specimen is around 0.5 (Figure 46), satisfying this condition.

However, the amount of cracking depends on the amount of strain that is applied, which controls the amount of intergranular strain. As discussed in 6.1.4.2, the short cracks develop under high strain. With the propagation of cracks, the strain energy gradually decreases, and the intergranular strain is relaxed. When the intergranular strain is sufficiently reduced, the crack development stops. Therefore, the pre-pitting can accelerate the SCC process, but the total amount of cracking is the same with or without pitting when applied the same strain.

## 6.2 6061 T6 aluminum based composite

### 6.2.1 Characterization

This composite was developed by Prof. Marina Galano's group, and the characteristics of this material has been tested by Dr. Xia Jiang. In this experiment, they were tested again for the purpose of verification. The measured hardness of the composite was 139.0±1.8 HV. In Xia Jiang's paper, the microhardness of the material was tested with a load of 500 g, and the measured hardness is 137.6±1.7 HV[58].

### 6.2.2 Stress corrosion cracking

The SCC tests of the 6061 T6 aluminum based composite were conducted under the same environmental conditions as the 6061 T6 aluminum alloy, although with a higher applied load. The DIC result shows there is no significant strain increase over the salt deposit location either at the center location or at the end location over 16 days' SCC test. Furthermore, the SEM and X-ray tomography also show that there is only pitting but no cracks developed (Figure 86 to Figure 88, and Figure 93 to Figure 96). The different SCC behavior between the 6061 T6 aluminum alloy and that alloy

based composite may be due to differences in applied stress, strain, or the addition of SiC nano particles. These influence factors are discussed as follow.

### 6.2.2.1 Applied stress

Both materials were machined into the same shape, and the applied load of the composite is 1050±20 N, while that of the aluminum alloy is 948±20 N. The applied stress of the composite is 1.11 times of that of the aluminum alloy. From the data for yield stress, the applied stress at the center of the composite specimen is 114% of the yield stress, compare to 120% of the yield stress in the non-composite alloy samples. This indicates that the applied stress is not the key simple factor influencing the crack initiation and propagation. The applied stress and strain to the center and end locations of two kinds of specimen is shown in Figure 98.

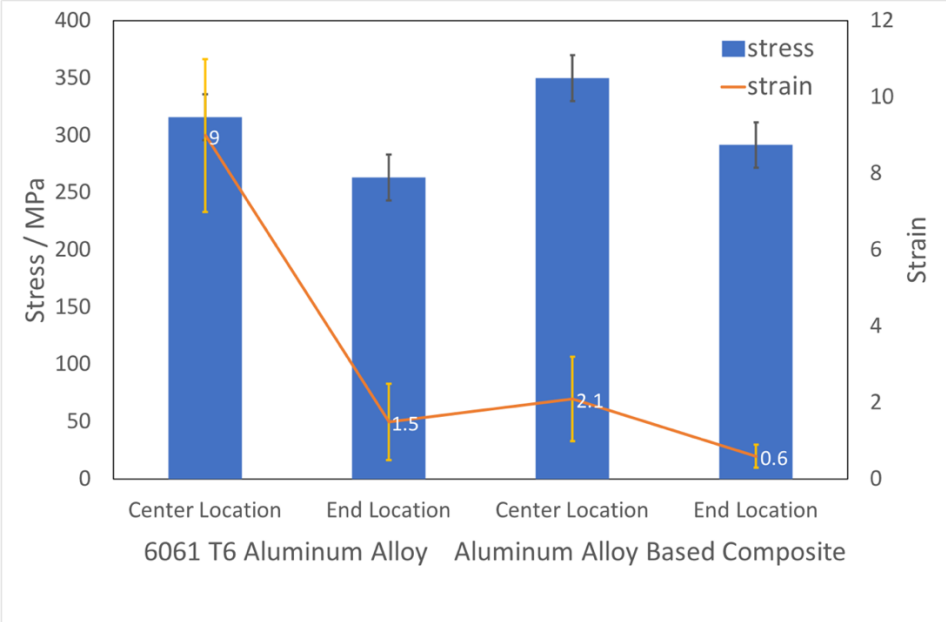



*Figure 98 The applied stress and strain of the center and the end location for two materials' tapered specimen*

### 6.2.2.2 Applied strain

The average strain at the center location of the 6061 T6 aluminum alloy is 9.02±2.05, while that at the end location is 1.47±1.04. However, for the aluminum based composite, the average strain at the center location is 2.89±1.16, and that at the end location is 0.84±0.40 (Figure 98).

Comparing the pre-pitted samples of two materials, the DIC result shows the strain of center location of the 6061 T6 aluminum alloy specimen increases at the beginning of the SCC test and then reaches the plateau (Figure 68). For the 6061 T6 aluminum based composite, after the strain reaches the plateau, it increases again (Figure 92). After 16 days' stress corrosion, the total strain increase along the loading direction of the 6061 T6 aluminum alloy specimen is $(190.0\pm7.2)\times10^{-5}$, while that of the 6061 T6 aluminum based composite specimen is $(39.8\pm43.3)\times10^{-5}$.

The applied strain of the aluminum alloy at the center location is 3.12 times of that of the aluminum based composite, resulting in a 4.77 times larger strain increment during the SCC test. It can be concluded that the applied strain has a direct relation with the strain increase during the stress corrosion, which means it promotes the crack initiation and propagation.

### 6.2.2.3 The addition of SiC nano particles

Although the applied strain of the center location of the aluminum based composite is slightly higher than that of the end location of the aluminum alloy, they are equal within the error range (2.89±1.16 and 1.47±1.04 respectively) (Figure 92). However, a strain increase can be observed on the aluminum based composite specimen, while the strain increment of the aluminum alloy specimen fluctuates around 0. This

phenomenon may be because of the addition of SiC nano particles. The interfacial film and large dislocation density between the reinforcement and matrix lead to a stress concentration at this area. The large stress concentration can either promote the dissolution of atoms, or detach the reinforcement from the matrix[110]. However, there was no cracking observed, so further investigation would be needed to verify this.

# 7 Conclusion and future work

This experiment develops a methodology for SCC test, including the calibration, data collection and analysis methods. The results show that DIC is a reliable technique to precisely measure the displacement and strain change of the specimens during the SCC process. These changes are caused by cracking, as demonstrated by SEM and X-ray tomography.

It proves that the stress corrosion cracks will develop on the 6061 T6 aluminum alloy when a sufficiently high plastic strain is applied. The strain increases rapidly due to cracking, and then saturates. The SCC test was conducted on both pre-pitted sample and non pre-pitted sample, and the result shows that the existence of pre-pitting can accelerate the crack initiation, but does not affect the final strain. This indicates that pre-pitting does not affect the final amount of cracking.

Comparing the SCC result of the end salt deposit location of 6061 T6 aluminum alloy and that of the center salt deposit location of aluminum based composite, these two locations had an almost equal strain applied, and were put in the same environmental condition for the SCC test. After 16 days' stress corrosion, although no cracks could be observed at both locations, the displacement increment of the aluminum based composite specimen is larger than that of the 6061 T6 aluminum alloy specimen. It can be concluded that the addition of SiC nano particles makes the material more susceptible to corrosion.

The center salt deposit location of the 6061 T6 aluminum based composite was at a larger stress but a smaller strain than that of the 6061 T6 aluminum alloy, and cracks were only observed in the 6061 T6 aluminum alloy specimens, indicating that the applied strain instead of the stress is the key factor in the SCC process.

There are some further experiments can be done to verify these conclusions, as well as to deepen the understanding of the SCC process of the 6061 T6 aluminum alloy and that aluminum based composite.

- This project conducted the SCC test on three pre-pitted specimens and one non pre-pitted specimen of 6061 T6 aluminum alloy, and on one pre-pitted specimen and one non pre-pitted specimen of 6061 T6 aluminum based composite. It is worthwhile to conduct repeat experiments on more specimens to verify the conclusion.
- One conclusion of this project is that there is a threshold strain for the stress corrosion crack development on the 6061 T6 aluminum alloy. A series of different strains needs to be tested to find the threshold strain.
- In this experiment, the 6061 T6 aluminum based composite had a strain of 2.1±1.1% applied, and no cracks were observed on the sample surface. A larger strain can be applied to the specimen (within the load capacity of the proving ring) to investigate if cracks will be developed under this condition. A careful comparison should be made with 6061 T6 aluminum alloy specimens loaded to the same strain to verify the effect of the addition of SiC nano particles on the SCC behavior.
- According to the DIC result, the strain over the salt deposit location of the pre-pitted sample increases to $(20\pm1)\times10^{-4}$ and then remains stable, while that of the non pre-pitted sample gradually increases to $(13\pm8)\times10^{-4}$ after 16 days' stress corrosion and then increases to $(19\pm9)\times10^{-4}$ after another 16 days' stress corrosion. It is worthwhile to conduct the SCC test on the 6061 T6 aluminum alloy specimen for a longer time to check if there is a strain increment limit

around $20x10^{-4}$ under this condition.

- A phenomenon observed in this experiment is that the crack propagation stops after several days' stress corrosion. One assumed explanation for it is that when applied a load, the dislocations pile up at the grain boundaries, causing a large shear stress and strain around these areas that induce the crack development. With the propagation of cracks, the shear stress and strain energy decrease, and the propagation rate correspondingly decreases to zero. In order to verify this explanation, techniques such as EBSD can be adopted to check the strains on the grain boundaries of specimens under loading before and after the stress corrosion[111].

# Reference


1. Edwards, K. ASM handbook volume 11: failure analysis and prevention. *Materials & Design* **25,** 735–736 (2004).
2. Rao, U., Vasu, V., Govindaraju, M. & Srinadh, S. Stress corrosion cracking behaviour of 7xxx aluminum alloys: A literature review. *Trans. Nonferrous Met. Soc. China* **26,** 1447–1471 (2016).
3. Cottis, R. *Guides to good practice in conrrosion control*. (1982).
4. Wachob, F. & Nelson, G. Influence of microstructure on the fatigue crack growth of A516 in hydrogen. in *The metallurgical sociaty of AIME* (1980).
5. Guo, T., Qiao, L., Pang, X. & Volinsky, A. Brittle film-induced cracking of ductile substrates. *Acta Mater.* **99,** 273–280 (2015).
6. Burleigh, D. The postulated mechanisms for stress corrosion cracking of aluminum alloys: A review of the literature 1980-1989. *Corros. Sci.* **47,** 89–98 (1991).
7. Skoulikidis, T. & Spathis, K. Influence of stress and notch orientation on SCC in an aluminum alloy. *Corrosion* **45,** 303–307 (1989).
8. Chu, W., Hsiao, C. & Wang, J. Stress corrosion cracking of an aluminum alloy under compressive stress. *Metall. Trans. A* **16A,** 1663–1670 (1985).
9. Davis, R. Corrosion of aluminum and aluminum alloys. *ASM Int.* 351–416 (1999).
10. Polmear, I., John, D., Nie, J. & Qian, M. *Light Alloys*. (Butterworth-Heinemann, 2017).

11. Degarmo, P., Black, T., Kohser, A. & Klamecki, E. *Materials and processes in manufacturing*. (Wiley Publishing, Inc., 2004).

12. Davis, R. *Aluminum and aluminum alloys*. (ASM International, 1993).

13. Bond, M., Robertson, M. & Birnbaum, K. Effects of hydrogen on deformation and fracture processes in high-purity aluminum. *Acta Metall.* **36,** 2193–2197 (1988).

14. Vogt, H. & Speidel, O. Stress corrosion cracking of two aluminium alloys: A comparison between experimental observations and data based on modelling. *Corros. Sci.* **40,** 251–270 (1998).

15. Gruhl, W. Stress corrosion cracking of high strength aluminium alloys. *Z. Met.* **75,** 819–828 (1984).

16. Davoodi, A. Mechanistic studies of localized corrosion of Al alloys by high-resolution in-situ and ex-situ probing techniques. (Royal Institute of Technology, 2008).

17. Pickens, R., Gordon, R. & Green, S. The effect of loading mode on the stress-corrosion cracking of aluminum alloy 5083. *Metall. Trans.* **14,** 925–930 (1983).

18. Skoulikidis, T. & Colios, J. An electrochemomechanical approach to stress corrosion cracking problem of aluminium alloys. *Aluminium* **63,** 619–623 (1987).

19. Connolly, J. *et al.* X-ray microtomography studies of localised corrosion and transitions to stress corrosion cracking. *Mater. Sci. Technol.* **22,** 1076–1085 (2006).

20. Rambabu, P., Prasad, E. & Kutumbarao, V. *Aluminium alloys for aerospace applications*. (Springer Science+Business Media, 2017).

21. Braun, R. On the stress corrosion cracking behaviour of aluminum alloy sheet in an aqueous solution of 3% NaCl + 0.3% H2O2. *Mater. Corros.* **45,** 255–263 (1994).

22. Bucci, J. Selecting aluminum alloys to resist failure by fracture mechanisms. *Adv. Mater. Process.* **155,** 41–44 (1999).

23. Braun, R. Slow strain rate testing of aluminium alloys 7050 in different tempers using various synthetic environments. *Corrosion* **53,** 130–138 (1997).

24. Graedel, E. Corrosion mechanisms for aluminium exposed to the atmosphere. *J. Electrochem. Soc.* **136,** 204–212 (1989).

25. Pyun, I., Moon, M., Ahn, H. & Kim, S. Effects of Cl-, NO3- and SO42- ions on anodic dissolution of pure aluminum in alkaline solution. *Corros. Sci.* **41,** 653–667 (1999).

26. Oger, L., Andrieu, E., Odemer, G. & Blanc, C. About the role of hydrogen in stress corrosion cracking of a 7xxx aluminium alloy (Al-Zn-Mg). *Mater. Sci. Forum* **877,** 522–529 (2016).

27. Joshi, A., Shastry, R. & Levy, M. Effect of heat treatment on solute concentration at grain boundaries in 7075 aluminum alloy. *Metall. Trans. A* **12,** 1081–1088 (1981).

28. Galvele, J. A stress corrosion cracking mechanism based on surface mobility. *Corros. Sci.* **27,** 1–33 (1987).

29. Tsai, C. & Chuang, H. Atmospheric stress corrosion cracking of a superplastic

7475 aluminum alloy. *Metall. Mater. Trans. A* **27,** 2617–2627 (1996).

30. Zhao, P. & Su, Y. Research progress in stress corrosion cracking of high-strength aluminium alloy. *Equip. Environ. Eng.* **13,** 130–138 (2016).

31. Sun, Z. Effect of tempered conditions on the stress corrosion cracking of Al-Zn-Mg-Cu alloy. *J. Chinese Soc. Corros. Prot.* **26,** 232–236 (2006).

32. Siegel, J., Schindelholz, M. & Friedersdorf, F. Small scale crack growth sensor for determination of AA5XXX susceptibility to SCC. in *NACE International Corrosion Conference* (2015).

33. Alyousif, M. & Nishimura, R. The effect of applied stress on environment-induced cracking of aluminum alloy 5052-H3 in 0.5 M NaCl solution. *Int. J. Corros.* **2012,** (2012).

34. Namahoot, J. Effect of deformation on corrosion of Al-Mn alloys. (The University of Birmingham, 2004).

35. Ambat, R., Davenport, J., Afseth, A. & Scamans, G. Electrochemical behavior of the active surface layer on rolled aluminum alloy sheet. *J. Electrochem. Soc.* **151,** 53–58 (2004).

36. Scamans, M., Afseth, A., Thompson, E. & Zhou, X. Thermomechanical processing induced corrosion of aluminium alloy sheet. in *International Symposium on Aluminium Surface Science and Technology* 9–16 (2000).

37. Kim, H., Erb, U., Aust, T. & Palumbo, G. Effect of texture on the corrosion behaviour of high purity aluminum. *Mater. Sci. Forum* **408–412,** 1043–1048 (2002).

38. Elswick, S. Characterization of corrosion pit initiation in aluminum using

advanced electron microscopy techniques. (North Carolina State University, 2006).

39. Pitting Corrosion. *NACE international*

40. Zhang, X., Li, S., Liang, R. & Akid, R. Effect of corrosion pits on fatigue life and crack initiation. in *13th International Conference on Fracture* (2013).

41. Kolios, A., Srikanth, S. & Salonitis, K. Numerical simulation of material strength deterioration due to pitting corrosion. in *2nd CIRP Conference on Surface Integrity* (2014).

42. Fang, B., Eadie, R., Elboujdaini, M. & Chen, W. Transition from pits to cracks in pipeline steel in near-neutral pH solution. in *12th International Conference on Fracture* (2009).

43. Kondo, Y. Prediction of fatigue crack initiation life based on pit growth. *Corrosion* **45,** 7–11 (1989).

44. Jones, H. & Ricker, E. Mechanisms of stress-corrosion cracking. *ASM Int.* (1992).

45. Li, C. & Ellyin, F. Short crack growth behavior in a particulate-reinforced aluminum alloy composite. *Metall. Mater. Trans. A* **26,** 3177–3182 (1995).

46. Omar, G., Esa, R., Tamaldin, N., Masripan, B. & Jasmee, S. The formation of thermally aged stress corrosion cracking on copper oxide surface under high temperature. in *Mechanical Engineering Research Day* (2017).

47. Turnbull, A. Corrosion pitting and environmentally assisted small crack growth. *Proc. R. Soc.* **470,** 1–19 (2014).

48. AZoM. Heat treatment of aluminium and aluminium alloys. *Mater. World* **12,**

37–38 (2004).

49. Rajaa, M., Abdulhadi, A., Jabur, S. & Mohammed, R. Aging time effects on the mechanical properties of Al 6061-T6 alloy. *Eng. Technol. Appl. Sci. Res.* **8,** 3113–3115 (2018).

50. ASTM. *Standard specification for aluminum and aluminum-alloy sheet and plate*. (2014).

51. Lavernia, J. & Schoenung, M. Particulate reinforced aluminum alloy matrix composites-A review on the effect of microconstituents. *Rev.Adv.Mater.Sci.* **48,** 91–104 (2017).

52. Ghazi, H. Production and properties of silicon carbide particles reinforced aluminium alloy composites. *Int. J. Mining, Metall. Mech. Eng.* **1,** 191–194 (2013).

53. Aigbodion, S. & Hassan, B. Effect of thermal ageing characteristics of Al-Si-Fe/SiC particulate composite synthesized by double stir casting. *J. Eng. Res.* **7,** 53–61 (2010).

54. Meena, L., Manna, A. & Banwait, S. An analysis of mechanical properties of the developed Al / SiC-MMC's. *Am. J. Mech. Eng.* **1,** 14–19 (2013).

55. Subramanian, J., Seetharaman, S. & Gupta, M. Processing and properties of aluminum and magnesium based composites containing amorphous reinforcement: A review. *Metals (Basel).* **5,** 743–762 (2015).

56. Aigbodion, S. Development of Al-Si-Fe / SiC particulate composites as advanced materials for engineering application. (Ahmadu Bello University, 2007).

57. Poirier, D., Drew, L., Trudeau, L. & Gauvin, R. Fabrication and properties of mechanically milled alumina/aluminum nanocomposites. *Mater. Sci. Eng. A* **527,** 7605–7614 (2010).

58. Knowles, J., Jiang, X., Galano, M. & Audebert, F. Microstructure and mechanical properties of 6061 Al alloy based composites with SiC nanoparticles. *J. Alloys Compd.* **615,** S401–S405 (2014).

59. Gu, W. Bulk Al/SiC nanocomposite prepared by ball milling and hot pressing method. *Trans. Nonferrous Met. Soc. China* **16,** s398–s401 (2006).

60. Chaubey, K., Gokuldoss, K. & Wang, Z. Effect of particle size on microstructure and mechanical properties of Al-based composite reinforced with 10 Vol.% mechanically alloyed Mg-7.4% Al particles. *Technologies* **4,** 1–8 (2016).

61. Salem, A., Batanony, E. & Ghanem, M. Effect of the matrix and reinforcement sizes on the microstructure , the physical and mechanical properties of Al-SiC composites. *J. Eng. Mater. Technol.* **139,** 1–7 (2017).

62. Tephen, C. & Bernard, C. *ASM handbook volume 13A: corrosion: fundamentals, testing, and protection*. *ASM International* (2003).

63. Abbass, K., Hassan, S. & Alwan, S. Study of corrosion resistance of aluminum alloy 6061/SiC composites in 3.5% NaCl solution. *Int. J. Mater. Mech. Manuf.* **3,** 31–35 (2015).

64. Koch, H. Tests for stress-corrosion cracking. *Adv. Mater. Process.* **159,** 36–38 (2001).

65. Toribio, J. & Ayaso, J. *On the most adequate round notched specimen for*

*hydrogen embrittlement testing*. (2002).

66. British Standard. *Corrosion of metals and alloys-stress corrosion testing*. (BSI Standards Publication, 2018).

67. Goes, O., Castro, P. & Meggiolaro, A. 3D thickness effects around notch and crack tip stress/strain fields. *Frat. ed Integrita Strutt.* **9,** 89–96 (2015).

68. Yu, R., Cao, R., Yan, G. & Chen, H. Effects of short cracks produced at blunted pre-crack tip on stress and strain distributions. *Int. J. Fract.* **132,** 33–48 (2005).

69. Moilanen, P. Pneumatic servo-controlled material testing device capable of operating at high temperature water and irradiation conditions. (Helsinki University of Technology, 2004).

70. Serebrinsky, A. & Galvele, R. Effect of the strain rate on stress corrosion crack velocities in face-centred cubic alloys. *Corros. Sci.* **46,** 591–612 (2004).

71. Drugli, J. & Steinsmo, U. *Assessment of susceptibility to chloride stress corrosion cracking of highly alloyed stainless steels*. (NACE International, 1997).

72. Lyon, N., Marrow, J. & Lyon, B. Journal of materials processing technology influence of milling on the development of stress corrosion cracks in austenitic stainless steel. *J. Mater. Process. Tech.* **218,** 32–37 (2015).

73. Prosek, T., Iversen, A., Taxen, C. & Thierry, D. Low-temperature stress corrosion cracking of stainless steels in the atmosphere in the presence of chloride deposits. *Corrosion* **65,** 105–117 (2009).

74. Isaacs, S. & Looi, M. Behavior of laser welded steel in chloride solution

studied using difference imaging. *Corros. Sci.* **49,** 53–62 (2007).

75. Street, S. Atmospheric corrosion of austenitic stainless steels. (University of Birmingham, 2016).

76. Li, S. & Hihara, L. In situ Raman spectroscopic identification of rust formation in Evans' droplet experiments. *Electrochem. commun.* **18,** 48–50 (2012).

77. Chen, C. & Mansfeld, F. Potential distribution in the evans drop experiment. *Corros. Sci.* **39,** 409–413 (1997).

78. Duff, J. & Marrow, J. In-situ observation of short fatigue crack propagation in oxygenated water at elevated temperature and pressure. *Corros. Sci.* **68,** 34–43 (2013).

79. Reu, L., Rogillio, R. & Wellman, W. Crack tip growth measurement using digital image correlation. in *13th International Conference on Experimental Mechanics* (2007).

80. Cook, A. *et al.* Preliminary evaluation of digital image correlation for in-situ observation of low temperature atmospheric-induced chloride stress corrosion cracking in austenitic stainless steels. *ECS Trans.* **25,** 119–132 (2010).

81. Singh, S. *et al.* In situ experimental techniques to study the mechanical behavior of materials using X-ray synchrotron tomography. *Integr. Mater. Manuf. Innov.* **3,** 9 (2014).

82. Marrow, T., Babout, L., Connolly, B. & Engelberg, D. High-resolution, in-situ, tomographic observations of stress corrosion cracking. *Environ. Crack. Mater.* **2,** 439–447 (2008).

83. Ornek, C., Leonard, F., Mcdonald, A. & Engelberg, L. Time-dependent in situ measurement of atmospheric corrosion rates of duplex stainless steel wires. *Mater. Degrad.* **10,** 1–15 (2018).

84. Horner, A., Connolly, J., Zhou, S., Crocker, L. & Turnbull, A. Novel images of the evolution of stress corrosion cracks from corrosion pits. *Corros. Sci.* **53,** 3466–3485 (2011).

85. Marrow, J., Mostafavi, M., Hashimoto, T. & Thompson, E. A quantitative three-dimensional in situ study of a short fatigue crack in a magnesium alloy. *Int. J. Fatigue* **66,** 183–193 (2014).

86. ASTM. *Standard test method for vickers hardness of metallic materials*. (1997).

87. ASTM. *Standard test methods for tension testing of metallic materials*. (2011).

88. ASTM. *Standard practice for preparation and use of direct tension stress-corrosion test specimens*. (2000).

89. Shoemaker, K. Animating rotation with quaternion curves. in *12th Annual Conference on Computer Graphics and Interactive Techniques* (1985).

90. Salman, K., Aziz, H. & Abdulaziz, M. Effect of surface hardening for aluminium alloys 6061-T6 on mechanical properties. *Am. J. Sci. Ind. Res.* **5,** 134–138 (2014).

91. Wang, B., Chen, X., Pan, F., Mao, J. & Fang, Y. Effects of cold rolling and heat treatment on microstructure and mechanical properties of AA 5052 aluminum alloy. *Trans. Nonferrous Met. Soc. China* **25,** 2481–2489 (2015).

92. Najib, M., Alisibramulisi, A. & Amin, M. The effect of rolling direction to the

tensile properties of AA5083 specimen. in *The International Civil and Infrastructure Engineering Conference 2014* (2014).

93. Reyes-ruiz, C. *et al.* Texture and lattice distortion study of an Al-6061-T6 alloy. *Mater. Trans.* **56,** 1781–1786 (2015).

94. Ahmad, E., Manzoor, T. & Zahid, G. Effect of cold rolling and annealing on the grain refinement of low alloy steel. in *International Symposium on Advanced Materials* (2013).

95. Gao, J. *et al.* Dependence of film texture on substrate and growth conditions for CdTe films deposited by close-spaced sublimation. *J. Vac. Sci. Technol.* **29,** 501–507 (2011).

96. Sakali, J. Investigation of structural and optical properties of GDC thin films deposited by reactive magnetron sputtering. *Acta Phys. Pol. Ser. A* **120,** 63–65 (2011).

97. Braun, R. Investigation on microstructure and corrosion behaviour of 6XXX series aluminium alloys. *Mater. Sci. Forum* **519–521,** 735–740 (2006).

98. Sharma, A. & Kumar, V. Behavior of steels against corrosion in peroxide solutions. *J. Mater. Environ. Sci.* **3,** 76–84 (2011).

99. Mutombo, K. Intermetallic particles-induced pitting corrosion in 6061-T651 aluminium alloy. *Mater. Sci. Forum* **690,** 389–392 (2011).

100. Ding, H., Hawthorn, A. & Hihara, H. Inhibitive effect of seawater on the corrosion of particulate-reinforced aluminum-matrix composites and monolithic aluminum alloy. *J. Electrochem. Soc.* **156,** C352–C359 (2009).

101. Thomson, S. & Frankel, S. Atmospheric pitting corrosion studies of AA7075-

T6 under electrolyte droplets: Part I. Effects of droplet size, concentration, composition, and sample aging. *J. Electrochem. Soc.* **164,** C653–C663 (2017).

102. Jegdic, V., Bobic, M., Alil, B. & Putic, S. Stress corrosion cracking resistance of aluminum alloy 7000 series after two-step aging. *Chem. Ind. Chem. Eng. Q.* **21,** 261–268 (2015).

103. Gao, J. Experiments to explore the mechanisms of stress corrosion cracking. (University of Rochester, 2011).

104. Parrott, R. & Pitts, H. *Chloride stress corrosion cracking in austenitic stainless steel*. (2011).

105. Croize, D., Renard, F. & Gratier, J. *Compaction and porosity reduction in carbonates: A review of bbservations, theory, and experiments*. **54,** (Advances in Geophysics, 2013).

106. Roylance, D. *Introduction to fracture mechanics*. (2001).

107. Guo, Y. *et al.* Measurements of stress fields near a grain boundary: Exploring blocked arrays of dislocations in 3D. *Acta Mater.* **96,** 229–236 (2015).

108. Zhang, J. *Nuclear fuel reprocessing and waste management*. (World Scientific, 2018).

109. Lemus, V., Almaraz, G. & Lopez, J. Stress concentration on artificial pitting holes and fatigue life for aluminum alloy 6061-T6 , undergoing rotating bending fatigue tests. in *Materials Research Society Symposium* (2010).

110. Monticelli, C. Stress corrosion cracking behavior of some aluminum-based metal matrix composites. *Corros. Sci.* **39,** 1949–1963 (1997).

111. Stratulat, A., Duff, A. & Marrow, J. Grain boundary structure and

intergranular stress corrosion crack initiation in high temperature water of a thermally sensitised austenitic stainless steel, observed in situ. *Corros. Sci.* **85,** 428–435 (2014).